



This is to certify that the

dissertation entitled

Investigation of a Carbon Rod Atomization System for Laser-Induced Breakdown Spectroscopy presented by

James R. Ridge

has been accepted towards fulfillment of the requirements for

Ph.D. degree in Analytical Chemistry

Date July 15, 1997

LIBRARY Michigan State University

PLACE IN RETURN BOX to remove this checkout from your record.

TO AVOID FINES return on or before date due.

DATE DUE	DATE DUE	DATE DUE
FEB 0 9 2000		

MSU is An Affirmative Action/Equal Opportunity Institution

INVE

INVESTIGATION OF A CARBON ROD ATOMIZATION SYSTEM FOR LASER INDUCED BREAKDOWN SPECTROSCOPY

By

James Robert Ridge

A DISSERTATION

Submitted to
Michigan State University
in partial fulfillment of the requirements
for the degree of

DOCTOR OF PHILOSOPHY

Department of Chemistry

ABSTRACT

INVESTIGATION OF A CARBON ROD ATOMIZATION SYSTEM FOR LASER INDUCED BREAKDOWN SPECTROSCOPY

By

James Robert Ridge

Laser-induced breakdown spectroscopy (LIBS) is a unique approach to excitation of a sample by a laser plasma. A laser plasma is created by focusing light of a high powered pulsed laser. At the focal point of a planoconvex lens, a luminous plasma is created by dielectric breakdown of the surrounding atmosphere with a temperature and electron density as high as 10⁵ K and 10¹⁹ cm⁻³, respectively. This makes it especially useful for hard-to-excite elements, such as the halogens. Detection of analyte emission from the laser plasma is spectrally and temporally resolved in order to discriminate against the background plasma emission. LIBS has been used primarily for determining solid samples where the laser ablates, atomizes, and excites the analyte. It has also been applied to liquid and gaseous samples.

In this work, a new approach to sample introduction was used. Electrothermal atomization (ETA) is well-known for its superior control and high efficiency for the desolvation, charring, and atomization of a sample. It also has the ability for directly determining analytes that are

solids, l (CRA) f the ana

laser pl

the fun experim

the dete

CRALIBS

solids, liquids, or gases. This work explores using a carbon rod atomizer (CRA) for sample introduction into a laser plasma. Using this method the analyte is separated from the sample matrix, and vaporized into the laser plasma.

This dissertation presents the principles, the instrumentation, and the fundamental characteristics of the laser plasma. The influence of experimental conditions on the characteristics of the laser plasma is also explored. Next, this dissertation presents the application of CRALIBS to the determination metals and nonmetals. Finally, the future potential of CRALIBS is discussed.

TO MY FAMILY

ACKNOWLEDGEMENTS

I would like to first thank my parents for their continuous support (especially financially) through my academic career. They helped me in many intangible ways. Without my parents and family, there would be no dissertation. I thank you from the bottom of my heart.

This project occurred only because Stanley R. Crouch accepted me into his group. His guidance and hands-off approach has been invaluable to me. You provided instantaneous help in the middle of a crisis, and was always available to discuss the latest results, and what direction to head.

Without Stephen Medlin's friendship, writing this acknowledgement page also would have been a dream. It is ironic that I am writing this on the day he leaves to continue his life in another state. He taught me about philosophy, world politics, religion, relationships, and current events. His unique view of the world influenced my life in so many ways. But most importantly, he taught me the skills to be a better scientist. His off the wall suggestions, turned out to have great scientific insight. I will forever miss going out the lunch with you, and especially the late-night breakfasts at Theio's there at the end when things looked gloomy. It will take a lifetime to find a friendship this valuable to me.

Kurt, I have not forgot about you. Just because you are the fourth paragraph doesn't mean you are fourth best. As in the NBA draft, the player who is drafted first is the most important, and the players drafted second through tenth are equivalent in importance. Your influence on my life is as unparalleled as Stephen's, but more in different ways. You not only supported me in offering up suggestions in solving my latest research problem, but your constant striving for knowledge and to understand about how things work in life, keeps me always searching for more than just a cursory answer.

What would happen to me if I forgot Tracy. You probably would not cook those fine meals or wash my laundry anymore. It is quite incredible all the things that you have done for me and probably shouldn't be mentioned here. To an outsider, it may have looked like we are having a serious fling. NOT! Don't worry Nurt, I am sure that I could not afford her, EVER!

Eric. You are quite unbelievable. We spent a great many hours together making an ACS video that will one day make us famous (hope you don't expect to get rich off this), developing courses, and playing basketball. And that is just a few of the things we did together. Most importantly, you gave me alot of &*#@\$! without retribution. The only payment was the spoked rims for Christmas. I cannot forget a friendship like this.

I cannot forget all the people who have had a lasting impression on me: Krissy Sue (Are you ever going to write those acknowledgements?), Eddy (Want another gorilla fart?) and Maria (Take me home and %\$#@& me!), Mary (My lost study partner), Jason (Janal!) and Sue (Hi Sue! ©), BQ, LEP, Gilbey, Berly, etc. Partying with this group gives a new meaning to the phase, "party 'till you puke!" I remember the

initiation the lon football

been a did not had tog

future.

more v

initiation into the Blue Marlin Drinking Club, the free parties at B'zars, the long island iced teas at Olga's, Monday nights at Mac's, and the football and hockey game parties. What a blast!

Finally, a special friend who I owe many thanks. Sue you have been a large part of my life for the last three years. Even though things did not work out the way we planned, I will not forget the good times we had together. Your moral support also will not be forgotten. I learned many things about my weaknesses, and I promise to work on them in the future. I cannot believe that you convinced me to get two cats. Even more unbelievable, I am very attached to Simon and Garfield.

LIST OF

LIST OI

CHAPT

CHAPT

CHAP

CHAP

.

(

L

TABLE OF CONTENTS

LIST (OF TAI	BLES	xi
LIST (OF FIG	URES	xiii
CHAP	TER 1	. INTRODUCTION	1
СНАР	TER 2	HISTORICAL BACKGROUND OF LASER INDUCED BREAKDOWN SPECTROSCOPY	10
	A.	Introduction	10
	B.	Breakdown Mechanisms	12
	C.	Analytical Applications of Laser-induced BreakdownSpectrometry	16
СНАР	TER 3	INSTRUMENTATION	25
	A.	Introduction	25
	В.	Experimental Setup	26
	C.	Experimental Conditions	34
СНАР	TER 4.	CHARACTERIZATION OF ARGON LASER PLASMA	4 0
	A.	Introduction	4 0
	B.	Determination of Excitation Temperature	41
	C.	Determination of Ionization Temperature	4 3
	D.	Determination of the Electron Density	44

E.	Measured Characteristics of the Laser Plasma	45
	1. Physical Dimension of the Plasma	45
	2. Background Emission Characteristics	
	of the Plasma	46
	3. Time-resolved Excitation Temperatures of the Plasma	49
	4. Time-resolved Electron Density of the Plasma	53
	5. Time-resolved Ionization Temperatures of the Plasma	56
	6. Conclusions	57
CHAPTER 5.	INFLUENCE OF EXPERIMENTAL PARAMETERS ON THE CHANGE IN PLASMA CHARACTERISTICS	60
A.	Introduction	60
В.	Preliminary Experiments	61
	1. Determination of the Change in Electron Density in the Plasma	61
	2. Determination of the Change in Ionization Temperature in the Plasma	63
	3. Determination of the Change in Background Emission from the Plasma	64
	4. Determining the Change in Excitation Condition in the Plasma	66
C.	Results of the Factorially Designed Experiment	67
	1. Initial Conditions of the Experiment	67
	2. ANOVA Results	
	3. Dependence of Argon Gas Temperature on Breakdown Threshold	71
	4. Argon Gas Temperature Dependence on Experimental Parameters	72
D.	Conclusions	7 5
CHAPTER 6.	ANALYTICAL STUDIES USING CRALIBS	78
A.	Introduction	78
R	Detection of Analyte Species in the Laser Plasma	79

D

E.

r

Н

i.

K

CHAPTE

B.

C

D.

CHAPTE

A.

B.

C.

C.	Experimental Importance of the Desolvation Stage	81
D.	Effect of Laser Power and Time Delay on Analytical Signal	84
E.	Optimization of Experimental Conditions	87
F.	Development of the Glass Chimney	92
G.	Analytical Detection of Elements	97
H.	Analyte Emission Dependence on Concentration	101
I.	Detection of the Calcium Chloride Salt	103
J.	Determination of Fe in Coal Fly Ash	105
K.	Determination of P in Coal Fly Ash	107
CHAPTER 7.	HELIUM PLASMAS AND THEIR ANALYTICAL APPLICATIONS	112
Α.	Introduction	112
В.	Characteristics of a Helium Plasma	115
C.	Analytical Studies of Chlorine in a Helium Plasma	119
D.	Determination of Chlorine in Pool and Tap Water	121
CHAPTER 8.	CONCLUSIONS AND FUTURE PROSPECTS	124
A.	Conclusions	124
В.	Instrumentation Upgrades	125
C.	Future Applications	127

TABLE

1-

1-

3-

4-

•

• .

4-

4-(4-7

5-]

5-2

5-3

5-4

6-1

LIST OF TABLES

TABLE		PAGE
1-1	Comparison of different excitation sources	5
1-2	Comparison of Different Atomic Spectroscopic Techniques	7
3-1	Summary of Experimental Parameters	38
4-1	Argon Atomic Line Parameters	50
4-2	Determination of Excitation Temperature from Boltzmann Plot of Argon Atom Emission Lines	50
4-3	Argon Ionic Line Parameters	52
4-4	Determination of the Excitation Temperature from a Group of Argon Ionic Lines	53
4-5	Line Widths used for Calculating Electron Density	54
4-6	FWHM for the 4806 Å argon ion line	56
4-7	Time-resolved Ionization Temperature of the Laser Plasma	57
5-1	Electron Densities ($\pm 20\%$) of Argon Plasma Before and During Atomization Cycle (all FWHM are ± 0.5 Å)	63
5-2	Experimental Conditions for the Factorially Designed Experiment	69
5-3	ANOVA Table for the Factorially Designed Experiment	70
5-4	Effect of Atomization Temperature on Slope	75
6-1	Sources of Imprecision for CRALIBS	94

TABLE		PAGE
6-2	Effect of Atomization Temperature on %RSD	96
6-3	Analytical Sensitivities for Calcium. 3933.95 Å Ca(II) line, 2900°C, and 4.0 MW/pulse laser power	99
6-4	Detection Limits for CRALIBS	100
6-5	Slopes for Curves of Growth for CRALIBS	103
6-6	Determination of Fe in Coal Fly Ash using CRALIBS	106
6-7	Determination of Fe in Coal Fly Ash using ICP-AES	107
6-8	Determination of Phosphorus using CRALIBS	108
7-1	Excitation and Ionization Energies for Halogens	113
7-2	Time-resolved Excitation Temperatures of a Helium Plasma	118
7-3	Time-resolved Electron Densities of a Helium Plasma	118

FIGU

3-1

3-

-

3

.

LIST OF FIGURES

FIGURE		PAGE
3-1	Experimental Setup. MC=monochromator, PMT=photomultiplier tube, and PC=personal computer.	26
3-2	Atomization Chamber	28
3-3	PIN Photodiode Detector Calibration Curve	29
3-4	CRA Voltage Drop Calibration Curve	30
3-5	Carbon Rod Stand	31
3-6	Honeycomb Structure	32
3-7	Glass Chimney attachment for Brass Stand	33
3-8	Circuit Diagram for Trigger Conversion	35
4-1	Background Continuum Emission Decay for the Laser Plasma	47
4-2	Argon Background Spectrum. Time Delay = 10 µs	47
4-3	Expanded Argon Background Spectrum at Various Time Delays	48
5-1	Argon Ion Linewidth Before and During Atomization Cycle	62
5-2	Ionization Temperature Change Before and During the Atomization Cycle	64
5-3	Suppression of Continuum Background Emission	65
5-4	Change in the Argon Ion-to-Atom Ratio	67
5-5	Results of the Factorially Designed Experiment	71

FIGURE		PAGI
5-6	Effect of Breakdown Threshold on Gas Temperature	72
5-7	Effect of Argon Flow Rate on Maximum Gas Temperature	74
5-8	Effect of Height above the Carbon Rod on the Maximum Gas Temperature	74
6-1	Chromium Ionic Emission in the Laser Plasma. 2677.2 Å Cr(II), 25 µs time delay, 3.6 MW/pulse laser power, and 2700°C atomization temperature	80
6-2	Effect of Omitting Desolvation Cycle. 5890 Å Na(I), 25 µs time delay, 3.0 MW/pulse laser power, and 2200°C atomization temperature	83
6-3	Effect of Using Desolvation Cycle. 5890 Å Na(I), 25 µs time delay, 20 sec desolvation cycle at 100° C, 3.0 MW/pulse laser power, and 2200°C atomization temperature	84
6-4	Effect of Laser Power on Sodium Atomic Emission. 5890 Å Na(I), and 2500°C atomization temperature	85
6-5	Effect of Laser Power on Magnesium Ionic Emission. 2795.5 Å Mg(II) ion line, and 2600°C atomization temperature	86
6-6	Effect of Laser Power on Background Continuum. 8375 Å Cl(I) line, and 25 µs time delay	88
6-7	Time-resolved Relationship of Background Intensity. Zn(II) 2062 Å line, and 3 MW/pulse laser power	89
6-8	Effect of Time Delay on SBR for Ca(II). Ca(II) 3933 Å line, 4 MW/pulse laser power, and 3000°C atomization temperature	90

FIGU

6-4

6-

6-

6-

6

7

7

FIGURE		PAGE
6-9	Signal-to-Noise Ratio for the Background Continuum at Various Time Delays. Fe(II) 2599.4 Å line, and 3.0 MW/pulse laser power	90
6-10	Effect of Time Delay on %RSD of Zn(II) Signal. 100 ppm Zn, Zn(II) 2062 Å line, and 3000°C atomization temperature	91
6-11	Effect of Glass Chimney on Sensitivity. 3933 Å Ca(II) line, 50 µs time delay, 2600°C atomization temperature, and 3.5 MW/pulse laser power	97
6-12	Working Curve for Chromium. 2677.2 Å Cr(II) line, 25 µs time delay, 2950 °C atomization temperature, and 3.6 MW/pulse laser power	98
6-13	Effect of Chloride on Ca(II) Emission. 3933 Å Ca(II) line, 50 µs time delay, 2600°C atomization temperature, and 3.5 MW/pulse laser power	104
7-1	Helium Plasma after 25 µs Time Delay with a laser power of 8.0 MW/pulse	116
7-2	Signal-to-Background Ratio for Cl(I) in a He Plasma	119
7-3	Profile of Cl(I) Emission in a He Plasma	120
7-4	Working Curve for Chlorine. Cl(I) 8375 Å line, 25 us time delay, and 2600°C atomization temperature	121

CHAPTER 1

INTRODUCTION

"The average Ph.D. thesis is nothing more but a transference of bones from one graveyard to another."

J. Frank Dobie, "A Texan in England," 1945

The ideal elemental technique (1) has the ability to determine all elements simultaneously in any sample form (solid, liquid, gas). This ideal analytical technique also has the ability to determine the analyte at any concentration within any sample matrix. It would also possess no chemical, matrix, or spectral interferences.

Actually, the analytical technique chosen for a given determination depends on sample form and matrix, analyte concentration, and quantity of sample available. The chosen technique will have the most flexible sample introduction. For current atomic spectroscopic methods, the ideal technique should have separate control over the individual processes of desolvation, ashing, atomization, and excitation of the analyte. This will ultimately allow optimization of each process which leads to increased sensitivity, precision, accuracy, lower detection limits, and minimization or elimination of interferences. In order for simultaneous multielement detection, the technique must be emission based.

One of the techniques that provides some of the ideal characteristics is electrothermal atomization (ETA). ETA possesses superior control over the volatilization, ashing, and atomization of most elements present in complex matrices. The sample requirements are

typically 1 to 20 µL. Detection limits for volatile elements such as alkali, alkaline earth, and many transition elements are at ultratrace levels (subpicogram) (1). For less volatile elements such as Al, Si, B, and rare earth metals, the detection limits are 1 to 100 picograms. Linearity of the working curve extends over 5 orders of magnitude of concentration (2).

However, electrothermal atomization is plagued with many interferences; most of these are chemical in origin (3,4). A chemical interference is any chemical process that reduces the population of free atoms in the gas phase. Many transition elements form stable oxides above the atomizer surface (pyrolytic graphite) (5,6), while others react with the atomizer to form stable carbides (3,5). Other interferences include suppression of the analyte signal due to interelement matrix interferences and formation of stable refractory molecules (7–9). These interferences can be reduced in magnitude, but not eliminated, by using a set of conditions developed by Slavin (6) called the Stabilized Temperature Platform Furnace (STPF) conditions. This procedure usually calls for some type of time-intensive separation of the analyte into a suitably non-interfering matrix, or a matrix modification to reduce the effect of the interference before an analysis is performed. A matrix modification is "the process of chemical alteration of the desired analyte." sample matrix, or graphite surface (10)." A typical modifier is the addition of palladium to the sample matrix. The STPF conditions also dictate the use of a L'vov platform (10) to produce a time lag in atomization of the analyte until the gas temperature within the furnace has increased. This reduces the condensation of the atoms in the gas phase.

The high atomization efficiency of ETA has led many researchers to use different methods of independent excitation of the atomic plume. These include glow discharges (GD) (11), capacitively coupled plasmas (CCP) (12), and inductively coupled plasmas (ICP) (13). These excitation sources have a high excitation efficiency for a wide range of elements. The GD and CCP excitation sources are actually formed within the graphite furnace during the atomization cycle. This provides further atomization, dissociation of molecules as well as excitation and ionization of the vaporized analyte. These two methods maximize transport efficiency of the analyte plume into the excitation source since the discharge is formed inside the furnace. With the ICP, however, the analyte vapor generated in the graphite furnace must be transported to the plasma. Detection limits for the above techniques are comparable or superior to graphite furnace atomic absorption spectrometry.

Table 1-1 (11) compares the physical parameters of four excitation sources. The choice of the excitation source is most critical. The choice depends on the fraction of atomized sample that is actually transported to the excitation source, the residence time in the region of the source that is observed, the degree of excitation of the sample, and the magnitude of specific interferences within the excitation source. By switching to a high energy laser plasma the excitation efficiency increases by 10⁴ or more, since the fraction of atoms excited is directly related to the temperature of the excitation source according to the Boltzmann equation (assuming thermodynamic equilibrium). The increased excitation fraction results in an increase in analyte emission, not only from excited atoms but also from excited ions due to the

increas
that podeterm
infrare
ionic li
emissionexcitati

laser p
the sur
can be
is not
concen
laser p
may for
is usua
atoms f

access i

formed

electro

maximi

F, S, Si,

increased ionization efficiency of the laser plasma. This allows analytes that possess atomic emission lines in the vacuum ultraviolet to be determined using their ionic emission lines in the visible or near infrared (14). The increased excitation of the laser plasma also allows ionic lines having better sensitivity to be used, or it allows an alternate emission line to be employed for reduced spectral interferences. Finally, excitation of elements possessing high ionization potentials such as Cl, F, S, Si, and B is possible.

Laser-induced plasmas (LIP) are created by focusing a high energy laser pulse to the diffraction limit and causing dielectric breakdown of the surrounding atmosphere. Laser plasmas have many properties that can be exploited. Being optically thin (15), the emission from the plasma is not self-absorbed. This allows a large dynamic range (10^4-10^5) of concentrations to be used. The higher excitation temperature of the laser plasma has sufficient energy to dissociate molecular species that may form after the atoms leave the surface of the atomizer. The plasma is usually formed in an inert atmosphere (N₂, Ar, He) which protects the atoms from reacting with species such as molecular oxygen. Only optical access is required to form the laser plasma. This allows the plasma to be formed directly within the atomic plume generated by the electrothermal atomizer. Thus, transport efficiency is automatically maximized.

Table 1-1. Comparison of different excitation sources (11)

Excitation Source	Gas Temp(kK)	Electron Temp (kK)	β _e fraction excited	β _i fraction ionized	Background intensity
ICP	5-10	5-10	10-5 - 10-4	high	moderate
GD	1-3	10-20	10-5 - 10-4	high	low
GF	2-3	2-3	10-8 - 10-4	low	low
LIP	10-20	10-20	> 0.3	high	low

ICP = Inductively Coupled Plasma

GD = Glow Discharge

GF = Graphite Furnace

LIP = Laser-induced Plasma

Table 1-2 (1,11–13,16) compares the figures of merit for some of the best analytical spectrometric techniques routinely available. For comparison, data from this dissertation have been included. These techniques have been developed into very powerful trace and ultratrace analysis methods due to low sample consumption and the capability of multielement determinations with large dynamic ranges. Other reasons for the acceptance of these techniques have been the successful removal, or suppression, of matrix, chemical, and spectral interferences. The development of the hyphenated techniques in Table 1-2 are based on electrothermal atomization for sample introduction into either a glow discharge, capacitively coupled plasma, or inductively coupled plasma. These hyphenated techniques have shown to improve detection limits

and reduce interferences for many elements using a limited amount of sample. They also have been used for non-metal determinations with great success.

This dissertation introduces a new analytical technique that uses a carbon rod atomization system as the sample introduction system for laser-induced breakdown spectroscopy (CRALIBS). In the following chapters, the principles, instrumentation, and application of this method for the determination of metals and non-metals are presented. Chapter 4 describes the physical parameters of the plasma, such as the excitation and ionization temperatures, and the electron density. Chapter 5 discusses the influence of the experimental parameters on the plasma characteristics. Following the fundamental studies of the laser plasma, results showing the analytical utility of this technique for determining metals and non-metals in complex matrices are presented. Finally, the analytical potential of this new technique for the future is discussed.

 Table 1-2
 Comparison of Different Atomic Spectroscopic Techniques

;	GFAAS*	ICP- AES*	FAPES†	FANES‡	ICP- MS [§]	ETA/ICP- MS"	ETA - LIBS ^{††}
detection limit (pg)	0.04 - 100	1 - 1000	<1.0	<1.0	<1.0	1 - 100	100 - 1000
sample required (µL)	1 - 20	100 to 2000	1 - 20	1 - 20	100 to 2000	1 - 20	1 - 20
elements per sample	1-2	>40	>40	>40	>40	>40	>40
dynamic range	$10^2 - 10^5$	10 ⁵ -	104	10 ⁵	10 ⁵ -	105	10 ⁵ -

GFAAS = Graphite Furnace Atomic Absorption Spectrometry

ICP-AES = Inductively Coupled Plasma Atomic Emission Spectrometry

FAPES = Furnace Atomization Plasma Excitation Spectrometry

FANES = Furnace Atomization Nonthermal Excitation Spectrometry

ICP-MS = Inductively Couple Plasma-Mass Spectrometry

ETA/ICP-MS = Electrothermal Atomization/Inductively Coupled Plasma-Mass Spectrometry

ETA-LIBS = Electrothermal Atomization/Laser-induced Breakdown Spectrometry

^{*} Reference 1

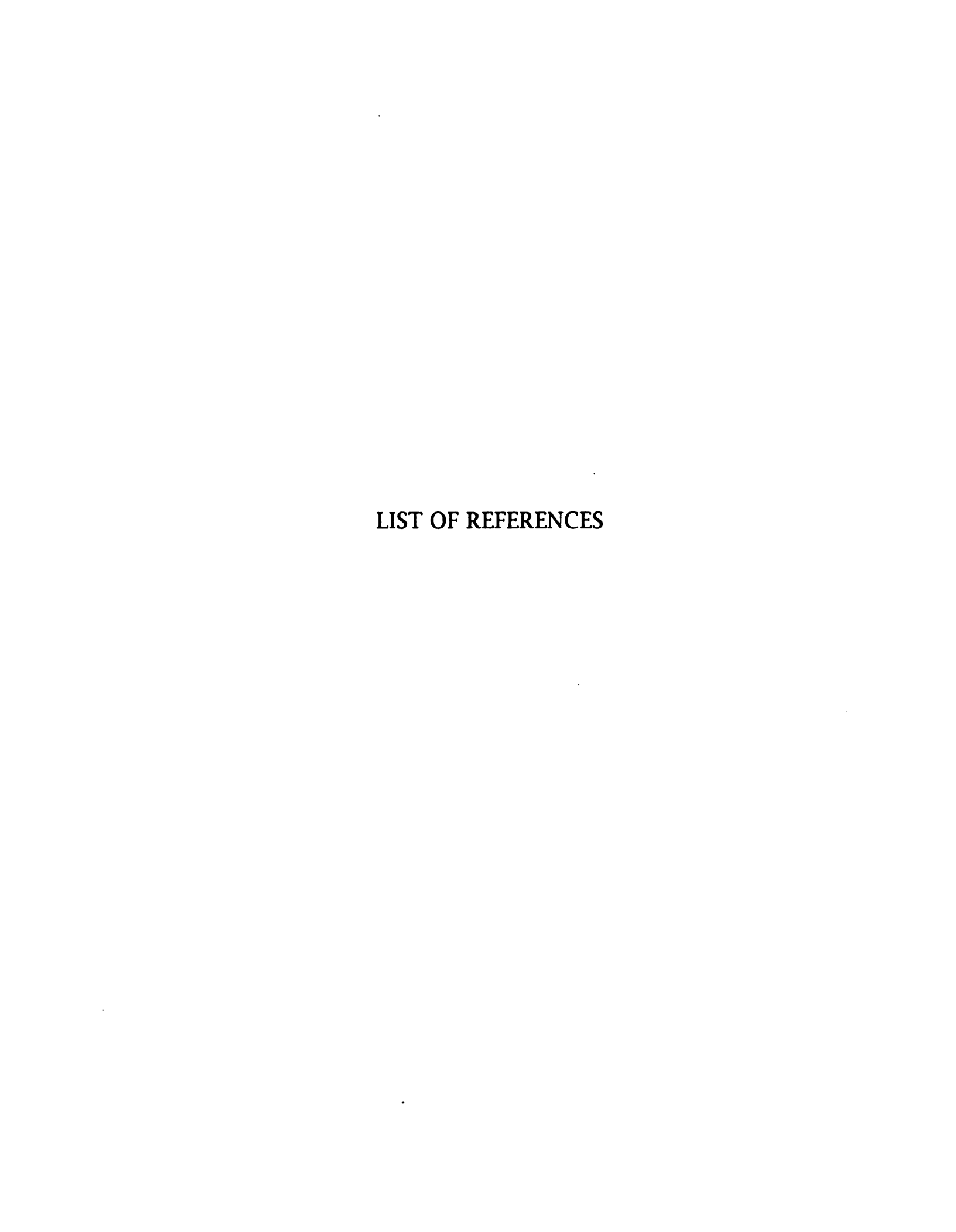
[†] Reference 12

[‡] Reference 11

[§] Reference 16

^{**} Reference 13

^{††} This work



l.

2.

3.

4. 5.

6.

7.

8.

9.

10.

11.

12.

13. 14. 15.

LIST OF REFERENCES

- 1. Ingle, J. and Crouch, S., *Spectrochemical Analysis*, Prentice Hall, Engelwood Cliffs, NJ, 1987
- 2. Fuller, C. W., Electrothermal Atomization for Atomic Absorption Spectrometry, Burlington House, London, 1977
- 3. L'vov, B., J. Anal. Atom. Spectrom., 3, 9 (1988)
- 4. Brown, A., J. Anal. Atom. Spectrom., 3, 67 (1988)
- 5. Wendl, W. and Vogt-Muller, G., Spectrochimica Acta, Part B, 40, 527 (1985)
- 6. Slavin, W. and Manning, D., Spectrochimica Acta, Part B, 37, 955 (1982)
- 7. Lauri, H., J. Anal. At. Spectrom., 7, 735 (1992)
- 8. Chauvin, J., Davis, D., Hargis, L., Anal. Lett, 25, 137 (1992)
- 9. Hulanicki, A., Bulska, E., Dittrich, K., J. Anal. At. Spectrom., 5, 209 (1990)
- 10. Carnick, G, Schlemmer, G., Slavin, W., Am. Lab, February, 120 (1991)
- 11. Falk, H., Hoffmann, E., Ludke, Ch., Spectrochimica Acta, Part B, 39, 283 (1984)
- 12. Smith, D., Liang, D., Steel, D., Blades, M., Spectrochimica Acta, Part B, 45, 493 (1990)
- 13. Matusiewicz, H., Barnes, R., Spectrochimica Acta, Part B, 40, 29 (1985)
- 14. Cremers, D. and Radziemski, L, Anal. Chem., 55, 1252 (1983)
- 15. Tourin, R. H., J. Quant. Spec. Rad. Trans., 3, 89 (1963)

16. Houk, R. and Thompson, J., Mass Spectrometry Reviews, 7, 425 (1988)

CHAPTER 2

HISTORICAL BACKGROUND OF LASER INDUCED BREAKDOWN SPECTROSCOPY

A. Introduction

Atomic emission spectroscopy (AES) has been used since the 1930s as an analytical tool for the identification and quantification of elements in a wide variety of sample forms and concentrations. In the middle of the 1960s the advantages of inductively coupled plasma (ICP) atomic emission spectrometry (AES) were realized. Because the technique is emission based, the modern ICP offers simultaneous multielemental detection of many metals and nonmetals at the trace and ultratrace level (1). In addition, interferences and background emission are lower than with other sources. However, ICP-AES requires the sample to be in an aqueous media and free of particulates. When the analyte is a solid, it must be dissolved or vaporized for before introduction into the plasma. If the analyte is present in an organic matrix, a suitable extraction must be performed.

To overcome the sample introduction limitations, electrothermal atomization was recognized for having superior control over desolvation, charring, and atomization of the sample. Littlejohn and Ottaway (2) explored graphite furnace atomic emission spectrometry for multilelement trace analysis, but quickly realized that the furnace did not provide thermal excitation of elements with high excitation potentials. The theory of electrothermal atomization is summarized by

Fuller (3). L'vov (4) has reviewed the evolution and acceptance of electrothermal atomization.

The next advancement to improve excitation of the atomic plume within the graphite furnace was the development of Furnace Atomization Nonthermal Excitation Spectrometry (FANES) which was first proposed by Falk (5). This technique introduces a liquid sample through the dose hole of a graphite furnace. After the sample has been dryed and ashed, the gas pressure in the graphite furnace is then reduced to several torr. A large voltage is applied between a carbon rod which traverses the center of the graphite furnace and the graphite furnace. A hollow cathode discharge is formed and allowed to stabilize for 10 to 20 seconds. The furnace temperature is then increased in order to atomize the sample. Atomic emission from the vaporized sample results from high energy electron collisions within the discharge. The furnace is flushed with purge gas at atmospheric pressure to prepare the furnace for the next sample.

Because the discharge is not in local thermodynamic equilibrium (6), it has very low background emission. This is the limiting factor that determines the detection limit for FANES (7). Present detection limits are comparable or superior to graphite furnace atomic absorption spectrometry (7). FANES also possesses a large dynamic range, narrow linewidths, and the ability for excite all metals and non-metals.

A similiar technique to FANES is Furnace Atomization Plasma Excitation Spectrometry or FAPES. First developed by Blades (8), an atmospheric capacitively coupled plasma (CCP) is formed during the atomization cycle within a graphite furnace. The sample is introduced in the same way as the FANES technique. However, the excitation of the

sample is done at atmospheric pressure. Background emission from the plasma is minimal as in the FANES technique. Reported detection limits are similar to that of FANES, but with the capability of higher sample throughput.

In addition to glow discharges and the capactively coupled plasmas for excitation of analyte species, laser plasmas have also been used. Since the discovery of laser plasmas in 1963, the formation of laser plasmas has been studied extensively. Only within the last ten years have laser plasmas been used for determination of elements in air, bulk solution, aerosols, and direct ablation of sample targets. It is the goal of this chapter to present a summary of the theory of plasma formation followed by analytical applications of the technique called Laser Induced Breakdown Spectrometry, or LIBS.

B. Breakdown Mechanisms

Dielectric breakdown of air induced by pulsed laser radiation was first reported by Maker *et al.* (9) and by Mayerand and Haught (10). The traditional method to generate a laser plasma in a gas is to focus a 1-10 joule laser pulse to a fluence greater than 10 MW/cm² (11). Breakdown occurs when the electric field (10⁵ V/cm) at the focal point exceeds the dielectric strength of the medium. The resulting plasma has a temperature of 10⁴ to 10⁵ Kelvin, an electron density of 10¹⁵ to 10¹⁹ cm⁻³, a lifetime of tens of microseconds, and a volume of about 250 mm³ (11).

The formation of laser plasmas has been studied in nitrogen, oxygen, and air, as well as in various monoatomic gases. It has been found that the threshold energy required for the formation of the

plasma is affected by the properties of the surrounding gas (12–15) as well as the pressure (12–16), the wavelength of the laser (17–20), the pulse length (21), and the focal spot size (15, 21, 22) of the beam. Each parameter directly influences the dominant breakdown mechanism by which the plasma is formed.

There are two mechanisms by which optical breakdown can occur. These are the collisional or cascade ionization, and the multiphoton ionization (MPI) processes (23). Recent studies by Gamel and Moneim (24,25) show that breakdown actually occurs by a combination of both mechanisms. The collisional ionization process assumes a "seed" electron is created. There are several possible sources for the seed electron. It may come from naturally occurring electrons (10⁻³ to 10 cm⁻³) resulting from cosmic rays, thermionically emitted electrons from aerosols particles, an impurity such as an organic vapor with a lower ionization potential or multiphoton ionization of the gas itself. Within the focus of the laser beam, this free electron gains energy from the optical frequency electromagnetic field upon collision with another atom or ion to produce another electron. When the energy gained by free electrons overcomes the losses from electron diffusion, electron attachment to oxygen, recombination, and emission from excited species within the focal volume, excitation and ionization of atoms will produce more electrons to sustain the plasma. This defines the breakdown threshold energy for plasma formation. Above the breakdown threshold, an avalanche or cascade of electrons results. As the ionization process continues, the plasma produced rapidly becomes opaque, absorbs more laser energy, and grows toward the laser source until the end of the pulse (11,26).

Theoretical calculations of the breakdown threshold of gases, defined as an electron concentration of 10¹³ cm³ or 0.001% ionized, have been carried out by Kroll and Watson (27) and have been experimental studied extensively (10,11,24-29,43,46). It has been found that the breakdown threshold is inversely proportional to the pressure of the gas. It is also dependent on the type of gas (atomic or molecular) used, its ionization potential, the wavelength of laser light used, the diameter of the laser spot size, and the duration of the pulse (26,46). By studying these parameters it is possible to determine the mechanism for plasma formation (27). Early research probed the physics of the plasma in the gas phase with time-resolved studies being used to discriminate against the intense background emission upon generation of the plasma. Breakdown thresholds, electron densities, ion temperatures and the variables that affect them have been measured for various gases such as air (30,31), N_2 (32,33) and O_2 (32), He (33,34), and Ar (35,62). Later studies involved creating a laser spark in water (36-41,65,66) and in aerosols. These experiments indicated that if small liquid or aerosol particles were present in the laser focal volume where the plasma is created, the breakdown threshold could be reduced up to three orders of magnitude due to the magnified field around the particle (11,28,42,62,64,68). The breakdown threshold can also be influenced by the prescence of preionization (43). The source of preionization is from the creation of initial electrons using a dc static field (44, 45) or the laser beam (46–48). The existence of preionization at the focal volume of the laser beam reduces the breakdown threshold by providing the seed electrons needed to create and sustain the plasma.

The second mechanism by which a plasma may form is the MPI process. This mechanism is highly improbable due to the low energy of each laser photon and the number of photons required to ionize the gas. The multiphoton absorption process requires the promotion of a electron to a virtual state at an energy equal to the photon energy absorbed, E=hv, followed by another absorption of a photon and promotion of the electron to a virtual state at 2hv. This occurs until the ionization potential is reached. For example, if the fundamental wavelength of a Nd:YAG pulsed laser (1064 nm, 1.17 eV) were used to breakdown argon (IP = 15.8 eV), the absorption of 14 photons would be required (49). Experimentally, the Lebedev Institute has determined that it requires only 10.3 ± 0.3 photons (50). The number of photons required experimentally is less due to pertubation of the upper levels in the gas from the high electric field, which effectively lowers the ionization potential of the gas (51). Nonetheless, the probability cross section for MPI is approximately 10⁻¹⁴⁶ cm⁻² (51).

When sufficiently high photon energy, i.e., ultra-violet or visible laser radiation, is used for plasma creation, the multiphoton ionization process can dominate over cascade ionization. To determine experimentally the dominant mechanism, the laser pulse duration and gas pressure must be varied. In general, it has been found that when the pulse duration is short compared to time of free electron loss (10⁻⁷ seconds), the multiphoton ionization process becomes dominant (51). At atmospheric pressure, the pulse duration must be on the order of picoseconds for the MPI mechanism to dominate. At millitorr pressures the pulse duration can be as long as tens of nanoseconds and the multiphoton ionization mechamism will be dominant (51).

After the initiation or generation step, a laser plasma proceeds through two subsequent stages, growth and decay (49). During the growth stage the plasma absorbs and reflects the laser radiation; this rapidly increases the temperature and electron density and size of the plasma. The final stage, decay, starts at the end of the laser pulse. In this stage "optical detonation" occurs from heat conduction and shock wave mechanisms, analogous to a combustion wave. Recombination becomes the dominant mechanism until the plasma extinguishes. The time scale of each stage varies. Generally, initiation requires a few nanoseconds, growth occurs throughout the lifetime of the laser pulse, and decay lasts up to several tens of microseconds after the laser pulse (23, 26).

C. Analytical Applications of Laser induced Breakdown Spectrometry

Laser plasmas have been applied as a high intensity sources for X-ray lithography (52–54), for pumping dye lasers (55), and for time-resolved EXAFS (56–58). They have also been used in the application of controlled thermonuclear fusion (59).

In 1981, Cremers and Radziemski initiated analytical applications of LIBS by monitoring beryllium directly in air. The first method involved time-integrating the plasma emission for the determination (60). The second method involved time discrimination of the intense background that is present after the formation of the plasma. Better control over background emission, interferences, and molecular emission, as well as improved detection limits were possible (61).

LIBS has been used for determining the concentration of chlorine and fluorine in a gas sample (62). Since the atomic emission lines of

chlorine and fluorine are in the vacuum ultraviolet range, it was necessary to determine the concentrations using the ion lines in the near infrared region. This was made possible by the higher temperature plasma. Reported temperatures for this determination were in the range of 15000 K, about double a typical ICP. In the same year, Radziemski and co-workers determined beryllium, sodium, phosphorus, arsenic, and mercury in aerosols produced at atmospheric pressure (11).

Another application was the direct detection of beryllium on filters using LIBS. Direct monitoring of airborne beryllium using LIBS did not provide sufficient sensitivity due to the high toxicity of the element. The maximum exposure limit for Be is $2 \mu g/m^3$ for the average concentration during a eight hour period, and $25 \mu g/m^3$ over a period not longer than thirty minutes (63). By concentrating the airborne particulates on filter paper, this technique provided near real-time determinations for the monitoring of airborne particulates (64).

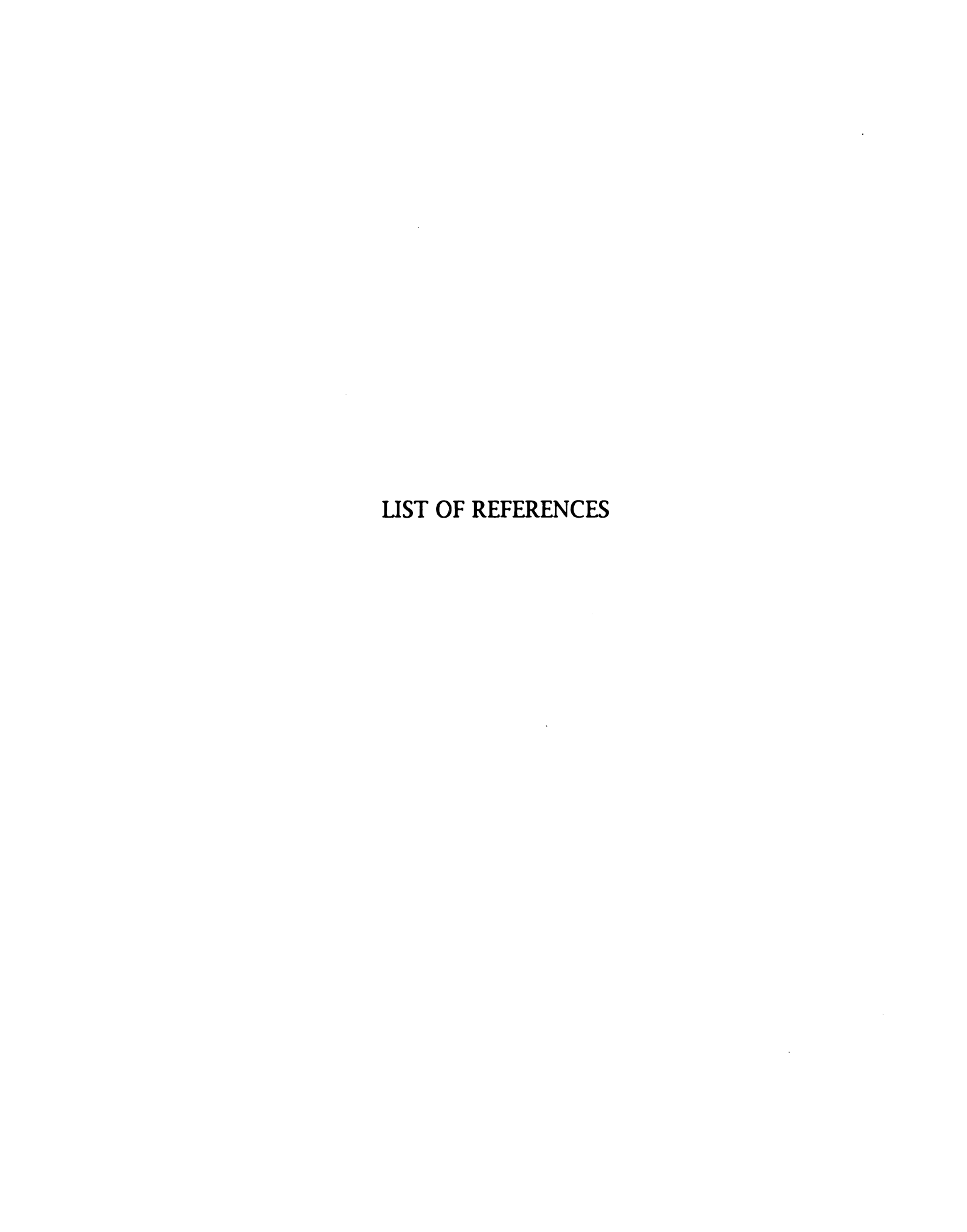
Cremers and co-workers further expanded the LIBS technique to determine alkali and alkaline earth metals in bulk aqueous solution with detection limits on the order of 1 μ L/mL, which are higher than for ICP-AES (65). Detection limits were greatly improved, especially for hard-to-ionize species such as boron, by using repetitive spark pairs, where the second laser pulse would follow less than 200 µsec later; this further increases the temperature of the plasma (65).

Archontaki and Crouch (66) used LIBS in conjunction with an isolated droplet generator (IDG). The IDG technique developed by Wiegand and Crouch (67) and led to interfacing atomic emission spectroscopy with flow injection analysis (FIA). This was possible due to the low dead volume of the isolated droplet interface. Time-resolved

methods and signal processing produced dynamic ranges extending over three orders of magnitude, and detection limits that were in the part-per-million (ppm) range for nanoliter sized droplets. Archontaki also showed that interferences, such as the classical phosphate interference on calcium emission in flame emission spectroscopy, were eliminated because at the higher temperature, the plasma had sufficient energy to break the bonds of the refractory species. The presence of sodium and aluminum actually enhanced the calcium (II) emission signal due to the suppression of higher ionization states of calcium present in the plasma.

LIBS possesses inherent advantages over conventional arc, spark, and plasma atomic emission spectroscopy. There is no wear on electrodes, which could introduce spectral interferences or perturbations in the plasma. The analysis can be performed in a remote location since the formation of the plasma only requires optical access. There is little sample preparation and simultaneous multielement determinations are Ottensen and co-workers demonstrated that LIBS is a possible. noninvasive technique in the determination of the elemental composition of entrained coal, char, and mineral matter in the combustion zone of a coal reactor (68). Cremers (69) showed the portability and the remote capability of the technique by determining the composition of metals by ablating metal from the surface using the laser plasma. The main limitations for this determination were collection of the emission with a fiber optic and plasma formation due to poor beam quality. LIBS has also been used for the determination of beryllium in beryllium-copper alloys (70) and manganese and chromium in steels (29).

Recently, the laser plasma was used as a continuum source for the detection of transient molecular species in a graphite furnace (71). The first reported use of a laser plasma as the excitation source for multielemental detection with graphite furnace atomization was by Majidi (72). Detection limits for cobalt and cadmium were 5 pg and 50 pg, respectively. This is comparable to detection limits with graphite furnace atomic absorption spectrometry, but with the advantage of minimizing or eliminating matrix interferences. More recently, this technique was applied in trace metal analysis for Hg, Pb, and Al (73). No detection limits or working curves were presented, but the results indicate that the laser plasma can be of analytical utility. Recently, a review of the spectroscopic applications of laser-induced plasmas has been published (74, 75). There are also two books that review the various aspects of laser plasmas (26, 76).



LIST OF REFERENCES

- 1. Fassel, V., Science, 202, 183 (1978)
- 2. Littlejohn, D. and Ottaway, J. M., Analyst, 104, 208 (1979)
- 3. Fuller, C. W., Electrothermal Atomization for Atomic Absorption Spectrometry, Burlington House, London, England, 1977
- 4. L'vov, B., 63, Anal. Chem., 924A (1991)
- 5. Falk, H. Hoffmann, E., Jaeckel, I., Lüdke, Ch., Spectrochim Acta, 34B, 333 (1979)
- 6. Falk, H., Spectrochim. Acta, 32B, 437 (1977)
- 7. Falk, H., Hoffmann, E., Lüdke, Ch., Spectrochim. Acta, 39B, 283 (1984)
- 8. Blades, M. W., Liang, D. C., Spectrochim. Acta, 44B, 1059 (1989)
- 9. Maker, P. D., Terhune, R. W., and Savage, C. M., in Proceedings of the 3rd International Conference on Quantum Electronics, Paris (1963) Vol. 2 (Columbia University, New York, 1964), pp. 1559-1576
- 10. Mayerand, R. and Haught, A., Phys. Rev. Lett., 11, 40 (1963)
- 11. Radziemski, L.; Loree, T.; Cremers, D.; Hoffman, N.; Anal. Chem., 55, 1246 (1983)
- 12. Minck, R. W., J. Appl. Phys., 35, 252 (1964)
- 13. Thomlinson, R. G., Damon, E. K., Buscher, H. T., Physics of Quantum Electron. (Proc. Intern. Conf., San Juan, Puerto Rico, 1965), ed. by Kelley, P. L., et al., McGraw-Hill, New York (1966), p. 520
- 14. Bergqvist, T. and Leman, B., Ark. Fys., 31, 177 (1966)

- 15. Mitsuk, V. E. and Chernikov, V. A., ZhETF Pis'ma Red., 4, 129 (1966)
- 16. Gill, D. H. and Dougal, A. A., Phys. Rev. Lett., 15, 845 (1965)
- 17. Generalov, N. A., Zimakov, V. P., Kozlov, G. I., Masyukov, V. A., Razier, Y. P., ZhETF Pis'ma Red., 11, 343 (1970)
- 18. Smith, D. C., J. Appl. Phys., 41, 4501 (1970)
- 19. Buscher, H. T., Tomlinson, R. G., Damon, E. K., Phys. Rev. Lett., 15, 847 (1965)
- 20. Alcock, A. J., Kato, K., Richardson, M. C., Optimum Commun., 6(4), 342 (1969)
- 21. Smith, D. C., Appl. Phys. Lett., 19, 405 (1971)
- 22. Mitsuk, V. E. and Chernikov, V. A., ZhETF Pis'ma Red., 6, 627 (1967)
- 23. Radziemski, L. and Cremers, D., Laser Induced Plasmas and Applications, Marcel Dekker, N.Y., 1989
- 24. Gamel, Y. and Moneim, A., J. Phys. D: Appl. Phys., 20, 757 (1987)
- 25. Gamel, Y., J. Phys. D: Appl. Phys., 22, 385 (1989)
- 26. Razier, Y. P., Laser Induced Discharge Phenomena, Consultants Bureau, N.Y., 1977
- 27. Kroll, N. and Watson, K., Phys. Rev. A, 5, 1883 (1972)
- 28. Pinnick, R., Chylek, P., Jarzembski, M., Creegan, E., Srivastava, V., Fernandex, G., Pendleton, J., Biswas, A., Appl. Opt., 27, 987 (1988)
- 29. Belleveau, J., Cadwell, L., Coleman, K., Huwel, L., and Griffin, H., Appl. Spec., 39, 727 (1985)
- 30. Ramsden, S. and Davies, E., Phys. Rev. Lett., 13, 227 (1964)
- 31. Tulip, J. and Segiun, H., Appl. Phys. Lett., 23, 135 (1973)
- 32. Stricker, J. and Parker, J., J. Appl. Phys., 53, 851 (1982)
- 33. Diaber, J. and Winans, J., J. Opt. Soc. Amer., 58, 76 (1968)
- 34. Hacker, M., Cohn, D., Lax, B., Appl. Phys. Lett., 23, 392 (1973)
- 35. Telle, H. and Laureau, A., Opt. Comm., 34, 287 (1980)

36.

37.

38.

39. 40.

41.

42.

43.

44.45.

46.

47.

48.

49.

50.

51.

52.

53.

54.

55.

- 36. Biswas, A., Latifi, H., Radziemski, L., Armstrong, R., Opt. Lett., 12, 313 (1987)
- 37. Barnes, P. and Rieckhoff, K., Appl. Phys. Lett., 13, 282 (1968)
- 38. Chitanvis, S., Appl. Opt., 25, 1837 (1986)
- 39. Pendelton, J., Appl. Opt., 24, 1631 (1985)
- 40. Carls, J., Brock, J., J. Opt. Soc. Amer., 13,273 (1988)
- 41. Carls, J., Brock, J., Opt. Lett., 13, 919 (1988)
- 42. Essien, M. and Radziemski, L., J. Atom. Anal. Spectrom., 3, 985 (1988)
- 43. Kumar, V. and Thareja, R. K., J. Appl. Phys., 64, 10 (1988)
- 44. Brown, R. T. and Smith, D. C., Appl. Phys. Lett., 22,245 (1973)
- 45. Smith, D. C., J. Appl. Phys., 41, 4501 (1970)
- 46. Williams, W. E., Soileau, M. J., Van Stryland, E. W., Appl. Phys. Lett., 43, 352 (1983)
- 47. Smith, D. C. and Fowler, M. C., Appl. Phys. Lett., 22, 500 (1973)
- 48. Morgan, C. G., Rep. Prog. Phys., 38, 621(1975)
- 49. C. Grey Morgan, C. Grey Morgan, *Electrical Breakdown of Gases*, by Meek, J. M. and Craggs, J. D., eds., chapter 9, Chichester, NY, Wiley, 1978
- 50. Voronov, G. S. and Delone, N. B., Soviet Phys. JETP, 23, 54(1966)
- 51. Bekefi, G., Principles of Laser Plasmas, Wiley, NY, chapter 11, 1978
- 52. Brown, C., Ekberg, J., Feldman, U., and Seely, J. F., J. Opt. Soc. Am., 4B, 533 (1987)
- 53. Dietze, H. J., Becker, S., Int. J. Mass Spectrom. Ion Process., 1, 82 (1988)
- 54. Toubhans, I, Fabbro, R., Gauthier, J. C., Chaker, M., Pepin, H., Proc. SPIE. Int. Soc. Opt. Eng., 1140, 358 (1989)
- 55. Laporte, P., Damany, N., and Damany, H., Opt. Lett., 12, 987 (1987)

- 56. Key, M. H., Plasma Phys. Controlled Fusion, 26, 12A, 1383 (1984)
- 57. Eason, R. W., Bradley, D. K., Hares, J. D., Rankin, Andrew, J., Tabatabaei, S. D., Lunney, J. G., Cheng, P. C., Feder, R., Michette, A. G., et al., Proc. SPIE-Int. Soc. Opt. Eng., 664, 161 (1986)
- 58. Kubiak, G., Outka, D., Rohlfing, C., Zeigler, J., Windt, D., Waskiewicz, W., J. Vac. Sci. Technol., B, 8(6), 1643 (1990)
- 59. Bobin, J. L., Floux, F., and Tonon, G., Plasma Phys. Contr. Nucl. Fusion Res. 8463 (17235), 363 (1971)
- 60. Radziemski, L. J, Loree, T. R., Plasma Chem. Plasma Proc., 1(3), 271 (1981)
- 61. Radziemski, L. J, Loree, T. R., Plasma Chem. Plasma Proc., 1(3), 281 (1981)
- 62. Cremers, D. and Radziemski, L., Anal. Chem., 55, 1252 (1983)
- 63. Sittig, M., Hazardous and Toxic Effects of Industrial Chemicals, Noyes Data Corp., Park Ridge, NJ, 1979
- 64. Cremers, D. and Radziemski, L., Appl. Spec., 39, 57 (1985)
- 65. Cremers, D., Radziemski, L., Loree, T., Appl. Spec., 38, 721 (1984)
- 66. Archontaki, H. A. and Crouch, S. R., Appl. Spec., 42, 741 (1988)
- 67. Wiegand, P. and Crouch, S., Appl. Spec., 42, 567 (1988)
- 68. Ottensen, D., Wang, J., Radziemski, L., Appl. Spec., 43, 967 (1989)
- 69. Cremers, D., Appl. Spec., 41, 572 (1987)
- 70. Millard, J., Dalling, R., Radziemski, L., Appl. Spec., 40, 491 (1986)
- 71. Majidi, V., Ratliff, J., Owens, M., Appl. Spec., 45, 473 (1991)
- 72. Majidi, V., Rae, J. T., and Ratliff, J., Anal. Chem., 63, 1600 (1991)
- 73. Joseph, M. R. and Majidi, V., J. Trace and Microprobe Techniques, 10, 207 (1992)
- 74. Majidi, V. and Joseph, M. R., Crit. Rev. in Anal. Chem., 23, 143 (1992)
- 75. Majidi, V., Spectroscopy, 8(3), 16(1993)

76. Raziemski, L. J. and Cremers, D. A., Laser-induced Plasmas and Applications, Marcel Dekker, New York, 1989

CHAPTER 3

INSTRUMENTATION

A. Introduction

The first section of this chapter describes the general experimental setup for all the carbon rod atomization laser-induced breakdown spectrometry (CRALIBS) experiments described within this dissertatation. The main components of the setup are the laser, optics to focus the laser pulse and to image the emission on the detection system, the carbon rod atomization (CRA) chamber used for sample introduction, the signal processing system, and an IBM PC-XT compatible computer. The basic apparatus remained the same throughtout these studies, with only minor modifications implemented to improve stability and detection. Figure 3-1 illustrates the general experimental setup.

The second section of this chapter describes the general conditions used for data collection. Many experimental parameters remained constant throughout this dissertation and are presented in tabular form at the end of this chapter.

The sequence required for operation is simple. A laser pulse produced every 100 milliseconds is focused by a planoconvex lens to the diffraction limit inside the atomization chamber. At the focal point, the electric field produced exceeds the dielectric strength of the surrounding atmosphere, and breakdown occurs. Because the laser pulse is finite in time (10 nanoseconds), the plasma created is transient in nature. At some point, the laser beam is momentarily blocked so a

sample can be introduced into the carbon rod atomization (CRA) chamber. The CRA is subsequently heated to initiate the atomization cycle. The generated atomic vapor is transported by argon carrier gas through the laser plasma. Analyte emission from the plasma is imaged onto the entrance slit of the monochromator, and detected using a photomultiplier tube transducer. The time variant signal is detected using a boxcar averager. The output of the boxcar averager is digitized and stored with a computer data acquistion system.

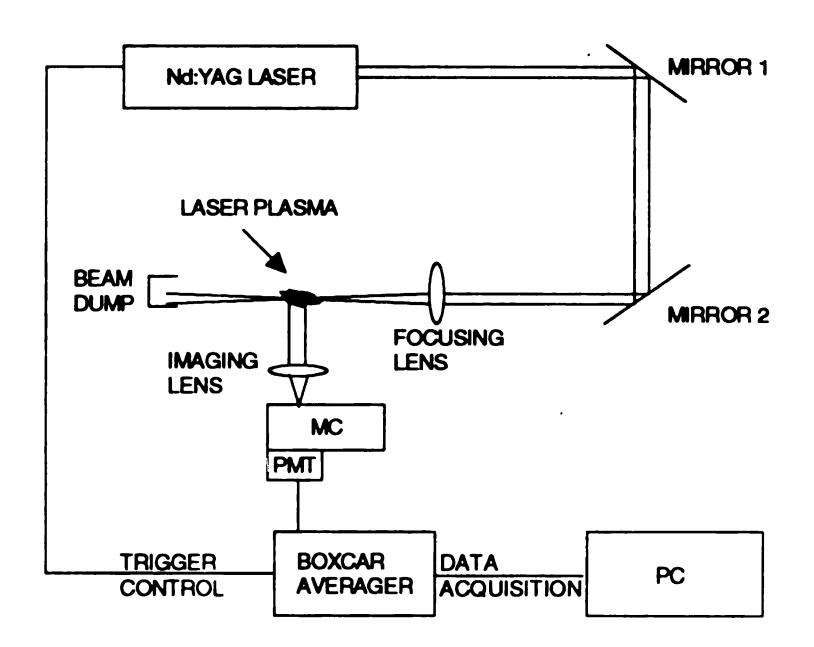


Figure 3-1. Experimental Setup. MC=monochromator, PMT=photomultiplier tube, and PC=personal computer.

B. Experimental Setup

A pulsed Nd:YAG Q-switched laser (Model GCR-11, Spectra Physics, Mountian View, CA) was used to generate the plasma. The fundamental wavelength (1064 nm) of the laser was used for all experiments.

However, frequency doubling of the laser allowed precise alignment of the laser beam inside the CRA. With a maximum power of 275 mJ/pulse at the fundamental wavelength, the laser had sufficient power to generate the plasma under all experimental conditions described. The nominal pulse duration of the laser was 10 nanoseconds. The repetition rate of the laser was variable with a maximum repetition rate of 15 pulses per seconds (pps). The optimum rate is 10 pps for best reproducibility of pulse energy. All experiments were performed using 10 pps unless otherwised stated. The average power of the laser was continuously monitored by placing a beam splitter in the optical path and directing one-tenth of the pulse energy at a pyroelectric detector (Ophir Optics, Jerusalem, Israel).

Two silver coated mirrors (Newport-Klinger, Irvine, CA) were used to direct the laser light into the atomization chamber (see Figure 3-2). This configuration gave the greatest degree of freedom for alignment, and the lowest probability of direct back reflection of the laser light into the cavity of the laser. Cardboard boxes with orthogonal entrance and exit holes were used to cover the mirrors. This minimized stray reflections and provided a place to mount the beam block required for sample introduction. The beam block was made from a metal box (10 cm x 7 cm x 8 cm) wrapped with black felt to absorb the laser radiation.

The carbon rod atomization (CRA) chamber, shown in Figure 3-2, was designed to provide flexible operation and maximal viewing of the laser plasma. The CRA consists of a square aluminum outer body with three quartz windows (ESCO Products, Inc., Oak Ridge, NJ) 25.4 mm in diameter, a plano-convex focusing lens, a PIN photodiode detector, and a

beam stop mounted on the outside of the chamber othogonally to one another.

The laser light was focused by a plano-convex lens (f=50 mm). The focal point of the lens was directly above where the sample was placed on the carbon rod (see below). The beam dump was made from a stack of razor blades mounted in a box, and was placed outside the opposite quartz window in the optical path to absorb excess laser radiation.

The PIN photodiode (hp 5820-4220, Hewlett Packard, San Jose, CA) monitored the blackbody emission from the carbon rod. The current generated by the PIN photodiode was converted to a voltage and displayed on a digital multimeter (Fluke Model 8000A, John Fluke Mfg., Seattle, WA).

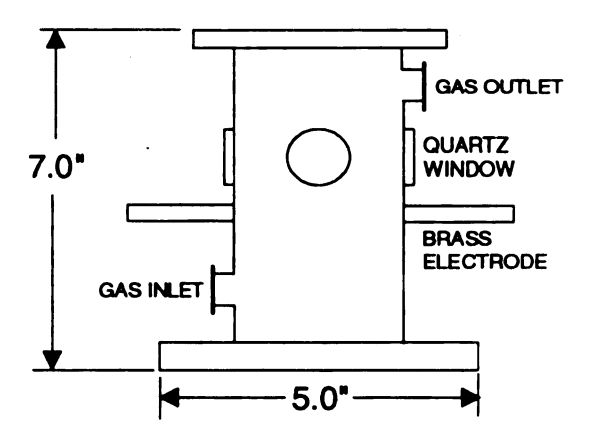


Figure 3-2. Atomization Chamber.

An optical pyrometer (Pyro Micro-Optical Pyrometer, The Pyrometer Instrument Co., Inc., Northvale, NJ) was used to calibrate the PIN photodiode detector response. Recalibration of the detector was performed periodically to ensure temperature integrity. The photodiode

was also recalibrated after any modification done inside the atomization chamber. The photodiode was capable of detecting blackbody radiation from the carbon rod at temperatures as low as 700° C. The calibration curve (y=13003x²-1305.6x+904.4) is presented in Figure 3-3. At temperatures below 700° C, the voltage drop across the CRA was used to indirectly determine the CRA temperature. Figure 3-4 shows the relationship between the CRA temperature and the voltage drop. The voltage drop is related to the CRA temperature by the equation, y=1548.9x-519.44, r^2 =0.991. This equation is used to extrapolate back to determine the temperature of the CRA.

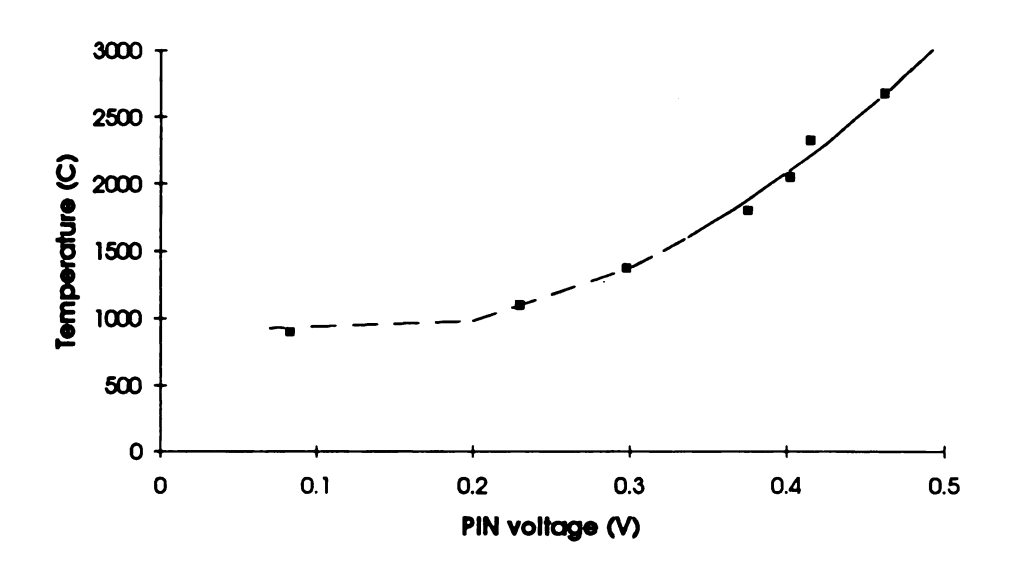


Figure 3-3. PIN Photodiode Detector Calibration Curve

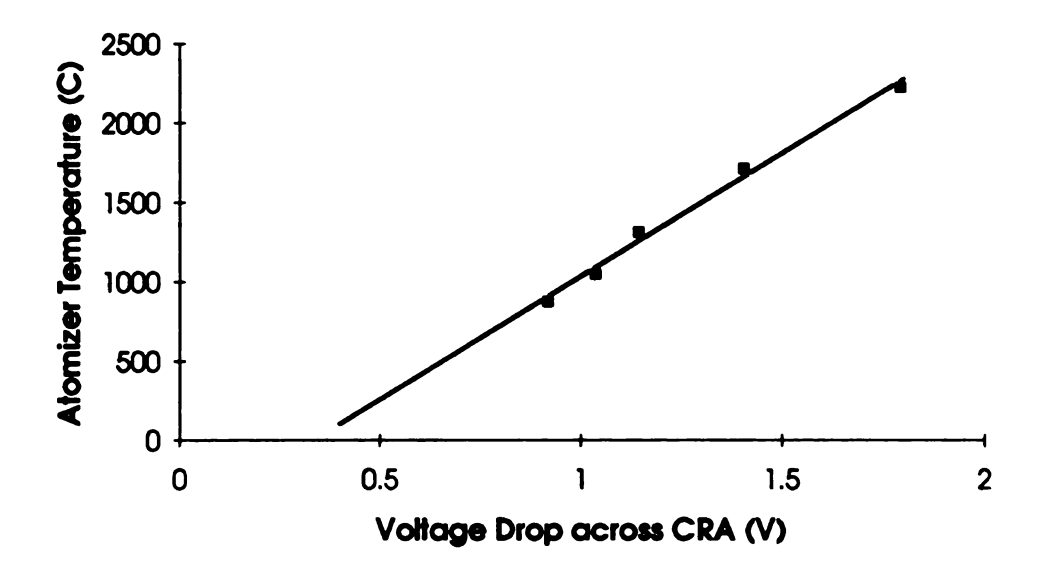


Figure 3-4. CRA Voltage Drop Calibration Curve

A carbon rod stand made from brass was constructed to mount the carbon rod inside the main body of the CRA chamber. The brass stand is illustrated in Figure 3-5. The base of the stand was made from a high melting point hard phenolic plastic to provide electrical insulation from the aluminum body. A small groove on top of each brass structure provided reproducible mounting of the carbon rod. The carbon rod was clamped into position by two brass plates.

The carbon rods used in all the experiments were high purity graphite rods (2.3 mm diameter x 21.5 mm length) originally manufactured (Bay Carbon, Inc., Bay City, MI) for a direct-current plasma (DCP) instrument. Each carbon rod was notched in the center to allow for reproducible sample placement. The sample was introduced through a 1.5 mm diameter hole in the top of the atomization chamber using a 5 µL syringe (Model 7105, Hamilton Corporation).

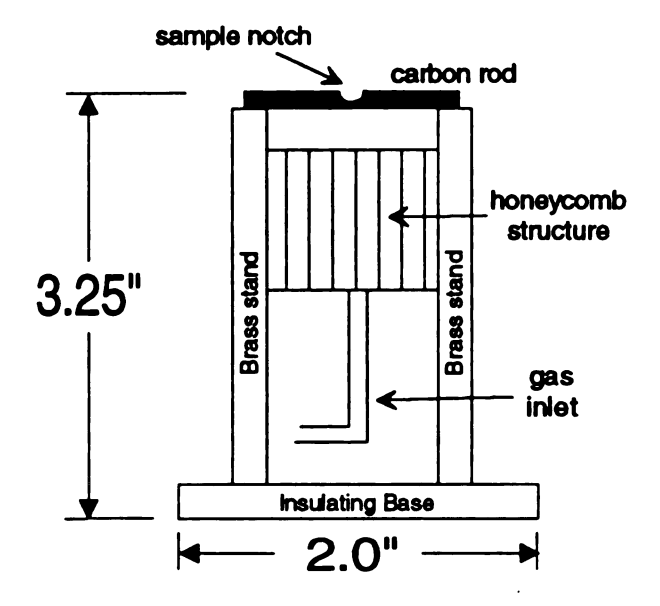


Figure 3-5. Carbon Rod Stand.

Illustrated in Figure 3-6 is a honeycomb structure made from capillary tubes (1.5 mm diameter and 2.0 mm length) that was positioned 10 mm below the carbon rod to promote a laminar flow of sheath gas across the carbon rod. This primary flow of argon transports the atomic vapor into the laser plasma. An auxiliary flow of argon was directed into the main body of the chamber to purge trapped oxygen. All the windows, the top and bottom of the chamber, and the focusing lens were fitted with O-ring seals to maintain the inert atmosphere inside the CRA chamber.

For analytical applications, a glass chimney structure was used to increase transport efficiency and reproducibility of the atomic vapor to the laser plasma. The chimney structure is shown in Figure 3-7.

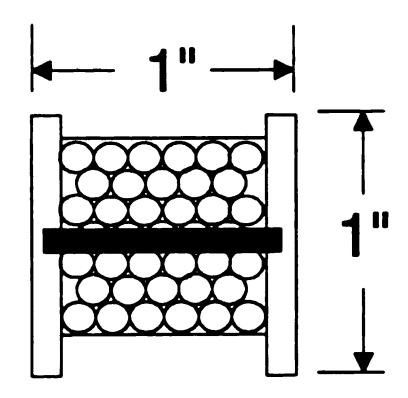


Figure 3-6. Honeycomb Structure.

The chimney was made from two different diameters of glass tubing. The larger diameter glass tube (46 mm) was placed over the brass stand while the smaller diameter glass tube (20 mm) was above the carbon rod. This forced the argon flow through the laser plasma, thus increasing transport efficiency and reproducibility. Three 8 mm holes were drilled in the chimney in order to gain optical access for the laser and collection of the plasma emission.

A commerically available power supply (HGA-2100, Perkin-Elmer, Norwalk, CT) was used for heating the carbon rod. The power supply is rated for a maximum output of 440 amperes at 5 volts. The power supply was manufactured for use with the HGA-2100 graphite furnace. The design of the CRA attempted to match resistances of the CRA (1 Ω) with the graphite furnace (0.4 Ω). Although the CRA has a higher resistance, no problems were encountered using this power supply. Electrical connection to the carbon rod was made through brass electrodes that connected to the brass stand inside the atomization chamber. Telfon spacers provided electrical insulation of the electrodes from the outer body of the chamber.

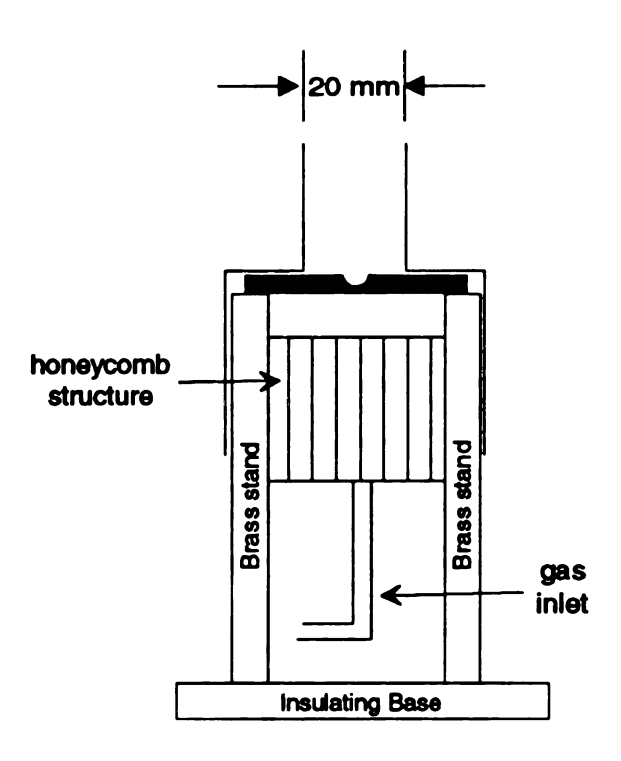


Figure 3-7. Glass Chimney attachment for Brass Stand

A quartz lens (f/4) perpendicular to the laser optical path imaged the plasma emission onto the entrance slit of a Czerny-Turner monochromator (Heath-McPherson, model EU-700/E, Benton Harbor, MI) equipped with a UV-Visible (200 -700 nm) sensitive photomultiplier tube (PMT) transducer (Model IP28A, Hamamastu Corporation, Bridgewater, NJ). For applications that required detection of analyte emission in the near-infrared (NIR), a red sensitive PMT transducer (Model R666, Hamamastu Corporation, Bridgewater, NJ) was employed.

A boxcar averager (Model 162, Princeton Applied Research, Princeton, NJ) and gated integrator (Model 164, Princeton Applied Research, Princeton, NJ) provided time discrimination of the detector signal. The boxcar averager was triggered by an external signal generated by the power supply of the laser. This trigger pulse coincided

in time with pulsing of the Pockels cell (the Q-switch) inside the laser cavity to release the laser pulse. The rise time of the trigger pulse (0 \rightarrow +5 V) was 20 nanoseconds. All time delays reported are relative to this trigger.

However, all time delays are retarded by 75 ns. This is due to the finite internal switching circuitry of the boxcar averager. A delay line was not used since this amount of time is insignificant on the microsecond time scale. Data acquisition of the signal from the boxcar output was accomplished by using a Data Acquisition Control Adapter (DACA) board (IBM Corporation, Boca Raton, FL) in a PC-XT compatible. The interrupt-driven data acquisition software (1) was written in Macro Assembler, Version 5.0 and Microsoft QuickBASIC version 4.0 (Microsoft Corporation, Redmond, WA). The IBM-DACA board was triggered for data collection by the HGA-2100 power supply at the start of the atomization cycle. The generated trigger pulse was altered in order to be compatible with the data acquisition board. The acquistion board requires falling edge trigger ($+5 \rightarrow 0$ V). The circuit schematic shown in Figure 3-8 transformed the existing HGA-2100 power supply trigger (+11 \rightarrow +1 V) into the necessary falling edge trigger required for the acquisition board. All atomization cycle times are relative to this trigger.

C. Experimental Conditions

The general experimental conditions used for all experiments are presented in Table 3-1. Unless stated to the contrary, the results in this dissertation have been collected under these conditions. There are several variables optimized for each experiment. The pulse energy of

the laser is optimized based on all the other experimental parameters. The pulse energy ranged from 3-5 MW/pulse unless otherwise stated.

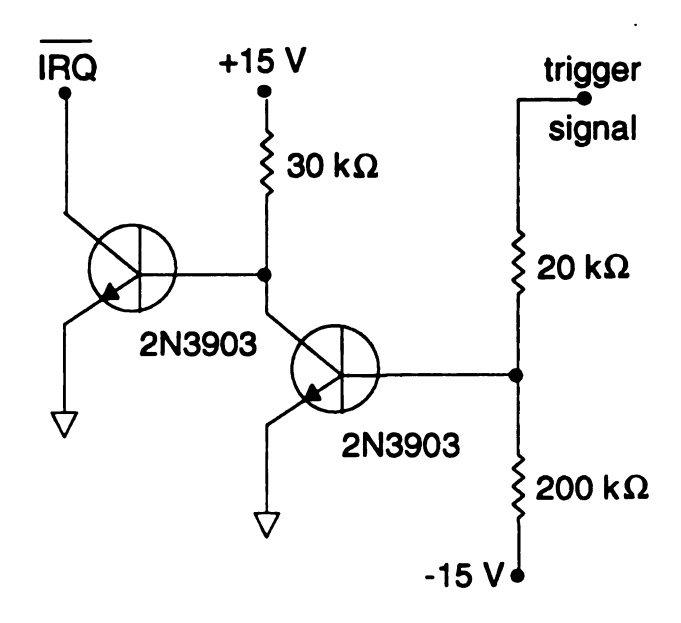


Figure 3-8. Circuit Diagram for Trigger Conversion.

The CRA heating cycle times were constant for all experiments. The desolvation or charring stages were not used until the analysis of real samples were performed. In that case, specific experimental parameters are stated. The atomization temperature was specific for each element analyzed based on literature values (2) and individual experimental results. For each determination, the atomization temperature is reported. The sample size used was constant at 5 µL.

The primary argon flow rate through the honeycomb structure was highly variable. There was a minimum flow rate required for reproducible transport of the analyte vapor to the laser plasma which was dependent on many experimental parameters. For most of the

experiments, the primary flow rate was 1.5 liters/minute. However, an entire chapter (see chapter 5) has been devoted to the effect of experimental parameters on the characteristics of the laser plasma. In this chapter, several flow rates were used and are specifically reported.

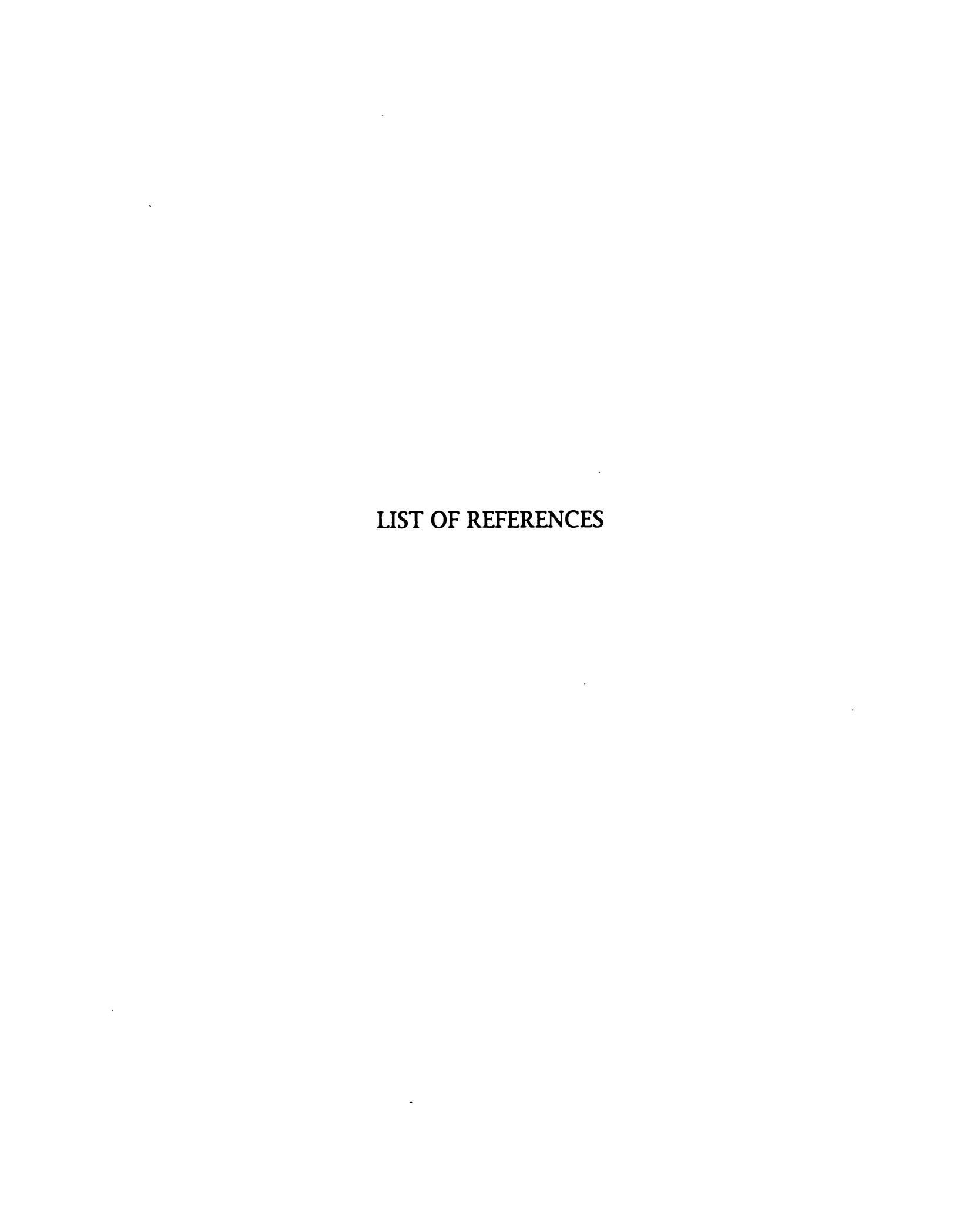
The parameters on the boxcar averager were varied according to the type of experiment. In order to preserve time resolution, the aperture duration was changed to 50 nanoseconds when temporal studies of the plasma characteristics were studied. For analytical determinations, the time duration was increased to 0.5 µs for a longer integration time. For all studies, the output time constant remained at 0.1 ms. Triggering of the boxcar was provided by the laser power supply. This method of triggering provided very reliable and reproducible The gated integrator parameters were not changed for any experiments. The parameters chosen were based on initial studies of the laser plasma which determined that a time constant larger than 1 us on the gated integrator distorted the output signal. The 1 M Ω input resistance of the gated integrator provided conversion of the PMT current from the photomultiplier tube to the working range voltage of the boxcar. The exponential averaging mode was chosen because this mode of operation best represents the input signal at the output.

The plasma was formed 6 mm above the surface of the carbon rod. This initial height was chosen based on previous experiments. The objective was to form the laser plasma close to the carbon rod in order to increase transport efficiency of the analyte vapor. However, the heating of the carbon rod in the atomization cycle affects the plasma characteristics as discussed in chapter 5. As a result, the plasma height

was moved to 10 mm for analytical determinations. The problem with moving the plasma further away from the carbon rod was a decrease of transport efficiency and reproducibility of the analyte vapor into the plasma. This problem was overcome by using the glass chimney structure.

 Table 3-1.
 Summary of Experimental Parameters

Laser	Quanta-Ray GCR-11 Nd:YAG
wavelength	1064 nm
nominal pulse duration	10 ns
repetition rate	10 pulses/second
pulse energy	20 -100 mJ/pulse
CRA Heating Conditions	
drying time	0 seconds
charring time	0 seconds
atomization time	8 seconds
sample size	5 μL
Argon Flow Rate	
primary flow rate	1.5 liters/minute, but highly variable
auxiliary flow rate	0.5 liters/minute
Signal Processing	
boxcar averager	PAR 162
aperture delay time	5-250 µs
aperture duration time	50 ns or 0.5 μs
trigger	external from Q-switch of laser
output time constant	0.1 ms
Gated Integrator	PAR 164
input resistance	1 ΜΩ
integrator time constant	1 μs
averaging mode	exponential
Height of Plasma Above Carbon Rod	6 mm or 10 mm



LIST OF REFERENCES

References:

- 1. Bowman, L., Victor, M., Crouch, S., Trends in Anal. Chem., 9, 111 (1990)
- 2. Fuller, C. W., Electrothermal Atomization for Atomic Absorption Spectrometry, Burlington House, London, England, 1977

CHAPTER 4 CHARACTERIZATION OF ARGON LASER PLASMA

A. Introduction

Laser plasmas are characterized by their physical dimensions, lifetime, excitation temperature, electron density, and ionization temperature. These characteristics depend on the laser wavelength, the amount of power, pulse duration, the optics employed, and the surrounding atmosphere in which the plasma is formed. It is no wonder that only general features are ever reported for a specific system.

The excitation temperature of an emitting source can be determined assuming that it is in Local Thermodynamic Equilibrium (LTE) where a Boltzmann distribution of electronic states of atoms and molecules is followed for a given temperature at a local area in the source. Emission intensity ratios from different upper energy levels of a thermometric element (1) in the same electronic state in a source are most frequently used to calculate the excitation temperature of a source.

The other parameters that describe the physical characteristics of a plasma are the ionization temperature and electron density. The ionization temperature is determined by the ratio of intensities of ion-to-neutral emission lines of the same element using the Saha relationship (1), which describes the basic mass action law of the ionization equilibrium. For each component in a plasma an equilibrium exists between the neutral atom and various ionized species (singly charged, doubly charged, etc.), depending on the degree of ionization of the plasma. In order to calculate an ionization temperature, the electron pressure of the plasma must be determined.

This chapter first discusses how the excitation temperature, electron density, and ionization temperature are calculated. The second section of the chapter presents and discusses the results obtained experimentally for each characteristic. As discussed in the previous chapter, time discrimination was performed using a boxcar averager This provides time-resolution on the with a gated integrator. microsecond scale. All time delay values reported within this chapter are relative to the trigger produced by the laser employed. This trigger is produced with each laser pulse used to create the plasma. There is a 75 nanosecond difference in the values quoted and the actual time delay. The difference arises due to the finite switching time of the boxcar averager used for all experiments. All temperatures and electron densities are spatially averaged over the plasma. Cremers and Radziemski (2) have determined that unfolding the plasma emission using an Abel inversion resulted in less than 5% difference from the spatially averaged determinations. All measurements were made using analytical grade argon gas at atmospheric pressure and room temperature.

B. Determination of Excitation Temperature

If the source is optically thin (i.e. negligible self-absorption), the intensity for a spectral line either from an atom, ion, or molecule is given by,

$$I_{av} = KA_{av}n_ahv_{av}$$
 Equation 4.1

where K is a proportionality constant dependent on the area of the source viewed, A_{00} is the Einstein coefficient or transition probability in

s⁻¹ of the emission from an upper state, q, to lower state, p, $n_{\rm q}$ is the population number density (cm⁻³) of the upper state, h is Planck's constant, and $v_{\rm qp}$ is the frequency of the emission. Assuming the plasma is in thermal equilibrium, the population of the upper state is given by the Maxwell-Boltzmann Equation:

$$n_q = \frac{ng_q}{Z}e^{-\frac{\varepsilon_q}{kT}}$$
 Equation 4.2

where n is the total population number density (cm⁻³), g_q is the statistical weight of the upper state, q, Z is the partition function, ε_q is the energy of the upper state relative to the ground state, k is Boltzmann's constant, and T is the excitation temperature of the plasma. Combining Equations 4.1 and 4.2, rearranging, and taking the natural logarithm the working Equation is obtained:

$$\ln\left(\frac{I_{qp}}{hv_{qp}g_qA_{qp}K}\right) = \ln\left(\frac{n}{Z}\right) - \frac{\varepsilon_q}{kT}$$
 Equation 4.3

A plot of $\ln [I_{qp} / (hv_{qp} g_q A_{qp} K)]$ versus ε_q should give a slope of -1/kT and an intercept of $\ln(n/Z)$ for a group of spectral lines emitted by atoms, ions, or molecules of one and the same kind. This is better known as a Boltzmann plot. An accurate excitation temperature can be obtained from the plot if there is no self-absorption of any of the lines, if the energies of the upper states cover a broad range, and if accurate transition probabilities are known. The major limitation in using this method is having spectrally resolved lines that cover a large energy range in which the transition probabilities are well studied.

C. Determination of the Ionization Temperature

Another parameter that is useful in describing a plasma, especially when highly ionized, is the degree of ionization or ionization temperature. The ionization temperature is calculated based on the degree of ionization of the plasma in conjunction with the ion-to-atom intensity ratio of the same element. The degree of ionization of the plasma is calculated by determining the electron density, or electron pressure. The electron pressure and ion-to-atom ratios determine the ionization temperature according to the Saha Equation below:

$$\log p_{\epsilon} = -\log \left(\frac{I_{qp}^{+}}{I_{qp}}\right) + \log \left(\frac{g_{qp}^{+}A_{qp}^{+}v^{+}}{g_{qp}A_{qp}v}\right) - \frac{5040}{T} \left(IE + \varepsilon_{q}^{+} - \varepsilon_{q}\right) + \frac{5}{2}\log(T) - 6.18$$

Equation 4.4

where p_e is the electron pressure in atmospheres, the superscripts (+) indicate the ion, ν is the frequency of the transition in Hz, T is the ionization temperature in Kelvin, $I\!E$ is the ionization energy of the atom in eV, ϵ_q is the energy level above the ground state of the atom or ion in eV. In the above equation, the electron pressure and ionization temperature are unknown. Thus, another independent equation is required. The second Equation is based on calculation of the electron pressure using the ideal gas law. Assuming one mole of gas, the electron pressure (in atmospheres) is equal to:

$$p_e = \frac{N_e T}{7.34 \times 10^{21}}$$
 Equation 4.5

where N_{Θ} is the electron density in cm⁻³, and T is the temperature in Kelvin. These two Equations must be solved recursively for the singular solution that represents the ionization temperature for a given ion-to-atom ratio and electron density.

D. Determination of the Electron Density

At times early in the plasma, the dominant mechanism of linebroadening is Stark broadening caused by perturbations of the electric field of the radiator from other atomic, ionic, or molecular species that contain a permanent dipole moment (3,4). Doppler broadening is insignificant compared with Stark broadening because of the high degree of ionization in the plasma. A convenient and well-known way to measure the electron density is by using the Stark widths of various hydrogen lines (4). The theoretical Stark profiles for hydrogen, neutral helium, and ionized helium emission lines are well known. Since these lines undergo a linear Stark effect (4), the full-width at half maximum of these lines raised to the 1.5 power is proportional to the electron density, i.e. $N_e = C(N_e, T)W^{3/2}$ where N_e is the electron density in cm⁻³, C(N_e,T) is a coefficient that is a weak function of the electron density and temperature, and W is the full Stark width. This equation assumes that the second ionization equilibrium is not important. The useful hydrogen lines (Balmer series) are H_{α} (6563 Å) for electron densities as high as 10^{19} cm⁻³, H_B (4861 Å) for electron densities between 10^{15} to 10^{17} cm^{-3,} and H_{γ} (4340 Å) for electron densities about 10^{17} cm⁻³ or when another line is not usable. Using the Stark broadened hydrogen lines to determine the electron density routinely results in errors less than 10%. The full-width at half maximum for the H_B line is 56.5 Å for a plasma

having an electron density of 10¹⁸ cm⁻³ and a temperature of 15000 K. When the above lines are not spectrally resolved, calculations of the electron density must be made using emission lines of heavier elements. Because the theoretical Stark profiles are not well known for heavier elements and are not as sensitive to changes in electron density, errors in the determination can be as high as 50%.

Other methods for determining the electron density of a plasma are based on interferometric measurements of optical dispersion (4), and measurements of absolute line and background continuum intensities (1,4). Interferometric techniques are the most reliable since they are independent of plasma composition and temperature. The absolute line and background continuum measurements depend heavily on detector calibration, and are useful only at moderate electron densities (approximately 10^{15} cm⁻³).

E. Measured Characteristics of the Laser Plasma

1. Physical Dimension of the Plasma

The physical dimensions of the laser plasma depend on the laser fluence, the focal length of the lens employed, the atmosphere in which it is produced, and the pressure of the surroundings. As the laser fluence increases above the breakdown threshold, the plasma grows toward the laser beam. An upper limit was found to the amount of power used to create the plasma. Above this limit, plasma formation became very erratic with nodes developing within the plasma. This resulted in an unstable plasma that was not analytically useful. Typically, the plasma was formed in argon at atmospheric pressure using

a 5 cm focal length planoconvex glass lens to focus a 10 nanosecond IR (1064 nm) laser pulse with a pulse energy of 4 MW/pulse. Under these conditions, a cylindrically symmetric plasma resulted that was 15 mm in length (along the axis of the laser beam) and 2 mm in diameter.

2. Background Emission Characteristics of the Plasma

The background emission of the laser plasma is most intense after formation and nearly exponentially decays. Figure 4-1 depicts the decay of background emission at the Ca(II) 3933.95 Å ion line and at various time delays. Background emission was detected at time delays as long as 400 µs after plasma formation. Because the background emission is initially very intense, time discrimination of the analyte signal increased the signal-to-background of the analyte emission.

The background spectrum from 2000 to 5000 Å is shown in Figure 4-2. The spectrum was collected 10 µs after plasma formation. Two main features are predominant in the plasma background spectrum. First, the background spectrum of the argon plasma is very rich due to argon ionic emission. Second, outside the 2000 to 5000 Å region, only background continuum radiation is observed, i.e., they are spectral free regions. Peak background continuum emission is observed at 3500 Å.

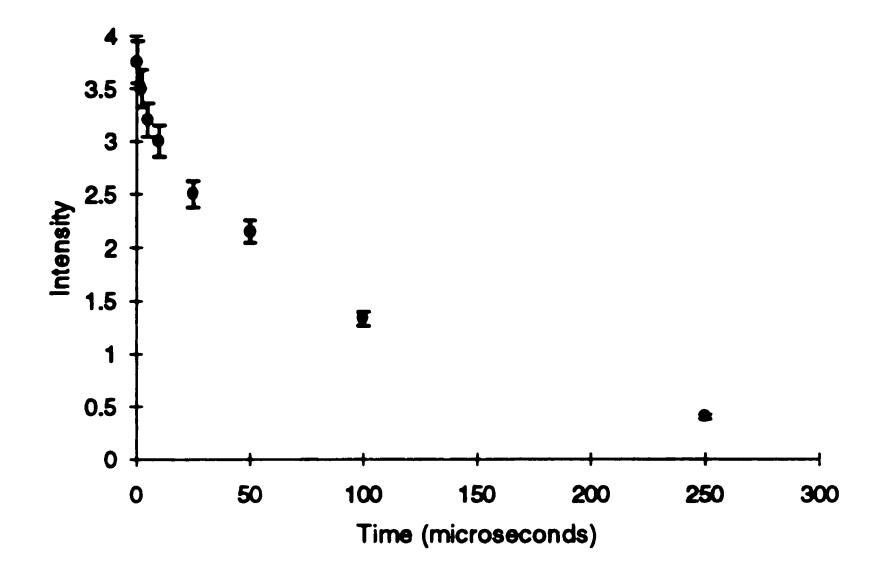


Figure 4-1. Background Continuum Emission Decay for the Laser Plasma.

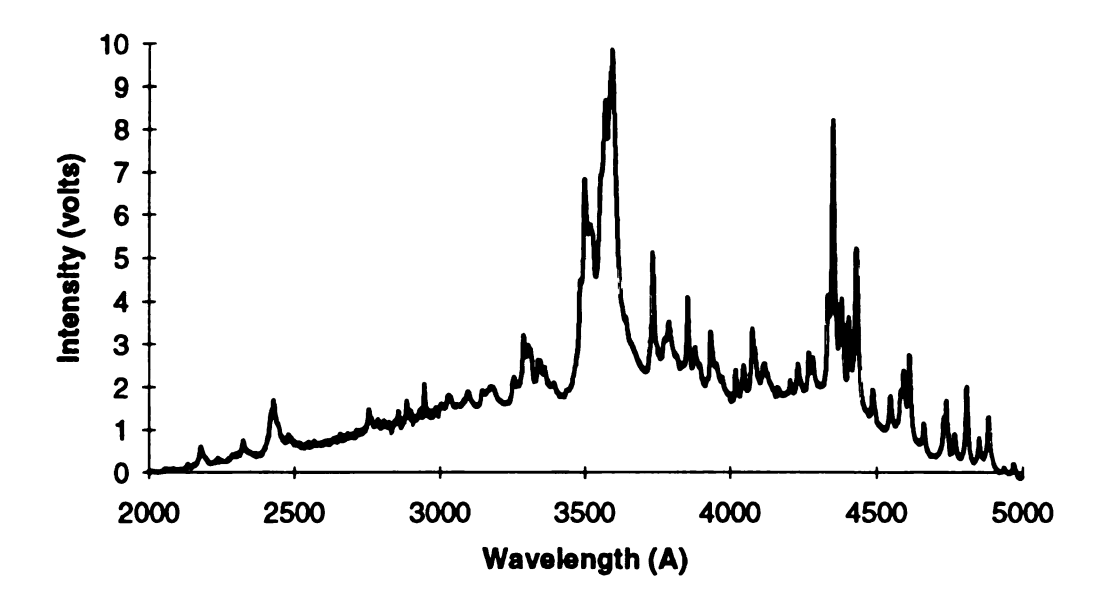


Figure 4-2. Argon Background Spectrum. Time Delay = $10 \mu s$.

The background continuum emission results from two sources, bremsstrahlung and radiative recombinations. Bremsstrahlung is a free-

free transition of electrons moving in an electric field of an ion with the emission of a photon. Radiative recombination occurs when free electrons recombine with ions to a bound state with emission of a photon. The plasma was so highly ionized that atomic emission from argon was weakly observed. In Figure 4-3, the expanded region between 4000-4300 Å represents the only argon atomic emission detected. Atomic emission developed after 25 µs and is located in the region between 4150-4300 Å. Peak atomic emission occurred at 50 µs, and decayed rapidly into the baseline at times greater than 50 µs.

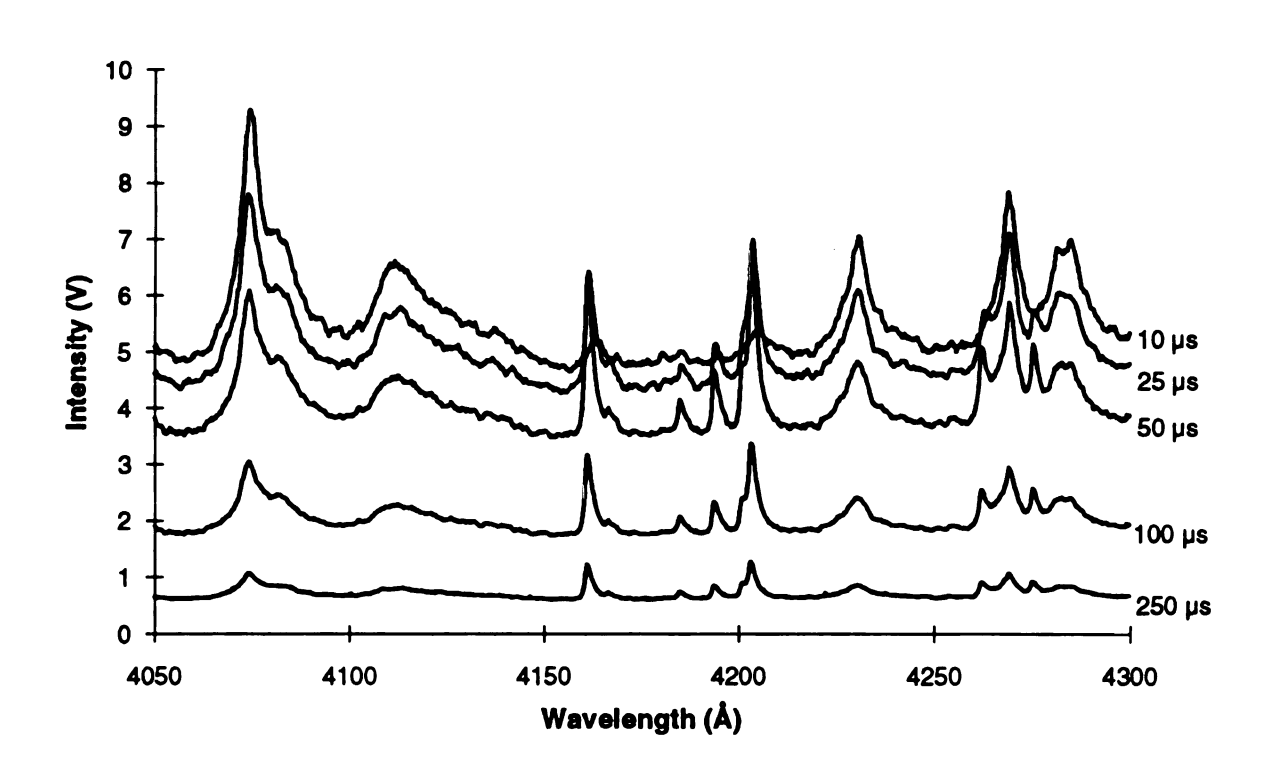


Figure 4-3. Expanded Argon Background Spectrum at Various Time Delays.

To put this in perspective, the emission line at 4158 Å is the most intense atomic argon emission line present in an ICP source (5). The

most intense emission in the laser plasma was a convolution of a group of singly ionized argon lines located in the region between 3500 Å and 3700 Å. Another feature of the background spectrum is the observed line widths. Full-width at half-maximum (FWHM) of argon ionic emission lines ranged from 5-9 Å. In comparison, the ICP has line widths for argon atomic emission that range from 0.1-0.2 Å.

3. Time-resolved Excitation Temperatures of the Plasma

The time-resolved excitation temperature was determined from a Boltzmann plot using a group of argon atom lines. An average excitation temperature of 5700 K was calculated. The atomic lines used for the determination of the excitation temperatures are tabulated in Table 4-1. The lines used were spectrally resolved. The calculated excitation temperatures are presented in Table 4-2.

Because the relative intensity of the argon atomic emission was very weak and the energy spread in the upper state of the lines used was narrow (see Table 4-1), the calculated excitation temperatures are quite imprecise. The average uncertainty in temperature is greater than 150%. Because this method of determining the excitation temperature of the plasma was very inaccurate, the ratio of ionic emission from argon were used.

Table 4-1. Argon Atomic Line Parameters.

Wavelength (Å)	E(eV)	g(upper)	Transition probability (s ⁻¹)
4158.6	14.540	5	1.45 x 10 ⁻¹⁰
4181.9	14.699	3	5.80 x 10 ⁻¹¹
4200.7	14.511	7	1.03 x 10 ⁻¹⁰
4259.4	14.749	1	4.15 x 10 ⁻¹⁰
4266.3	14.540	5	3.33 x 10 ⁻¹¹
4272.2	14.536	3	8.40 x 10 ⁻¹¹

Table 4-2. Determination of Excitation Temperature from Boltzmann Plot of Argon Atom Emission Lines.

time delay (µs)	Temperature (K)	%RSD
5	†	†
10	†	†
25	5953	198
50	4587	115
100	4799	123
250	7365	191

[†] No detectable atomic argon emission

Since the predominant features of the background are argon ion lines, the time-resolved excitation temperatures were determined using a group of these in the region 4300-4800 Å. Table 4-3 lists the ionic line parameters used for the determination. These emission lines were selected because they were spectrally resolved and covered a narrow wavelength interval where detector response was nearly constant. However, emission intensities were normalized for slight changes in detector response over the wavelength interval.

Table 4-4 shows the calculated time-resolved excitation temperatures obtained by using this group of argon ion lines. maximum excitation temperature occurred 50 µs after plasma formation. The average uncertainty in the determination was 27.4%. The lower uncertainty is due to the larger energy spread in upper energy levels for the group of lines used and the higher intensity of the ionic emission compared to the atomic emission. The calculated temperature is more accurate using the group of argon ion lines because of the larger differences in the upper energy levels for the ion lines as compared to the atom lines. This difference creates a larger population difference for the upper energy levels for the argon ion lines which gives a greater difference in the emission intensities observed for each transition. The uncertainty reported here is similar to other plasmas.

 Table 4-3.
 Argon Ionic Line Parameters.

Wavelength (Å)	E(eV)	g(upper)	Transition probability (s-1)
4348.1	19.510	8	1.24 x 10 ⁻⁸
4379.7	19.658	2	1.04 x 10 ⁻⁸
4401.0	19.238	6	3.22 x 10 ⁻⁹
4481.8	21.515	6	4.94 x 10 ⁻⁹
4545.1	19.883	4	4.13 x 10 ⁻⁹
4589.9	21.143	6	8.20 x 10 ⁻⁹
4609.6	21.160	8	9.10 x 10 ⁻⁹
4657.9	19.817	2	8.10 x 10 ⁻⁹
4726.9	19.778	4	5.00 x 10 ⁻⁹
4735.9	19.276	4	5.80 x 10 ⁻⁹
4764.9	19.883	4	5.75 x 10 ⁻⁹
4806.0	19.238	6	7.90 x 10 ⁻⁹
4847.8	19.321	2	8.50 x 10 ⁻⁹
4879.9	19.696	6	7.80 x 10 ⁻⁹

Table 4-4. Determination of the Excitation Temperature from a Group of Argon Ionic Lines.

Time Delay (µs)	Temperature(K)	%RSD
5	20111	25.2
10	27324	23.7
25	37499	26.0
50	39330	43.0
100	29119	24.5
250	28004	22.2

4. Time-resolved Electron Density of the Plasma

The time-resolved electron density of the laser plasma was determined by measuring the Stark broadening of three different species. The first measurements involved introducing helium gas into the plasma. The average full-width at half maximum (FWHM) for the helium(I) 5875 Å line was $11.0 \text{ Å} \pm 0.5 \text{ Å}$. The FWHM was independent of time delay. Thus, a constant electron density was observed over the time duration studied. The calculated electron density was $5.9 \times 10^{17} \text{ cm}^{-3} \pm 15\%$. The main source of error in this determination was the fact that the plasma characteristics were altered by having to introduce sufficient helium to detect atomic emission. As the helium concentration increased in the plasma, the background emission intensity decreased and shrinking of the plasma dimensions was observed. As the helium concentration was further increased, the plasma extinguished. This

error results from the higher ionization energy of helium (23 eV) as compared to argon (15.8 eV). This method was not further pursued.

To solve this problem, hydrogen gas was introduced to determine the electron density. Only the time-resolved emission line widths for the H_{α} line were measured since the other two predominant emission lines (H_{β} and H_{γ}) were not spectrally resolved from the background argon ionic emission. Data obtained for the FWHM of the H_{α} line are presented in Table 4-5.

Table 4-5. Line Widths used for Calculating Electron Density.

Time Delay (µs)	FWHM (Å) ± 0.5 Å	
10	24.7	
25	27.6	
50	26.6	
100	26.9	
250	26.2	
average	26.4	

The average FWHM for the H_{α} line was 26.4 Å. This represents an electron density of 3.8 x 10^{17} cm⁻³ ± 10%. This error is mainly due to the uncertainty in the Stark broadening coefficient and not the actual measurement itself. This value is numerically close to the value determined using helium. Again, over the time duration studied, the

electron density does not seem to change. Small changes in electron density alter the line width of hydrogen significantly. Hydrogen has the largest sensitivity to Stark broadening. The amount of hydrogen required to detect atomic emission altered the plasma characteristics as in the helium case, but not to the same degree. As the hydrogen gas concentration was increased in the plasma, background intensity decreased, but the plasma never extinguished. This is because the ionization energy (IE) for hydrogen (IE = 13.6 eV) is lower than for argon (IE = 15.8 eV). It is well-known that the introduction of any species into a source alters the characteristics of the source. The object is to alter its characteristics to a minimum in order to make a determination. These two determinations represent an estimation of the electron density in the laser plasma.

The last method for determining the electron density involved using argon background emission itself. This ultimately reduces any changes in the plasma characteristics. The disadvantage of this method is that argon is not as sensitive to changes in the electron density. The 4806 Å argon ion line used for the determination was well-resolved and had the greatest sensitivity to changes in electron density. Table 4-6 shows the time-resolved FWHM for the 4806 Å line.

Table 4-6. FWHM for the 4806 Å argon ion line.

Time Delay (µs)	FWHM (Å) ± 0.5 Å
5	4.9
25	4.5
50	4.6
100	4.4
average	4.7

The average FWHM for the argon ion line was 4.7 Å. The calculated electron density is 7.3×10^{18} cm⁻³ $\pm 20\%$. This value is about 10 times higher than the values determined from both the introduction of the hydrogen and helium. This is due to the change in plasma characteristics from the introduction of a foreign species in order to determine the electron density. Again, no change in line width for argon was observed which indicates that the electron density remains constant over the time duration studied. Because the measurements with argon involve the least perturbation of the plasma, the value obtained here is considered more accurate than those obtained from He and H₂.

5. Time-resolved Ionization Temperatures of the Plasma

Using the time-resolved electron density measurements, the ionization temperature was determined using the Saha Equation. The

recursive solutions to Equations 4.4 and 4.5 were performed using Excel 4.0 (Microsoft Corporation, Redmond, WA). Table 4-7 presents the time-resolved ionization temperature of the laser plasma.

Table 4-7. Time-resolved Ionization Temperature of the Laser Plasma.

Time Delay (µs)	Ionization Temperature (K)	
10	19600	
25	18600	
50	17800	
100	17800	
250	17800	

Because no detectable change in electron density was observed, the ionization temperature remained constant. After considering the uncertainty in transition probabilities (±25%) for the argon lines used for the calculation, the observed change in ionization temperature with time is insignificant.

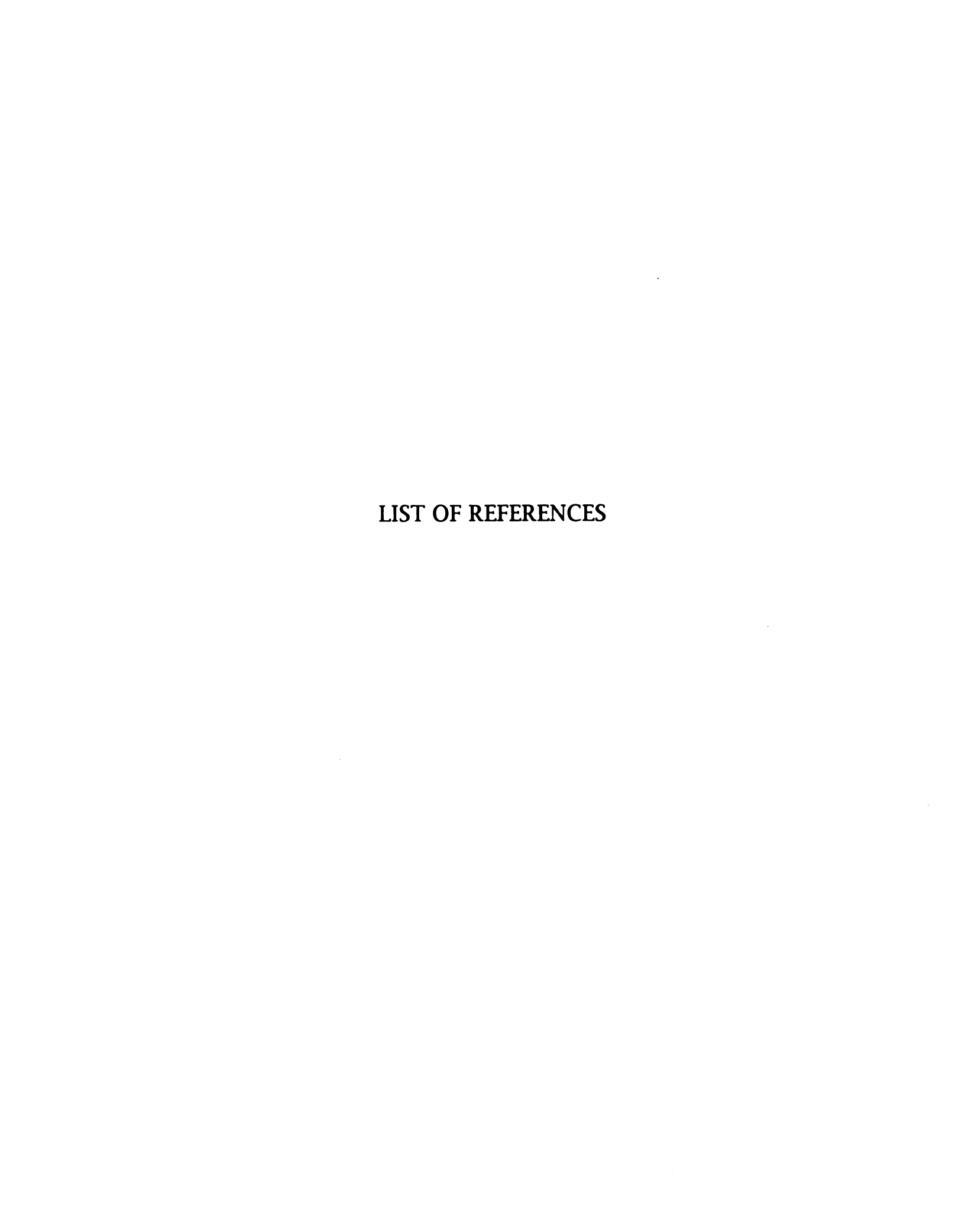
6. Conclusions

Based on the measurements of excitation and ionization temperature, local thermodynamic equilibrium (LTE) does not exist at any time during the plasma lifetime. In order for LTE to exist, it is a

necessary condition for the electron, gas, excitation, and ionization temperatures to become numerically equal.

It is advantageous to use a non-LTE plasma for atomic emission spectrometry. Work by Falk (6) with low pressure plasmas has shown that non-LTE plasmas have significantly lower background emission intensity than LTE plasmas. In emission spectrometry it is the background that determines the ultimate detection limit. However, it is a disadvantage to have a plasma with a high electron density. As the ionization equilibrium increases, the background intensity increases quadratically (7).

The laser plasma has very high excitation and ionization efficiencies that are important for dissociating any molecular species that form during the atomization cycle of the CRA. It is also important for excitation of metals and non-metals possessing high ionization energys. Even though the laser plasma has a high background emission early after plasma formation, time discrimination using the boxcar averager can enhance the signal-to-background ratio significantly.



LIST OF REFERENCES

- 1. Boumans, P. W. J. M, Theory of Spectrochemical Excitation, Plenum Press, New York, 1966
- 2. Cremers, D. A. and Radziemski, L. J., Anal. Chem., 55, 1252 (1983)
- 3. Ingle, J. and Crouch, S., Spectrochemical Analysis, Prentice Hall, Englewood Cliffs, NJ, 1987
- 4. Griem, H., Plasma Spectroscopy, Mc-Graw Hill, NY, 1964
- 5. Winge, R., Fassel, V., Peterson, V., Floyd, M., Inductively Coupled Plasma-Atomic Emission Spectroscopy, Elsevier, New York, 1985
- 6. Falk, H., Hoffmann, E., Ludke, Ch., Spectrochim. Acta, 39B, 283 (1984)
- 6. Falk, H., Spectrochim. Acta, 32B, 437 (1977)

CHAPTER 5

INFLUENCE OF EXPERIMENTAL PARAMETERS ON THE CHANGE IN PLASMA CHARACTERISTICS

A. Introduction

In the following sections of this chapter the changes in plasma characteristics due to the atomization cycle of the CRA are discussed. From initial experiments, it was discovered that three experimental parameters have the greatest influence in the change in characteristics that occur during the atomization cycle of the CRA: (1) the laser power used for the formation of the plasma, (2) atomization temperature, and (3) flow rate of the argon. The results of the initial experiments are presented in the first section.

From the preliminary results, a two-level factorially designed experiment was performed. A factorially designed experiment isolates the effects that every variable has on a response function (1). This experiment determines the influence and magnitude of the changes that occur in the plasma with respect to the three parameters above. The results of the experiment are discussed in the next section. The implications of the conclusions are discussed in the last section.

The experimental setup was previously described in chapter 3. For all experiments the plasma was formed 6 mm above the carbon rod surface. Normally, electrothermal atomizers use a three stage heating process. First, the desolvation cycle removes the solvent. Next, the charring, or ashing cycle, is used to remove volatile organics that may interfere with the analytical determination from the matrix. Finally, the

atomization cycle atomizes the analyte. For all the experiments described in this chapter only the atomization cycle was used. In addition, no sample was placed on the carbon rod for all experiments described.

B. Preliminary Experiments

1. Determination of the Change in Electron Density in the Plasma

Two physical changes of the plasma occur due to the atomization cycle of the CRA. The electron density and background decrease; however, the ionization temperature of the plasma throughout the atomization cycle remains nearly constant (see next section). In order to calculate the ionization temperature of the plasma, the electron density must be determined. This is typically done by measuring the linewidths of either hydrogen or helium emission lines in which the linear Stark effect is the dominant cause of broadening (see Chapter 4). The experimentally determined linewidths are compared to tabulated profiles (2). Because the hydrogen or helium concentration required to make a determination changed the characteristics of the plasma significantly, this method was not used. Instead, the linewidth of the 4806 Å argon ion line was measured. This method is not as sensitive to changes in electron density because the dominant cause of broadening for argon is the quadratic Stark effect. The 4806 Å ion line is wellresolved and has a high signal-to-background ratio at all time delays. Figure 5-1 shows the typical decrease in linewidth of the argon ion line caused by the atomization cycle. The data in Figure 5-1 were collected 5 us after plasma formation with an atomization temperature of 3000°C.

The monochromator entrance slit was set at 30 μ m (bandpass = 0.6 Å). The argon flow rate was 1.1 liters/minute. The calculated full-width at half maximum (FWHM) values for the argon ion line before and during the atomization cycle were 4.9 Å and 3.2 Å, respectively.

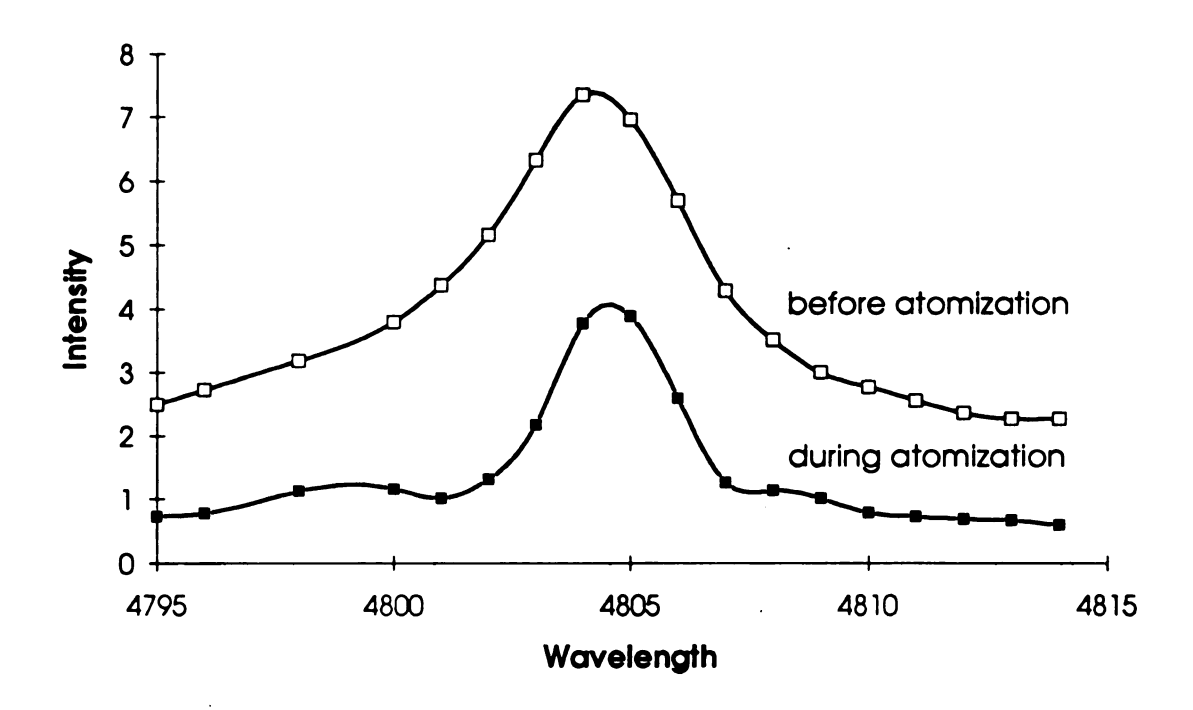


Figure 5-1. Argon Ion Linewidth Before and During Atomization Cycle

The calculated time-resolved electron densities based on the FWHM values before and during the atomization cycle (3000°C) are summarized in Table 5-1. On average, over the 100 µs time interval monitored, there was a 30% decreasein electron density. The change in electron density occurs early after plasma formation and decreases as the plasma decays. The largest change occurs 5 µs after plasma formation.

Table 5-1. Electron Densities ($\pm 20\%$) of Argon Plasma Before and During Atomization Cycle (all FWHM are ± 0.5 Å)

Time Delay (μs)	FWHM (Å) Before	Calculated Density (cm ⁻³)	FWHM (Å) During	Calculated Density (cm ⁻³)	% Change
5	4.9	8 X 10 ¹⁸	3.2	5 X 10 ¹⁸	-40
25	4.5	7 X 10 ¹⁸	3.4	5 X 10 ¹⁸	-30
50	4.6	7 X 10 ¹⁸	3.5	5 X 10 ¹⁸	-30
100	4.4	7 X 10 ¹⁸	3.5	5 X 10 ¹⁸	-30

2. Determination of the Change in Ionization Temperature of the Plasma

The ionization temperatures of the plasma were determined before and during the atomization cycle. Ionization temperatures were calculated (refer to Chapter 4) using the Saha equation (3). Relative ion-to-atom intensity ratios of the 4348 Å ion and the 4158 Å atom lines were used because they provide intense spectrally-resolved emission lines at all time delays. Figure 5-2 shows the time-resolved ionization temperatures before and during the atomization cycle. The average calculated ionization temperature was 21000 K. Only a small increase in the ionization temperature was observed by heating the carbon rod to the atomization temperature. The greatest change, 2%, was observed 5 us after plasma formation. At later times, the ionization temperature remained essentially constant. Due to the uncertainty in transition

probabilities ($\pm 25\%$) for the 4348 and 4158 Å argon lines, the change in ionization temperature was deemed insignificant.

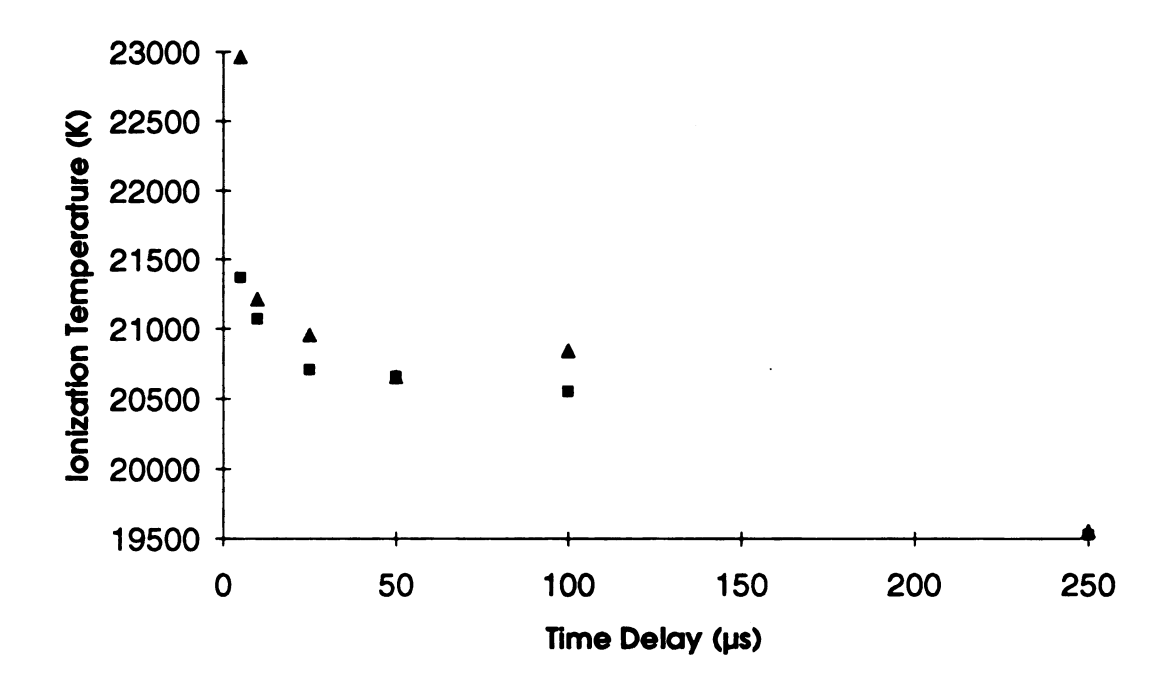


Figure 5-2. Ionization Temperature Change Before (■) and During (s) the Atomization Cycle

3. Determination of the Change in Background Emission from the Plasma

A large suppression of the background continuum also is observed during the atomization cycle. Suppression of the background is dependent on the atomization temperature, the height that the plasma is formed above the carbon rod, the laser power, and the argon flow rate. As illustrated in Figure 5-3, the background intensity decreases throughout the atomization cycle and then returns to the original intensity after the atomization cycle is completed. The background

emission was collected at the 3933 Å calcium ionic emission line, but is representative of the reduction of the continuum emission. If the laser power is not above a certain threshold, the plasma extinguishes during the atomization cycle. In addition, the brass stand (CRA) temperature increases after each use which decreased the background emission before the atomization cycle. After approximately ten repetitive cycles, the background emission equilibrates to a steady state value.

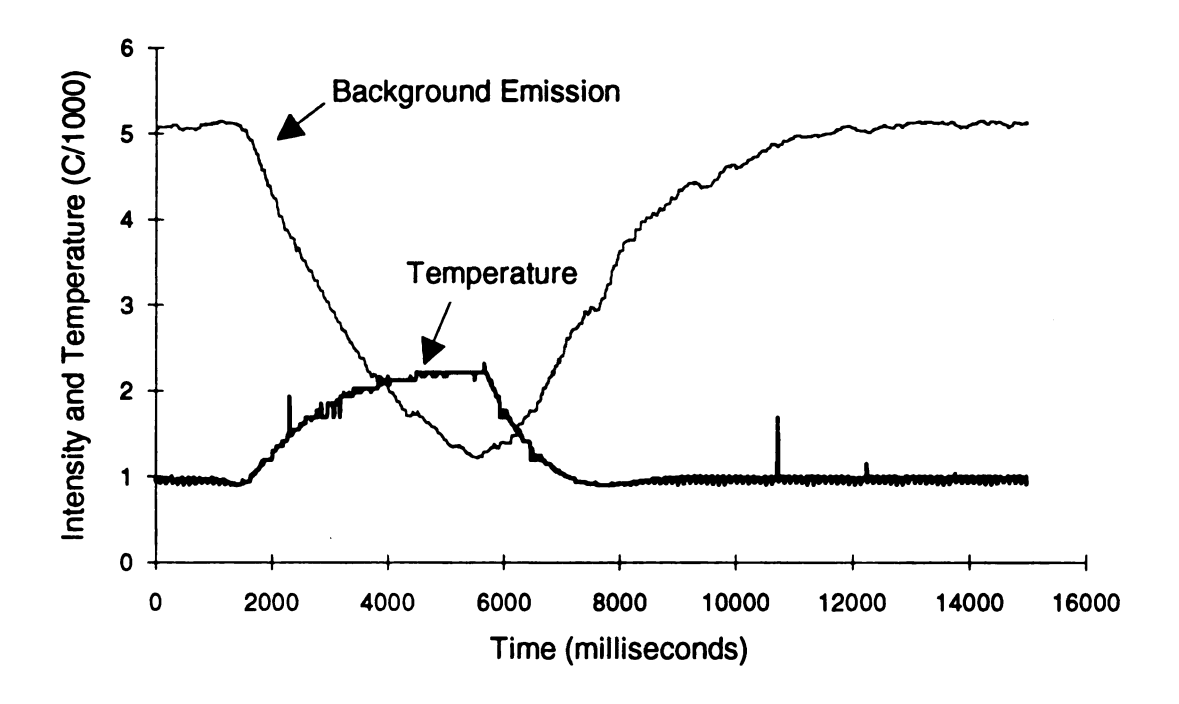


Figure 5-3. Suppression of Continuum Background Emission

The suppression in the background continuum emission occurs because the change in the density of argon caused by the heating of the gas in the atomization cycle. As a result, there are less argon atoms at the focal point of the laser. As the number density decreases, the

breakdown threshold of argon increases. Thus, the fraction of laser power required to breakdown argon increases and less energy is used for growth of the plasma which decreases the background continuum emission.

4. Determining the Change in Excitation Conditions in the Plasma

The ion-to-atom ratio for a given species is strongly influenced by the excitation conditions that exist in the plasma (3). To quantify the magnitude of the change in plasma conditions, this ratio was compared before and during the atomization cycle. The ratio of the ion-to-atom ratios was computed using the following formula:

$$R = \frac{(\frac{I_{\text{ion}}}{I_{\text{atom}}})_{\text{during}}}{(\frac{I_{\text{ion}}}{I_{\text{atom}}})_{\text{before}}} \times 100\%$$

An increase in R indicates enhanced excitation conditions in the plasma during the atomization cycle as compared to conditions before the atomization cycle. This ratio was calculated based on the maximum change in intensity that occured during the atomization cycle. Figure 5-4 shows the enhancement of the argon ion-to-atom line ratio during the atomization cycle. These results were obtained 5 µs after plasma formation with a laser power of 4.5 MW/pulse, argon flow rate of 1.5 liters/minute, and an atomization temperature of 2900°C.

An enhancement of 175% was observed under these conditions. There is also a time lag between the maximum atomization temperature and the maximum change in excitation conditions in the plasma. This is

due to the finite time it takes to heat the argon. The time lag is dependent on the specific heat and thermal conductivity of the inert gas used. Further results about the change in excitation conditions are presented in the next section. Figure 5-4 is representative of the results obtained.

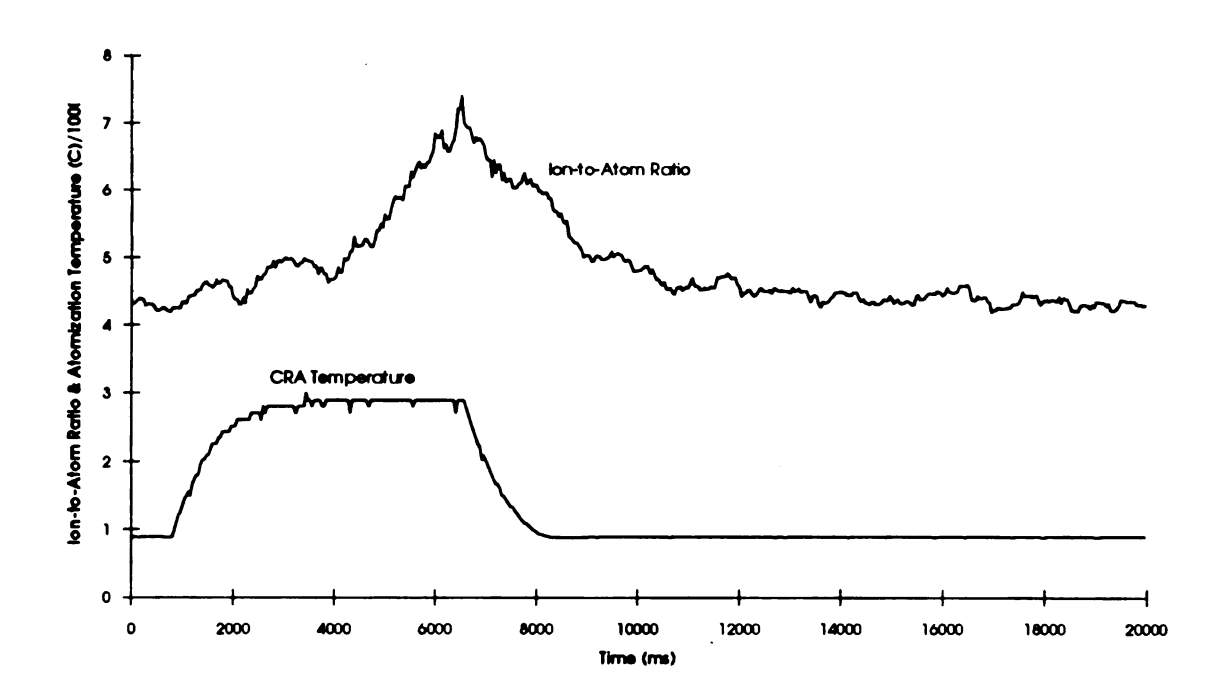


Figure 5-4. Change in the Argon Ion-to-Atom Ratio.

C. Results of the Factorially Designed Experiment

1. Initial Conditions of the Experiment

The preliminary results above indicate the plasma characteristics (electron density and background emission) are altered due to the changes in the surrounding atmosphere in which the plasma is formed. These changes are caused by heating the CRA to the atomization

temperature. A two-level factorially designed experiment was used to determine the significance of the atomization temperature, laser power, and the argon flow rate on the argon ion-to-atom intensity ratio. The two levels used for the experiment are presented in Table 5-2.

The LO flowrate is the minimum value that is necessary to transport the atomic vapor to the plasma. The HI flowrate is the boundary condition where results were not reproducible due to insufficient sampling of the atomic vapor by the 10 Hz repetition rate of the laser.

The LO atomization temperature was based on previous experiments that showed the plasma is more stable at atomization temperatures below 2000°C. The HI atomization temperature setting was the maximum temperature that did not produce visible soot from the rod.

The laser power settings were selected based on the above HI and LO conditions. At lower power settings, the plasma was very unstable and formation of the plasma was not observed with every laser pulse. When the atomizer was heated to the atomization temperature the plasma did not form at lower laser power. The LO setting represents the lowest power setting necessary to form the plasma under all the conditions listed in Table 5-2. The HI setting was the maximum power that did not damage the mirrors used in the experimental setup. All gas temperatures were measured by a Type K thermocouple (Omega, Stamford, CT) referenced to an ice-water bath (0°C). To give the fastest response time, the thermocouple was made as small as possible and used without a shield.

Table 5-2. Experimental Conditions for the Factorially Designed Experiment

Condition	LO Setting	HI Setting
Flow Rate	0.6 l/min Ar	1.5 l/min Ar
Atomization Temperature	2460°C	2950°C
Laser Power	9.0 MW/pulse	10.0 MW/pulse

The results presented in Figure 5-5 are the percent change in ion-to-atom ratio for the Ar(II) 4348 Å ion line and the Ar(I) 4158 Å under the eight different experiment treatments. The percent change was calculated using the following formula:

$$\%\text{change} = \frac{\left(\frac{I_{\text{ion}}}{I_{\text{atom}}}\right)_{\text{during}} - \left(\frac{I_{\text{ion}}}{I_{\text{atom}}}\right)_{\text{before}}}{\left(\frac{I_{\text{ion}}}{I_{\text{atom}}}\right)_{\text{before}}} \times 100\%$$

In all treatments, an increase in the ratio indicates that plasma excitation conditions are enhanced by heating the CRA to the atomization temperature.

2. ANOVA Results

Several trends are observed based on the results. First, using Analysis of Variance (ANOVA) (1), the percent changes in the ion-to-atom ratio are significant with respect to both delay time and the different

treatments of the experiment. Table 5-3 shows the ANOVA table calculated by Excel version 4.0 (Microsoft Corporation, Redmond, WA). The calculated F-values are larger than the critical F-values for all treatments of the experiment. The P-value represents the probability that $F_{\text{calculated}}$ is actually less than F_{critical} . Since the P-values are very small, the time delay and treatments for the experiment influence the change in characteristics of the plasma.

Table 5-3. ANOVA Table for the Factorially Designed Experiment

Source of Variation	F _{calculated}	F _{critical}	P-value
Time Delay	8.65	2.49	5.24 x 10 ⁻⁵
Treatments	4.27	3.07	1.67 x 10 ⁻²

Second, the enhancement in excitation conditions in the plasma is more pronounced at early time delays. This suggests that the actual formation of the plasma is affected. Tukey's statistical procedure (1) was used to identify significant differences between levels of the eight factors. Differences greater than 7.7 between two treatments indicate that the ion-to-atom ratio is affected significantly. The results of the factorially designed experiment are shown in Figure 5-5. In the abscissa legend, F = flowrate, T = atomization temperature, P = laser power, and the appended letter indicates h = high level or <math>l = low level for each experimental parameter. Finally, this figure shows the smallest change

in plasma excitations occurs when using a HI flowrate, a LO atomization temperature, and a HI laser power for all time delays.

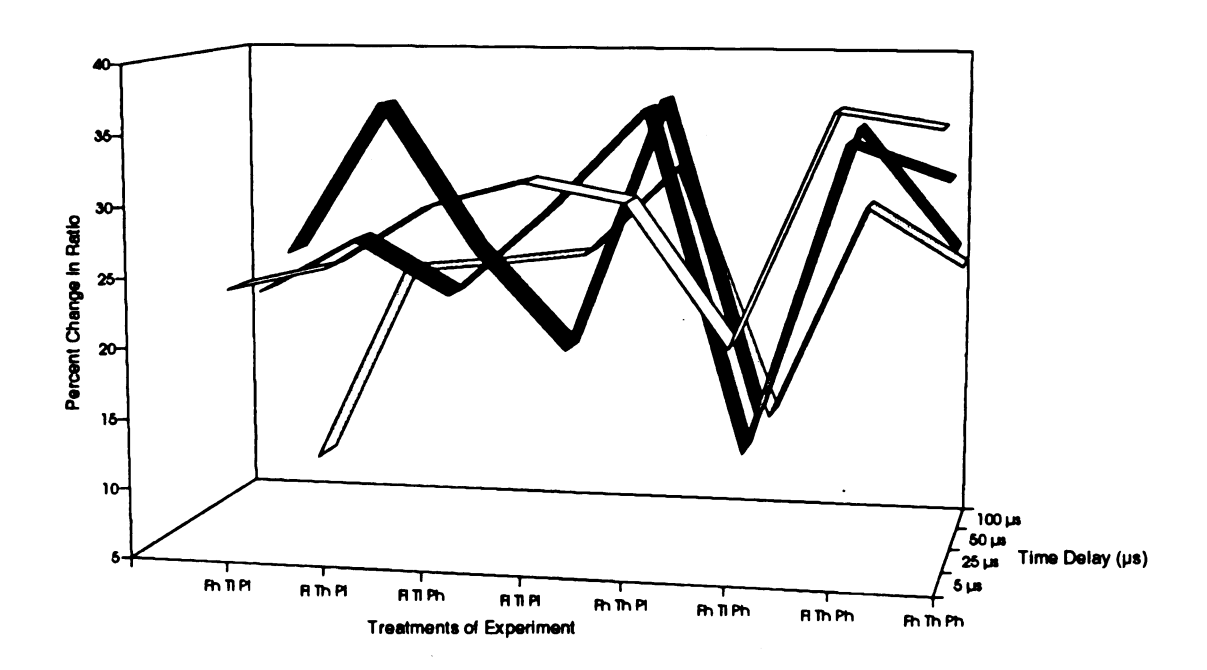


Figure 5-5. Results of the Factorially Designed Experiment.

3. Dependence of Argon Gas Temperature on Breakdown Threshold

Based on the results described above, formation of the plasma is seen to be dependent on the surrrounding conditions. As the atomization temperature is increased for a given set of conditions, the gas temperature in which the plasma forms is raised. Two reasons to expect this correlation may be suggested by comparing the breakdown thresholds at different argon gas temperatures. Gas temperatures were measured at the exact location where the plasma was formed above the carbon rod. The breakdown threshold is defined as the minimum laser

power necessary to form a plasma 90 percent of the time. Results are shown in Figure 5-6. The maximum gas temperature was 405°C, which corresponds to a maximum atomization temperature of 3044°C. The argon flow rate was 0.6 liters/minute. The breakdown threshold is linearly correlated with the argon gas temperature. Thus, when higher atomization temperatures are required, laser power for plasma formation is also increased. As shown in the previous section, a higher laser power was required also to maintain the excitation conditions in the plasma.

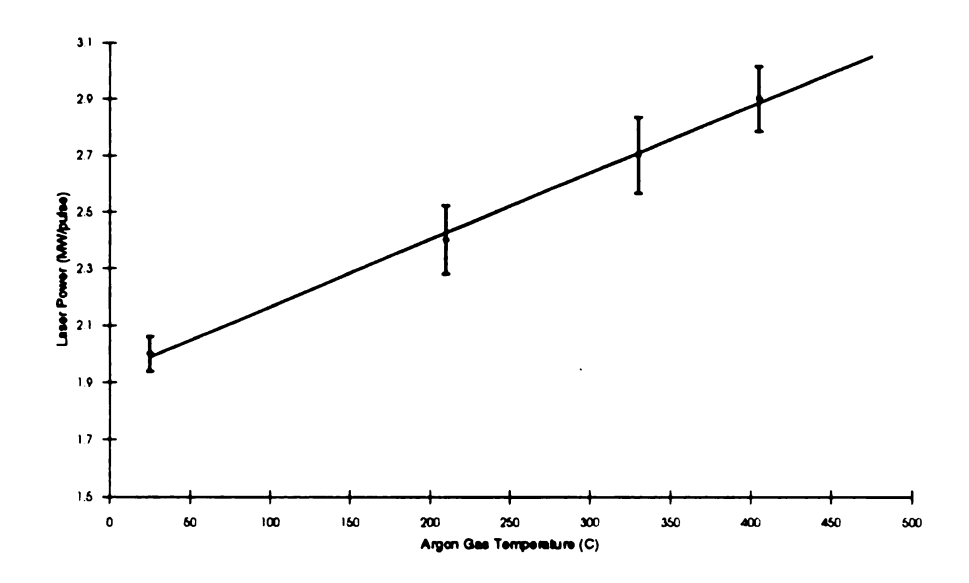


Figure 5-6. Effect of Breakdown Threshold on Gas Temperature

4. Argon Gas Temperature Dependence on Experimental Parameters

The argon gas temperature is dependent on the atomization temperature, flow rate, and height above the carbon rod. Figure 5-7 shows the effect of atomization temperature and argon gas flow on the

maximum argon gas temperature during the atomization cycle. The CRA was heated 3000°C and a thermocouple positioned 5 mm above the carbon rod measured the gas temperature. The computed equation for the regression line is Temperature = 3.51*flowrate(liters/minute) + 568.1 ($r^2 = 0.51$). Applying the t-test at the 95% confidence interval, the slope of the line is statistically zero. This indicates that the maximum argon gas temperature is independent of the argon flow rate. This independence is due to the high specific heat and thermal conductivity of argon.

Figure 5-8 shows the maximum argon gas temperature at different heights above the carbon rod during the atomization cycle. There is an inverse linear correlation between the height above the carbon rod and the maximum gas temperature. The flow rate was 1.5 liters/minute and the atomization temperature was 3000°C. As the atomization temperature increases, the maximum gas temperature becomes more sensitive to the height above the carbon rod. Table 5-4 shows the relationship between the atomization temperature and the slope of the line.

Under the experimental conditions used, the laser plasma is sustained by the avalanche mechanism (see Chapter 2). Two kinetic effects change due to the atomization cycle. First, as the argon gas density decreases during the atomization cycle, the plasma expands. This increases the probability that an electron will diffuse out of the focal volume of the electric field and undergo ion-electron recombination. Second, the increase in the mean free path reduces the frequency of electron-atom and electron-ion collisions that sustain the

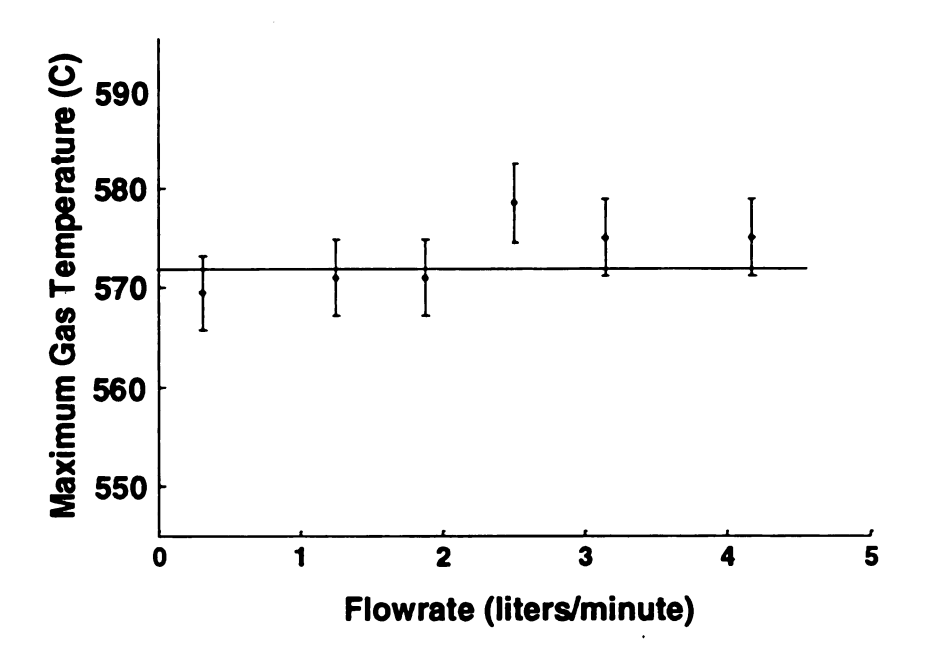


Figure 5-7. Effect of Argon Flow Rate on Maximum Gas Temperature

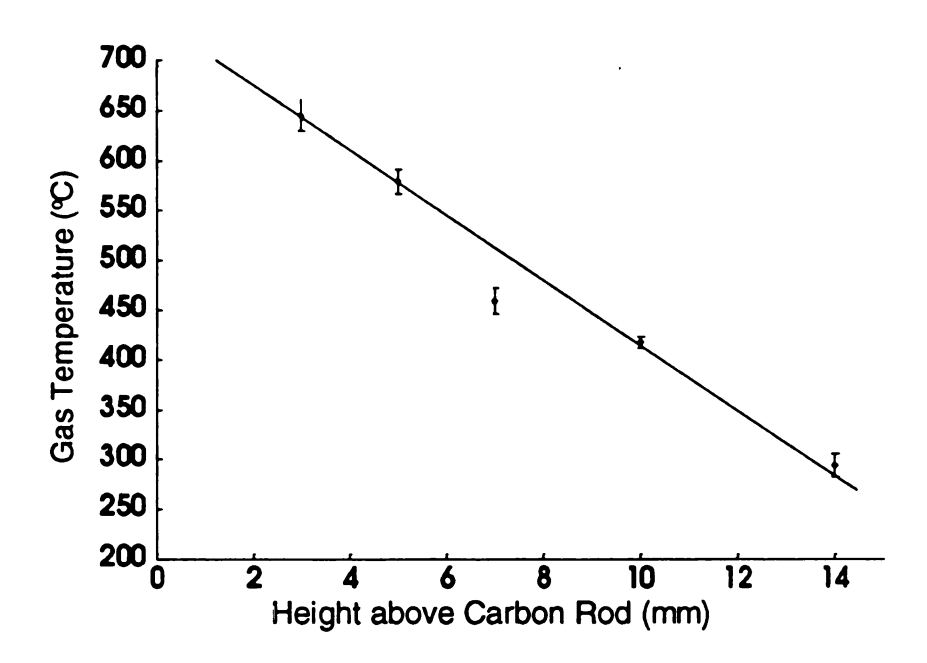


Figure 5-8. Effect of Height above the Carbon Rod on the Maximum Gas Temperature.

avalanche mechanism. The electrons cannot gain translational energy to sustain the plasma without collisions. The frequency of collisions along with the diffusion of electrons from the focal region determine whether the plasma will form, assuming that all other kinetic losses of free electrons remain constant. The end result is a less dense plasma, or no plasma at all.

Table 5-4. Effect of Atomization Temperature on Slope

Atomization Temperature (°C)	Slope (°C/mm)
2880	-27.3
3000	-31.3
3130	-50.6

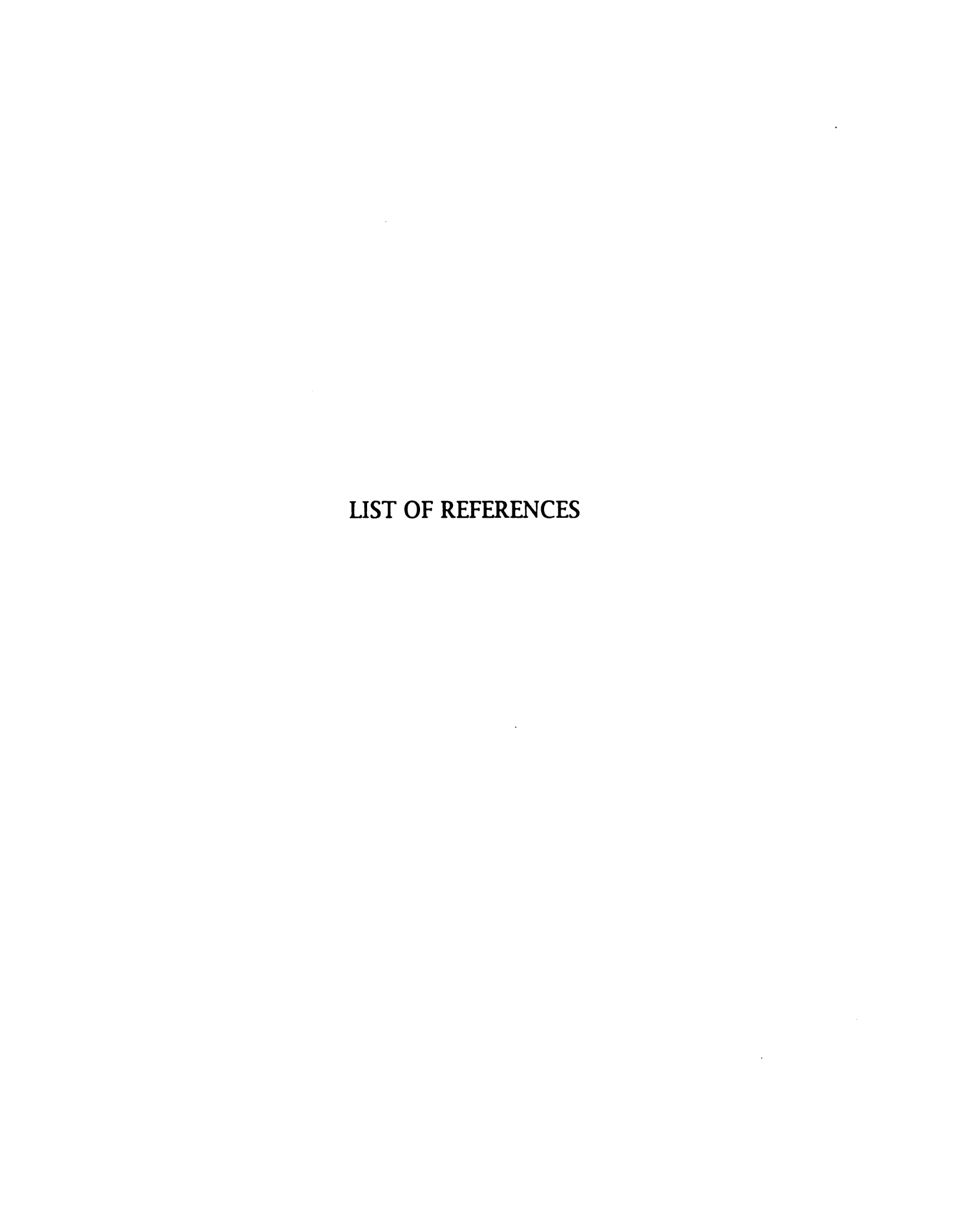
C. Conclusions

The laser power is an important parameter in determining the excitation conditions in the plasma. As discussed in chapter 6, analytical determinations require the laser power to be in the range from 3 to 5 MW/pulse, which is considerably less than that used in the factorial experiment above. At high laser powers (>5 MW/pulse), ionic emission from singly charged ions is not observed due to ionization of the analyte into higher ionization states. At low laser power (2-3 MW/pulse), the plasma becomes unstable and eventually is extinguished during the atomization cycle. This problem is more prominent when atomization

temperatures above 2000°C are employed. Higher flow rates cannot be used to compensate for determinations requiring higher atomization temperatures. The flowrate must be adjusted to be above the minimum required for reproducible transport of the atomic vapor to the plasma, yet below the maximum flowrate where the transport becomes erratic.

The conditions for an analytical determination must be chosen such that the conditions of the plasma are reproducible. This implies the use of the lowest possible atomization temperature which does not degrade the determination. This is because of the large dependence of atomization temperature on the change gas temperature. Since there is a substantial decrease in the maximum argon gas temperature at higher heights above the carbon rod, the CRA was modified so that the plasma is formed at 10 mm, instead of 6 mm, above the carbon rod.

As with laser microprobe analysis, the emission characteristics of the laser plasma are strongly influenced by the surrounding atmosphere (4). From this study it is concluded that careful selection of argon flow rate, atomization temperature, and laser power for a particular determination are necessary.



LIST OF REFERENCES

- 1. Devore, J. L., *Probability and Statistics for Engineering and the Sciences*, (Brooks/Cole Publishing Company, Belmont, CA, 1987), 2nd ed, p. 379.
- 2. Griem, H. R., *Plasma Spectroscopy*, (McGraw-Hill, New York, 1964), chapter 13.
- 3. Boumans, P. W. J. M., *Spectrochemical Excitation*, (Hilger & Watts Ltd., London, 1966), p. 171.
- 4. Iida, Y., Appl. Spec., 43, 229 (1989).

CHAPTER 6

ANALYTICAL STUDIES USING CRALIBS

A. Introduction

In chapter 4 the characteristics of the plasma were presented. These characteristics make the plasma especially attractive for determining elements of any excitation energy. In chapter 5 an investigation of the influence of experimental parameters on the plasma was presented. The effects of laser power, atomization temperature, and argon flow rate have been found to play an intricate role in the stability of the laser plasma, especially during the atomizaton cycle.

This chapter presents analytical data for the detection of alkali, alkaline earth, and transition metal elements. Data are collected by delaying the emission measurement until the background continuum emission decreases, and peak analyte emission occurs. Subsequent sections of this chapter investigate: (1), the importance of the desolvation stage; (2), the control of excitation conditions in the plasma; (3), the effect of plasma conditions on the analytical signal; (4), optimization of experimental conditions; (5), dissociation of molecular species vaporized from the CRA; and (6), the experimental results which led to the development of the glass chimney discussed in Chapter 3. In addition, detection limits are reported for the group of representative elements investigated in this dissertation. Finally, the results from the determination of Fe and P in a coal fly ash sample are presented. Experimental conditions are reported when they differ from the general conditions discussed in Section C of Chapter 3 (page 38).

The data presented in this chapter are a compilation of experiments performed at different times. Many supplemental studies were done during the investigation of a particular element. The results and trends reported are consistent under all experimental conditions. The integration time and time constant on the boxcar for all experiments presented was 0.5 µs and 0.1 ms, respectively.

B. Detection of Analyte Species in the Laser Plasma

Due to the high excitation and ionization temperatures (see Chapter 4) of the laser plasma, the emission of analyte species in the plasma orginate from singly charged cations such as Fe⁺, Ca⁺, and Mg⁺. This makes selection of the best analyte emission line difficult. The CRC Handbook of Chemistry and Physics (1) contains emission lines and relative intensities for all the elements collected using arc and spark excitation sources. A more valuable reference for the selection of analysis wavelengths is by Winge and co-workers (2). This book tabulates the intensity of emission lines for elements that are determined Inductively Coupled Plasma-Atomic by **Emission** Spectrometry (ICP-AES). It also tabulates spectral interferences that could arise during a determination. Since the ICP characteristics approximate the laser plasma, emission line intensities for both Unless stated otherwise, all emission techniques are similar. wavelengths were selected using this reference.

Figure 6-1 shows the emission from 5 μ L of a 75.7 ppm (378.5 ng) aqueous chromium solution. The emission at the 2677.2 Å Cr(II) line was collected after a 25 μ s time delay. The time axis is relative to the start

of the atomization cycle. The time lag in the appearance of the signal is due to the finite heating rate (800°C/s) of the CRA. Background emission was subtracted using the appropriate blank. Figure 6-1 is representative of the data collected for each element studied. The full width of the chromium ionic emission peak is approximately 4 seconds. These peak widths allow approximately 40 samplings of the analyte vapor by the laser plasma which is sufficient to define the peak without distortion (3). In general, peak widths for different elements vary from 2 to 4 seconds depending on volatility.

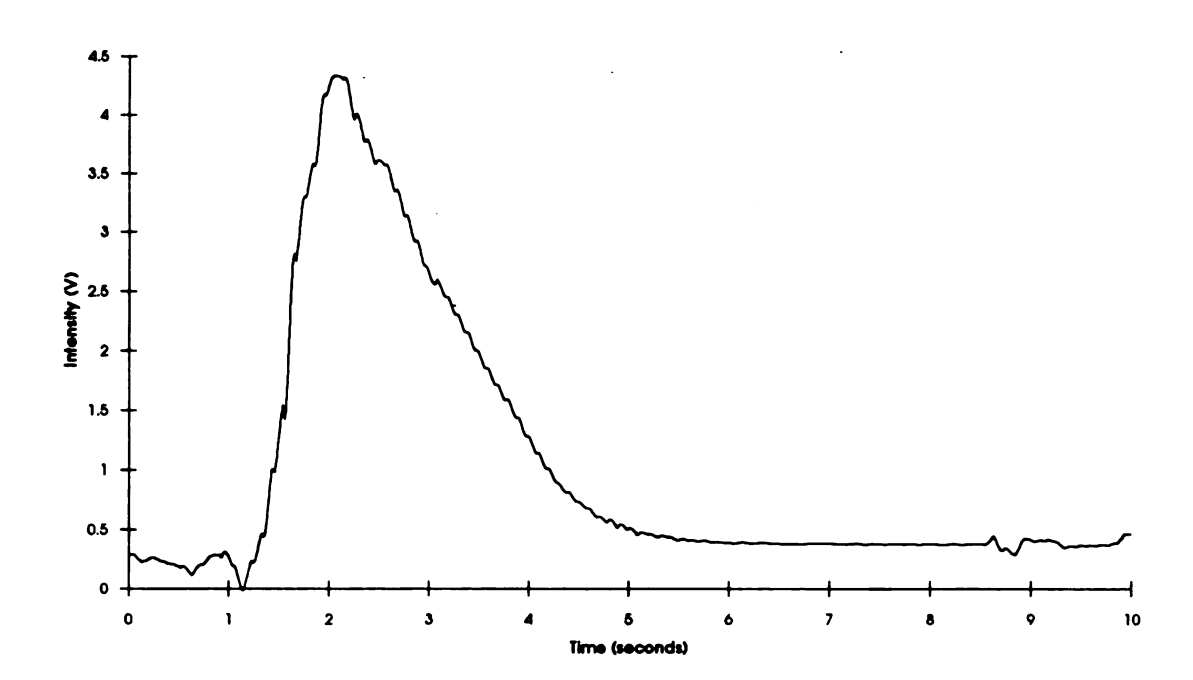


Figure 6-1. Chromium Ionic Emission in the Laser Plasma. 2677.2 Å Cr(II), 25 µs time delay, 3.6 MW/pulse laser power, and 2700°C atomization temperature.

C. Experimental Importance of the Desolvation Stage

The desolvation cycle in electrothermal atomization is used to vaporize the solvent. This cycle can last as long as sixty seconds and the temperature is typically adjusted to below the boiling point of the solvent to prevent loss of sample due to sputtering. The utility of the desolvation cycle for this technique was determined by placing different volumes of a 20 ppm sodium aqueous sample on the carbon rod atomizer (CRA) with and without using desolvation cycle. The maximum volume that fills the notch on the carbon rod is approximately 10 µL. Above this volume, the sample droplet easily falls off the carbon rod. Sodium atomic emission at 5890 Å was collected 25 µs after plasma formation.

A twenty second desolvation cycle was used. The desolvation temperature was not directly determined. The temperature must be determined indirectly because the PIN photodiode used to detect the blackbody radiation from the carbon rod is not sensitive to temperatures below 700°C. Instead, the temperature of the rod during the desolvation cycle was determined indirectly by measuring the the voltage drop across the CRA (see Chapter 3). The desolvation temperature was set at 100°C which corresponds to a 0.4 V drop across the CRA. When this setting is used, the CRA completely vaporizes the water in several seconds. This was confirmed visually and experimentally. As the solvent is vaporized, the background decreases because the energy of the plasma is used for dissociating, atomizing, and exciting the solvent. The suppression of the background lasts only several seconds; then it returns

to the previous intensity. The return of the background indicates the complete vaporization of the solvent. The length of the desolvation cycle was chosen so that the maximum volume of sample placed on the CRA would be vaporized completely before the atomization cycle begins. The desolvation time also allowed the plasma to restabilize before the atomization cycle occured so that each sample determination was reproducible.

Figure 6-2 shows the sodium atomic emission signal with increasing sample volume when the desolvation cycle is omitted. A linear signal ($y=1.07x-2.54 \times 10^{-16}$, $r^2=0.994$) is observed when sample volumes less than 2 µL are placed on the CRA. For volumes larger than 2 µL, the signal plateaus (y=0.174x+1.8, $r^2=0.978$), and becomes nearly independent of sample volume. The irreproducibility increases for larger sample volumes. These two effects are due to solvent plasma loading (4). As more solvent is vaporized, the energy of the plasma is used for excitation of the solvent. This reduces the amount of excitation the analyte receives in the plasma. Because the solvent and analyte are vaporized at the same time, the analyte emission becomes more irreproducible.

Figure 6-3 shows the effect of using the desolvation cycle. For sample volumes less than 2 μ L, the signal is proportional (y=0.839x - 0.17, r²=0.998) to the sample volume. For sample volumes of 2 μ L to 6 μ L, the signal is still proportional to the sample volume but has a lower sensitivity (y=0.347x + 0.772, r²=0.996). With higher sample volumes, the analyte signal becomes independent of the sample volume (y=-0.0085x + 3.02, r²=0.018). Thus three distinct regions are observed. At low sample

volumes, the generated aerosol does not perturb the plasma sufficiently to cool the plasma. All the energy is used to excite the analyte.

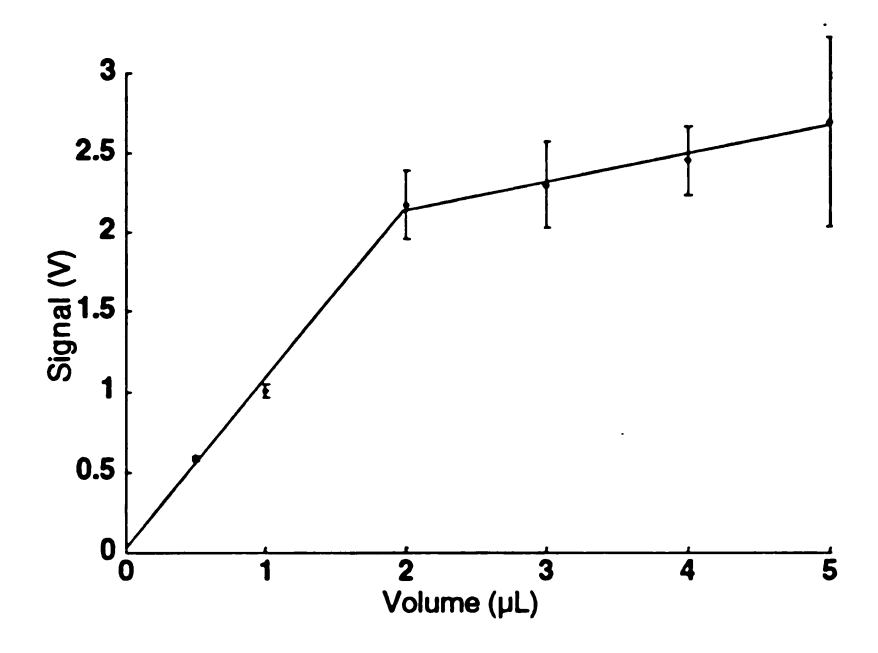


Figure 6-2. Effect of Omitting Desolvation Cycle. 5890 Å Na(I), 25 µs time delay, 3.0 MW/pulse laser power, and 2200°C atomization temperature.

At intermediate volumes, the plasma is slightly cooled by the aerosol which leads to a decrease in the response. At high sample volumes, the plasma is substantially cooled by the aerosol, and the signal becomes independent of the sample volume. By using the desolvation cycle, the amount of sample which can be analyzed is nearly doubled. The increase in desolvation prior to the atomization cycle allows larger sample volumes to be used before plasma solvent loading occurs. The reproducibility also remains approximately constant at all sample volumes when using the desolvation cycle.

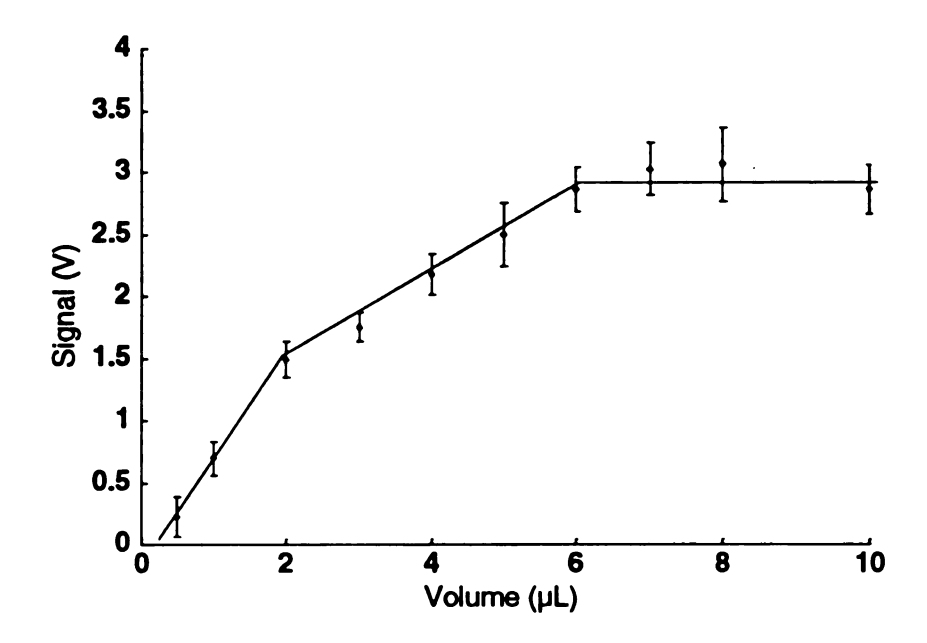


Figure 6-3. Effect of Using Desolvation Cycle. 5890 Å Na(I), 25 µs time delay, 20 sec desolvation cycle at 100°C, 3.0 MW/pulse laser power, and 2200°C atomization temperature.

D. Effect of Laser Power and Time Delay on Analytical Signal

As discussed in Chapter 5, the laser power determines the excitation conditions in the plasma. When laser powers above the breakdown threshold are used for formation of the plasma, the excitation conditions are enhanced with increasing laser power. Except for sodium, analytes which possess low and moderate ionization potentials (< 9 eV) are detected by emission from singly charged cations. Although sodium possesses a low ionization potential (IP = 5.14 eV) and is highly ionized in the plasma, the high oscillator strength of the $3S \rightarrow 3P$ transition for the 5890 Å neutral Na(I) emission line allows detection.

In general, as the laser power increases, the analyte is further ionized to a doubly charged cation and the emission from singly charged cations decreases. Figure 6-4 shows the effect of laser power on the intensity of the Na(I) emission at 5890 Å. As the laser power is increased, the peak signal intensity rapidly decreases and the peak emission occurs at later times. Atomic sodium is detected with laser powers as high as 6.75 MW/pulse.

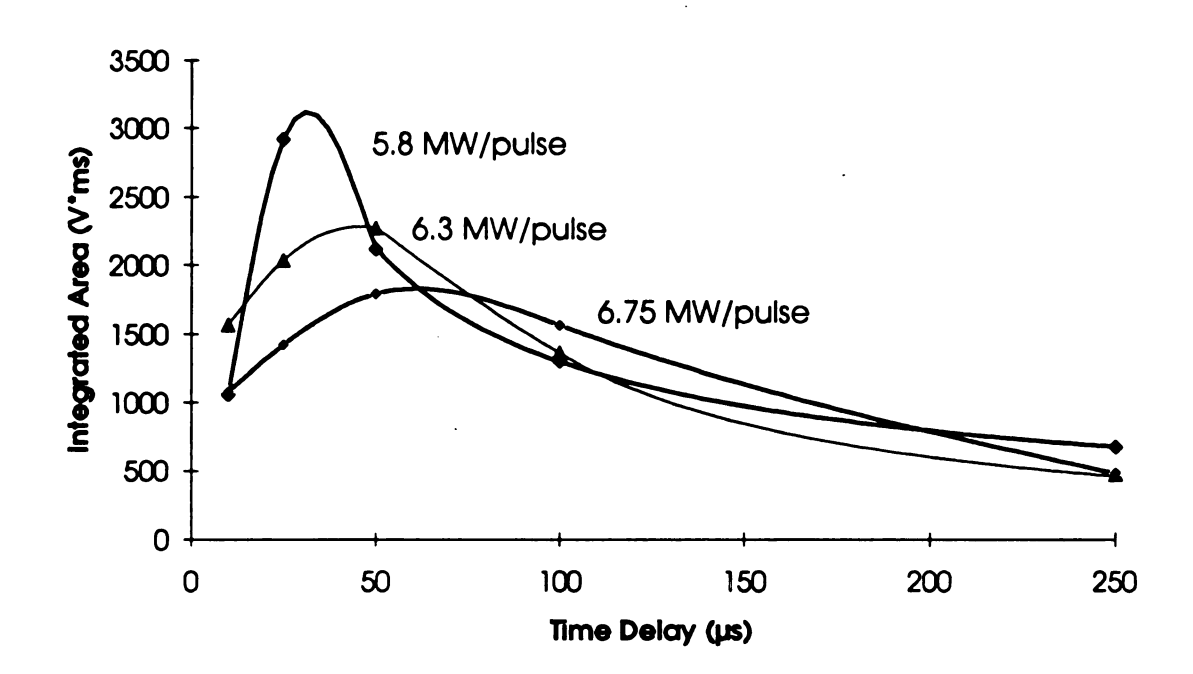


Figure 6-4. Effect of Laser Power on Sodium Atomic Emission. 5890 Å Na(I), and 2500°C atomization temperature.

Figure 6-5 shows the effect of laser power on peak emission for Mg(II). The intensity from magnesium ion emission is highly attenuated when using a laser power of 5.0 MW/pulse. At even higher laser power, no ionic emission is detected. This is because the plasma is ionizing Mg⁺

to Mg²⁺. Again, peak ionic emission shifts to later times with increasing laser power. Peak ionic emission from magnesium occurs approximately 40 µs and 65 µs after plasma formation when the laser power is 3.6 MW/pulse and 5.0 MW/pulse, respectively.

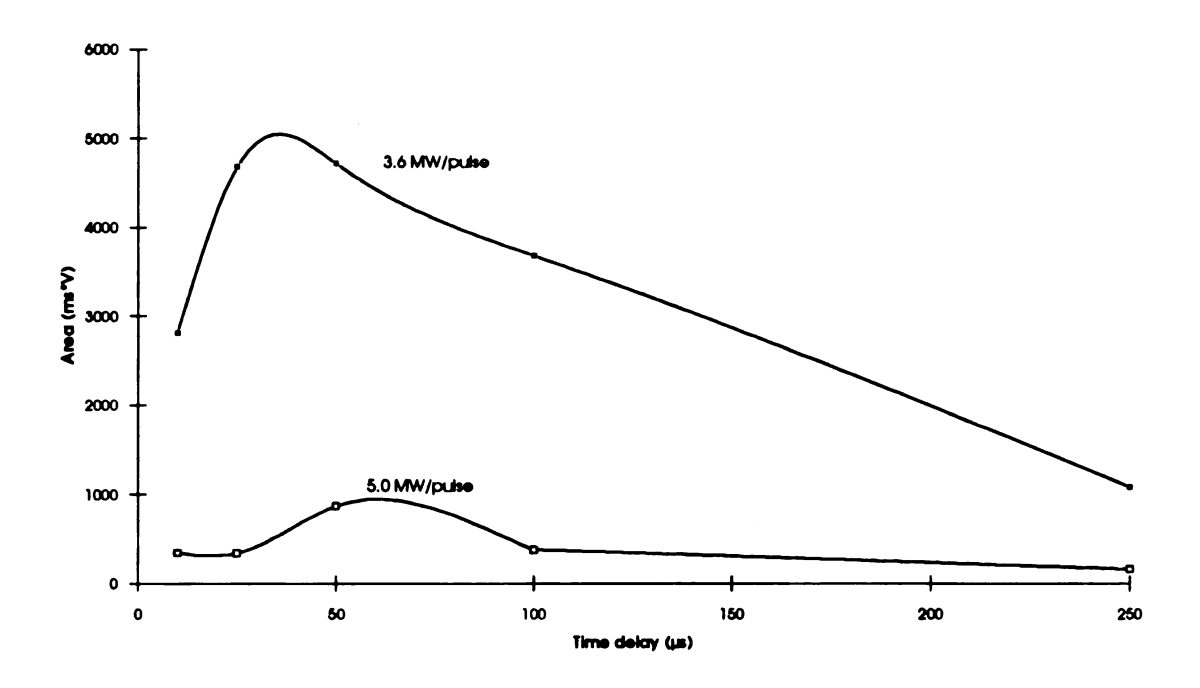


Figure 6-5. Effect of Laser Power on Magnesium Ionic Emission. 2795.5 Å Mg(II) ion line, and 2600°C atomization temperature.

At intermediate laser powers between the breakdown threshold of the gas and almost complete ionization of the analyte to the second ionization stage (M^{2+}), there is an optimum level of excitation for detecting each element. In general, the ideal laser power and time delay for alkali, alkaline earth, and transition metals is between 3-4 MW/pulse and 25-50 μ s, respectively. However, there is a compromise which exists between the optimum laser power and atomization temperature (see

Chapter 5). If a high atomization temperature is required for a determination, a corresponding high laser power must be used. The higher laser power assures that the laser plasma does not extinguish and has sufficient energy to maintain the excitation conditions during the atomization cycle. By using slightly higher laser powers, the sensitivity of the determination is reduced. This is partially compensated by using longer time delays where the peak ionic emission occurs.

E. Optimization of Experimental Conditions

Most often the analytical signal is adjusted by varying experimental parameters to maximize its magnitude. However, in most cases, this does not lead to the best signal reproduciblity. Instead, the signal-to-background ratio (SBR) in conjunction with the signal-to-noise ratio (SNR) is used to optimize measurement conditions. Ideally, the experimental parameters that result in the highest SBR and SNR will yield the best detection limits.

The intensity of the background continuum is dependent on the wavelength, laser power, and time delay. Figure 6-6 shows the effect of the laser power on the intensity of the background continuum. Each measurement was taken 25 µs after plasma formation at the Cl(I) 8375 Å line. The atomization cycle was not used for this study. There is a linear correlation (y=0.535x-0.285, r²=0.992) between laser power and intensity of the background continuum. Because the boxcar integrator has a maximum input of 100 mV, the minimum laser power must be used in order to prevent overloading the input. This limitation can be

overcome by making the measurement later in time where the background emission has decreased.

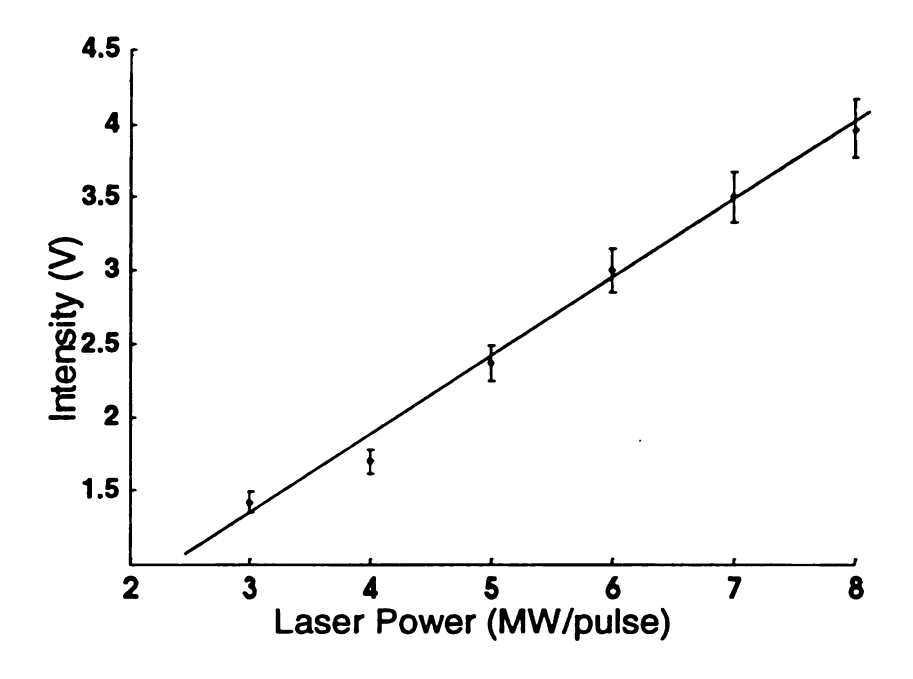


Figure 6-6. Effect of Laser Power on Background Continuum. 8375 Å Cl(I) line, and 25 µs time delay.

The background continuum intensity is very high after plasma formation and growth, but rapidly decays at the end of the laser pulse. Figure 6-7 shows the relationship between the background intensity and time delay. The background was collected at the Zn (II) 2062 Å line with a laser power of 3 MW/pulse and no atomization cycle. Thus, it is advantageous to take analytical measurements after the background emission has decreased.

Figure 6-8 shows the SBR at the Ca(II) 3933 Å line from a 50.7 ppm calcium aqueous solution at various time delays. The optimum SBR for Ca(II) emission occurs 50 µs after plasma formation. This is

representative of all elements studied using the optimum laser power for each determination.

Figure 6-9 shows the signal-to-noise ratio for the background continuum. The root mean square noise in the background was estimated as one-fifth the peak-to-peak voltage (5). The optimum SNR occured at 50 µs. In most emission-based techniques, noise in the background emission of the excitation source ultimately determines the limit of detection (6). Thus, background noise is minimized by making measurements using a 50 µs time delay.

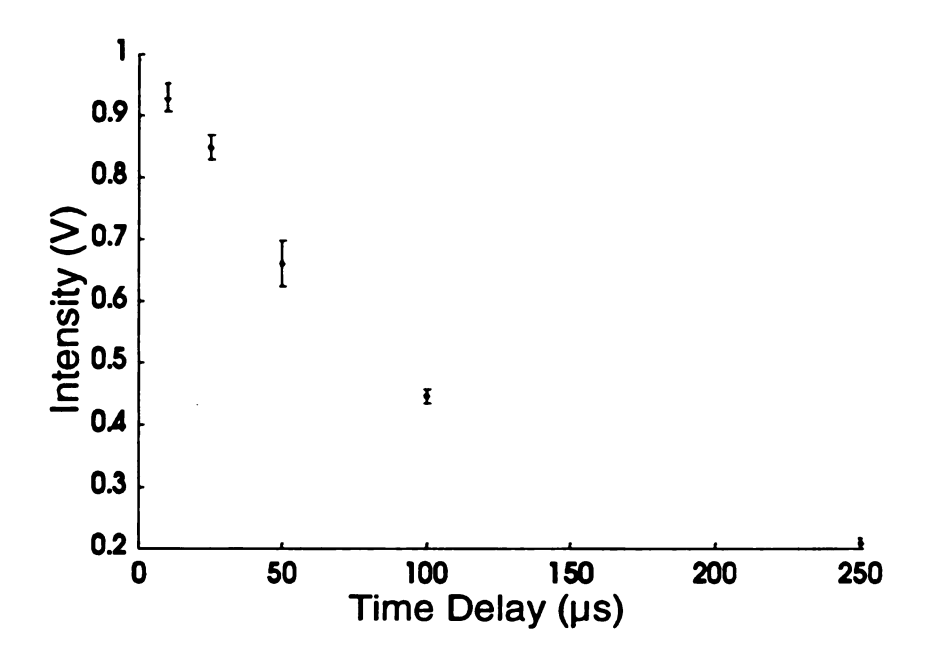


Figure 6-7. Time-resolved Relationship of Background Intensity. Zn(II) 2062 Å line, and 3 MW/pulse laser power.

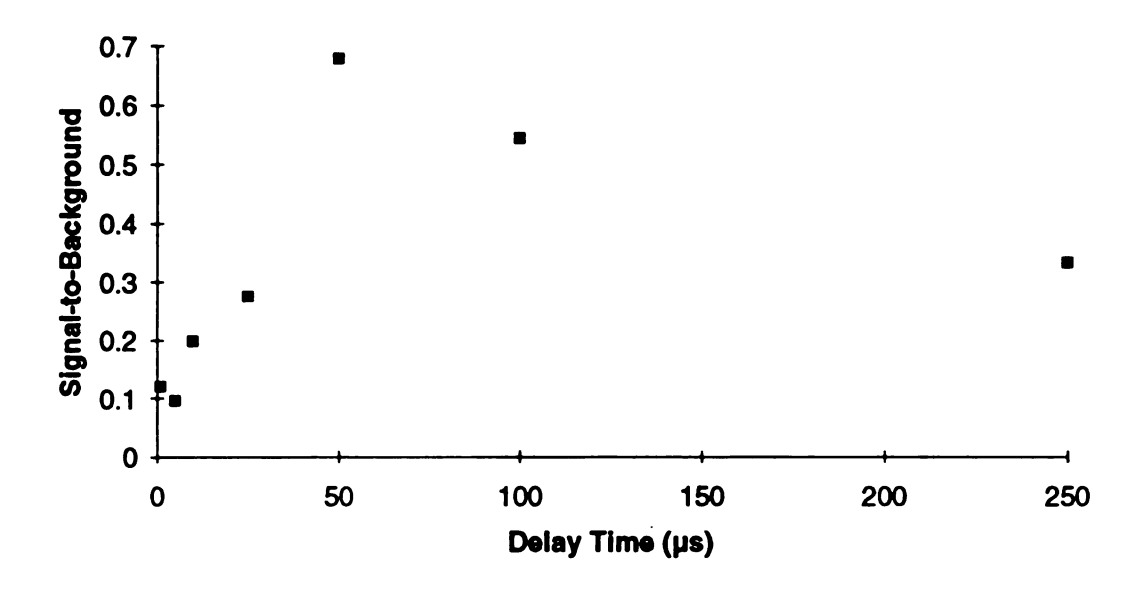


Figure 6-8. Effect of Time Delay on SBR for Ca(II). Ca(II) 3933 Å line, 4 MW/pulse laser power, and 3000°C atomization temperature.

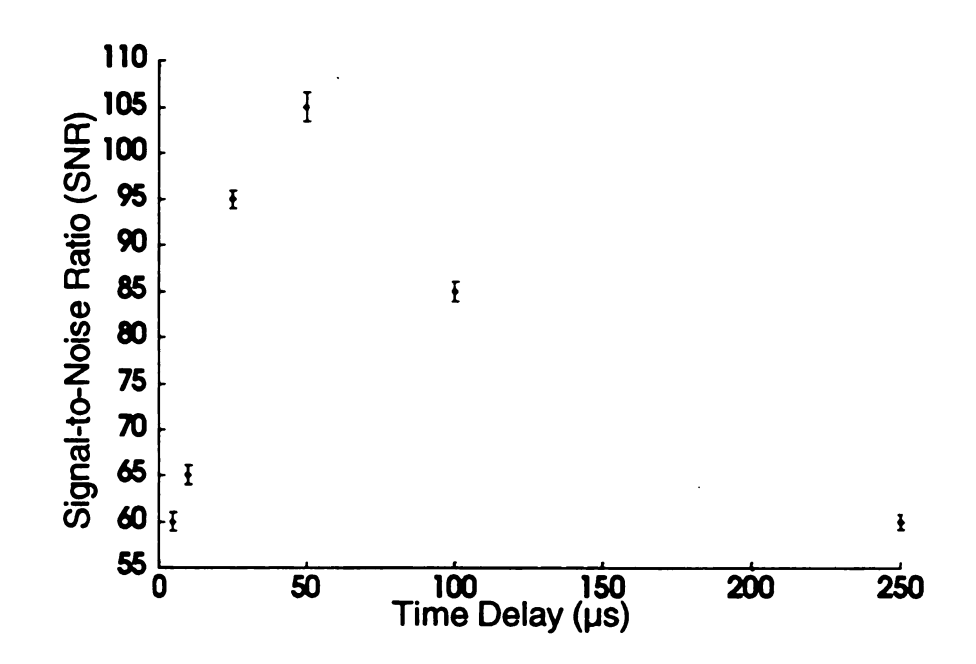


Figure 6-9. Signal-to-Noise Ratio for the Background Continuum at Various Time Delays. Fe(II) 2599.4 Å line, and 3.0 MW/pulse laser power.

The effect of signal reproducibility at various time delays is shown in Figure 6-10. The %RSD values were calculated based on 5 injections using a 100 ppm zinc solution, and collecting Zn(II) emission at 2062 Å analysis wavelength. The sample was atomized using a temperature of 3000°C. The best signal reproducibility occurred 25 µs after plasma formation.

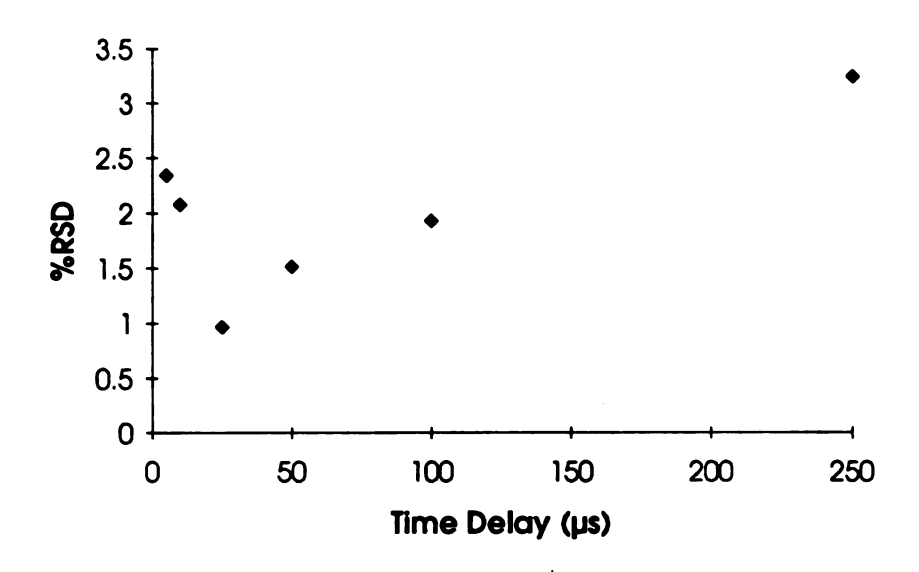


Figure 6-10. Effect of Time Delay on %RSD of Zn(II) Signal. 100 ppm Zn, Zn(II) 2062 Å line, and 3000°C atomization temperature.

As seen from the figures 6 to 10 in this section, the maximum SBR and SNR occur between 25-50 µs when the optimum laser power is used. Three advantages arise when the optimum laser power and time delay are used for a determination. First, the maximum sensitivity for the analyte is acheived. Second, the SBR and SNR maxima occur in the same time range. This simplifies the optimization of experimental conditions

because the SBR can be calculated during an actual determination. This condition also provides the lowest detection limit. Third, the background intensity has also decreased by approximately 40% during this the time delay as compared to the initial magnitude. Thus, laser power between 3 and 4 MW/pulse and time delays between 25 and 50 µs are preferred for determination of alkali, alkaline earth, and transition metals.

F. Development of the Glass Chimney

The results of the factorial experiment in Chapter 5 show that the laser plasma is affected by the increase in argon gas temperature as a result of the atomization cycle of the CRA. The laser plasma prior to this factorial experiment was formed as close as possible (6 mm) to the carbon rod surface. This inherently maximizes the transport efficiency and reproducibility of the atomic vapor to the laser plasma. When the laser plasma was formed at the 6 mm height, the optimum laser power could not be used since the laser plasma would extinguish during the atomization cycle. To compromise, the atomization temperature was lowered, and results were marginal at best. With the lower atomization temperature, incomplete volatization of the analyte creates memory effects. Because of the factorial experiment and poor analytical results, the laser plasma was formed higher (10 mm) above the carbon rod surface. The 10 mm height was chosen by considering the following three aspects: (1), the further the analyte vapor must travel, the more dilute the analyte vapor becomes and the poorer the detection limit; (2), when the analyte vapor must travel further, irreproducibility in

transport due to turbulent flow is enhanced; and (3), as shown in Chapter 5, the argon gas temperature decreases rapidly with increasing height above the carbon rod. The new height provides a compromise of the above three aspects. The main consideration is the height above the carbon rod surface at which the laser plasma is formed. This dictates the laser power required to produce and maintain the laser plasma. By moving it further away, a more stable plasma using lower laser powers can be used. In addition, the higher height allows the proper atomization temperature to be used for vaporizing the analyte.

However, after the plasma was formed at the new height, the relative standard deviation (%RSD) increased from approximately 15% to as high as 50%. There are several sources of imprecision that determine the overall reproducibility of the technique. Table 6-1 lists these sources along with approximate magnitudes where appropriate. The %RSD values were estimated from experimental results. There were several modification made to the CRA to decrease the sources of imprecision which are discussed below.

Table 6-1. Sources of Imprecision for CRALIBS

Source of Imprecision	Magnitude of Imprecision (%RSD)
Sample Introduction [†]	3-7 %
Atomization Temperature [†]	5 %
Laser Pulse Energy [‡]	4 %
Background Plasma Noise [†]	1 %
Digitization of Signal [†]	0.1 %
Transport Reproducibility [§]	25 %

- † Experimentally determined after the addition of the glass chimney
- ‡ See Spectra-Physics Quanta-Ray DCR-11 Instructional Manual (part number 110A)
- Estimated from data with and without the glass chimney (see Table 6-2)

Sample introduction should be the largest source of imprecision in this technique. To decrease the error in sample introduction, a notch is created in the center of the carbon rod, but accurate placement of the sample in the notch of the carbon rod using a microsyringe is difficult. In general, electrothermal atomization techniques have %RSD values for sample introduction of 3-7% (5). The error in sample introduction for this technique was determined from experiments after the development of the glass chimney as discussed later. The errors are comparable to those obtained by other workers.

The brass stand which mounts the carbon rod acts as a heat sink.

This creates a temperature gradient across the carbon rod during the

atomization cycle. Precision was improved by increasing the length of the carbon rod from 1 to 3 cm in length. The new length is the maximum length which can be mounted in the present design of the brass stand inside the CRA.

The power supply used to heat the CRA can reproduce the atomization temperature over the course of several days without readjustment. However, as the carbon rod degrades, the atomization temperature decreases slightly. Since this decrease occurs over several hundred runs of the CRA, this source of imprecision is a minimal contributor to the overall precision.

The pulse-to-pulse reproducibility of the laser is approximately 4% (7), and is very stable over many hours of use (5% over 10 hours). This source of imprecision is minimized by using the optimum 10 Hz pulse rate of the laser. The background noise from the plasma is related to the pulse-to-pulse reproducibility of the laser. Since the variation in the background noise is approximately 1%, this provides further evidence that the variance in laser pulse energy is minimal. The background noise is also minimized by using the appropriate time constants on the boxcar integrator and on the output of the averager.

Another source of imprecision is the digitization of the signal. The resolution of the IBM-DACA board in the present configuration is 4.88 mV. If the average signal is 5 V, the %RSD of digitizing the signal would be 0.1 %. This source of imprecision is clearly insignificant.

The final source of imprecision is the transport reproducibility of the atomic vapor to the laser plasma. The main cause of irreproducible transport of analyte vapor is the creation of turbulent flow between the carbon rod and the laser plasma caused by the atomization cycle. Moving the laser plasma 4 mm further away increased the mixing of the atomic vapor above the CRA. Table 6-2 shows the correlation between atomization temperature and the %RSD obtained. There is a direct correlation between the atomization temperature and the amount of tubulent flow. The turbulent flow results from the cool argon gas flowing around the carbon rod during the atomization cycle. The sudden temperature increase results in turbulent flow.

Table 6-2. Effect of Atomization Temperature on %RSD

Element	Atomization Temperature	%RSD
Zn	2000 °C	4.6
Na	2300 °C	13.9
Mg	2500 °C	24.2
Ca	2600 °C	25.9

To prevent mixing of the analyte vapor in the atomization chamber and to direct the analyte vapor through the laser plasma, a glass chimney was placed over the brass stand of the CRA. The design of the glass chimney is discussed in Chapter 3. The addition of the glass chimney reduced the %RSD for all determinations to 10% or less.

The glass chimney also increased the sensitivity of this method. Figure 6-11 shows the enhancement of the peak height obtained from 110 ng of calcium. The SNR increased from 41 to 154. The peak maximum also shifts in time, further indicating a turbulent mixing flow was present without the glass chimney.

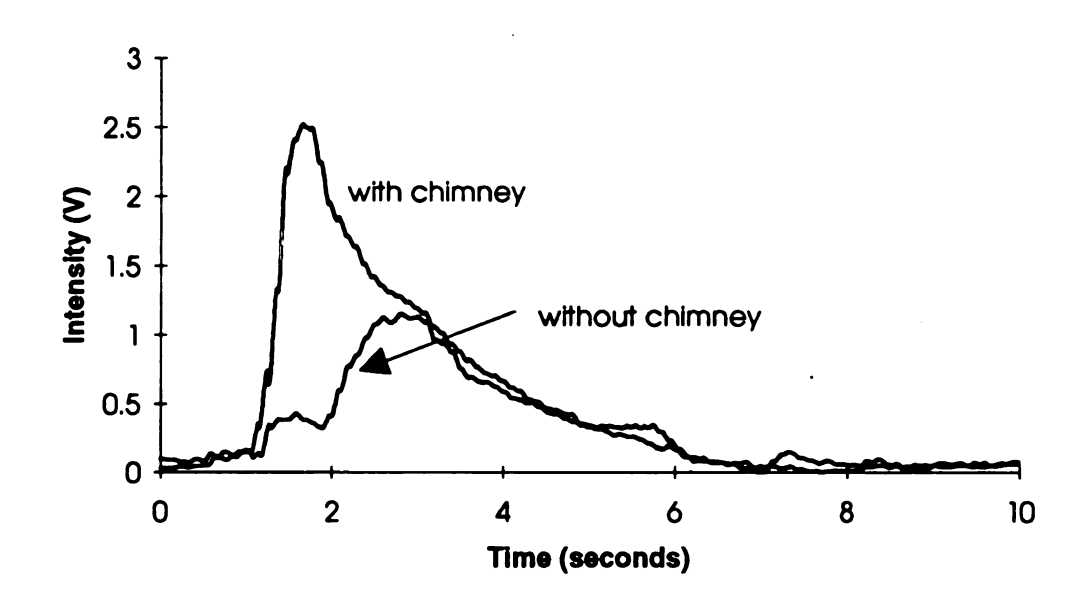


Figure 6-11. Effect of Glass Chimney on Sensitivity. 3933 Å Ca(II) line, 50 µs time delay, 2600°C atomization temperature, and 3.5 MW/pulse laser power.

G. Analytical Detection of Elements

Figure 6-12 shows the working curve for the detection of Cr(II) at 2677.2 Å. The atomization temperature was 2950°C and the laser power was 3.6 MW/pulse. This is a typical working curve obtained for all elements studied in this dissertation. The equation of the line for Cr(II)

is y=0.046x+0.058 with a coefficient of determination of 0.997. The average %RSD value for the determination of chromium was 8.2%.

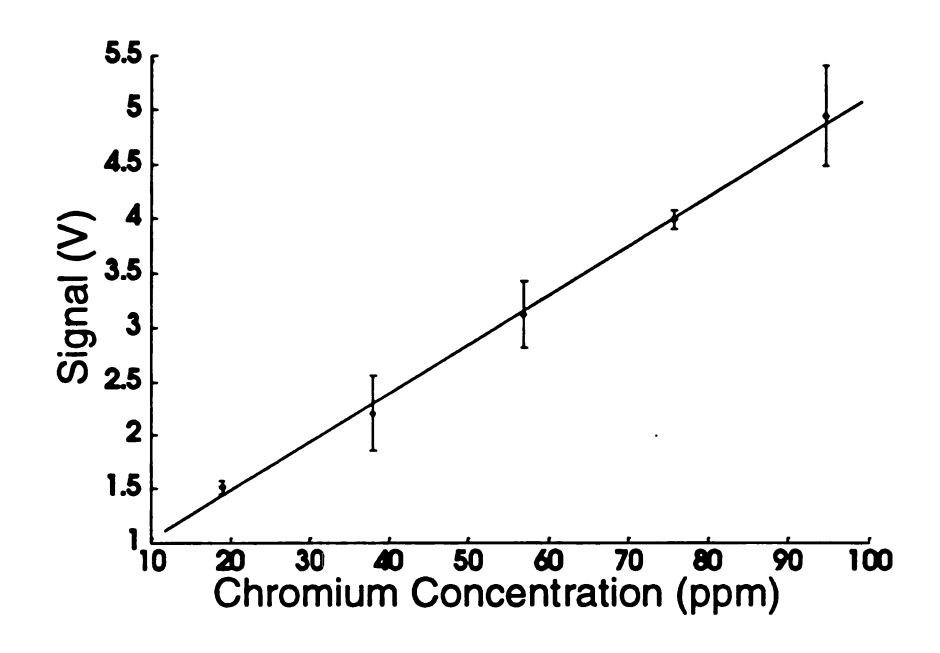


Figure 6-12. Working Curve for Chromium. 2677.2 Å Cr(II) line, 25 µs time delay, 2950°C atomization temperature, and 3.6 MW/pulse laser power.

Since analyte emission varies with time delay, a study was performed to determine the effect of sensitivity for the working curve. A comparison of the sensitivities for working curves using calcium is given in Table 6-3. This is representative of all elements, but is dependent on the relative sensitivity of the particular element. When high sensitivity is required the optimum time delay for the element can used. With the high sensitivity, a large background emission accompanies the signal. This limits the dynamic range because the signal exceeds the maximum input voltage of the boxcar averager. However, at longer time delay the

background has decreased significantly, and can be used to extend the dynamic range but with a loss of sensitivity.

Table 6-3. Analytical Sensitivities for Calcium. 3933.95 Å Ca(II) line, 2900°C, and 4.0 MW/pulse laser power.

Time Delay (µs)	Slope (V*ms/ppm)	Intercept (V*ms)	Coefficient of Determination
25	79.9	2957	0.960
50	100.3	1788	0.955
100	66.1	3985	0.985
250	11.6	475	0.950

The overall sensitivity for an element is affected by the same factors that influence the analyte emission as discussed earlier. The best region for detection is where the background is very low. This will give the largest dynamic range for a given set of experimental conditions. Experimentally, the background emission is very low at wavelengths below 3000 Å and above 5000 Å.

Table 6-4 shows the detection limits (DL) and analysis wavelengths for the determination several elements. The optimum experimental conditions were used for each element. The detection limit (DL) values reported were calculated by defining the DL as three times the standard

deviation of the lowest concentration standard solution divided by the slope of the working curve (5).

Table 6-4. Detection Limits for CRALIBS

Element	Detection Limit (ng)	Analysis Wavelength (Å)
Na [†]	6.0	5890.0
Mg	15.0	2795.5
Ca	13.0	3933.7
Fe	11.5	2599.4
Cr	7.5	2677.2
Zn	7.5	2062.0
рt	8.8	2149.5
CI†	4500	8375.5

[†] Detected as Na(I), P(I) and Cl(I)

The DLs for all the elements studied except for chlorine are in the nanogram range (low ppm). The high DL for chlorine is because of the high excitation energy. The peak emission of Cl(I) occured with a laser power of 8 MW/pulse, whereas the other elements' peak emission occured between 3-4 MW/pulse. Chlorine was detected at the Cl(I) 8375 Å line by using a red sensitive PMT (Model R666, Hamamatsu, Bridgewater, NJ). The Cl(I) transition used is 10.4 eV above the ground state. Detection of this transition is possible because of the high

excitation energy of the laser plasma. But this transition is high enough where excitation becomes inefficient. In contrast, detection of atomic emission from chlorine in an ICP must be performed in the vacuum ultraviolet using a transition that is 9.2 eV above the ground state (4). Emission from Cl(II) was not detected because the ionization potential is 13.8 eV, and the plasma does not have sufficient energy to both ionize and excite chlorine. Phosphorus is also very difficult to ionize, and detection was made using the P(I) 2149.5 Å line, for which the upper energy level is 7.2 eV above the ground state. In this case, the plasma had sufficient energy such that sensitivity was not lowered.

As shown in the next section, the ionization plus excitation potential for zinc (12.01 eV) is higher than for chlorine (10.4 eV), but the detection limit for zinc is not affected. This is because the energies of the two predominant excited argon-metastable atoms (11.55 and 11.76 eV) present in the plasma (8) match the upper energy level of the excited Zn(II). The mechanism of excitation is further discussed in Chapter 7.

H. Analyte Emission Dependence on Concentration

In atomic emission spectrometry (AES), the analyte signal is theoretically proportional to the concentration of the analyte in solution (5). This relationship is true when there is no change in source temperature or instrumental factors, and no self-absorption. Curves of growth are a powerful diagonistic tool to determine if a change in source temperature or self-absorption is present. Curves of growth are log-log plots of working curves. Table 6-5 shows the slopes for the curves of growth for several elements. The coefficient of determination for each

curve of growth was greater than 0.98. The predicted theoretical slope is 1, which reflects the expectation that analyte emission is linearly related to the concentration.

Since the average slope for the curves of growth is less than one, either self-absorption or a change in excitation conditions occured. Laser plasmas are optically thin, reducing the chance of self-absorption (9). In addition, the concentrations used in these experiments were near the detection limit, which also minimizes self-absorption. Thus, the excitation temperature of the plasma is apparently affected by the analyte vapor. The excitation temperature of a source has been shown to vary depending on the combined excitation and ionization potential of the species (10). As the excitation and ionization potential of the species increase, the source temperature decreases. This effect is shown in Table 6-5. Generally, as the energy of the upper level in the excited species increases, the slope of the log-log plot decreases. The exception is the slope for chlorine. This is because chlorine was introduced into the plasma using the sodium chloride salt. The high concentration of sodium maintained the excitation conditions in the plasma. The excitation interference is also affected by the matrix, as seen by the slopes in the determination of iron and phosphorus in fly ash.

The slope of the log-log plot does not affect the overall accuracy of the technique. It simply shows that the excitation temperature is altered due to the analyte vapor.

Ideally, the excitation conditions in the plasma should remain constant for best reproducibility. Working curves for each analytical

determination must still be prepared for each given set of instrumental factors and experimental conditions.

Table 6-5. Slopes for Curves of Growth for CRALIBS

Element	Slope	Energy of Upper Level (eV)
Calcium	0.96	3.15
Iron	0.96	4.77
Chromium	0.74	6.14
Phosphorus	0.75	7.20
Chlorine	1.05	10.4
Zinc	0.46	12.0
Iron (in fly ash)†	0.33	4.77
Phosphorus (in fly ash)†	0.61	7.20

[†] see section J in this chapter

I. Detection of the Calcium Chloride Salt

In electrothermal atomization, pre-volatilization of the analyte can occur in sample matrices which contain large concentrations of chloride. This is due to the formation of a volatile chloride salt which is vaporized during the charring cycle. This volatilization interference can also occur when hydrochloric acid is used in the preparation of the sample (11). It can go undetected if the sample matrix is unknown, or if an improper

charring temperature is selected. Figure 6-13 shows the prevolatilization of calcium as calcium chloride using CRALIBS.

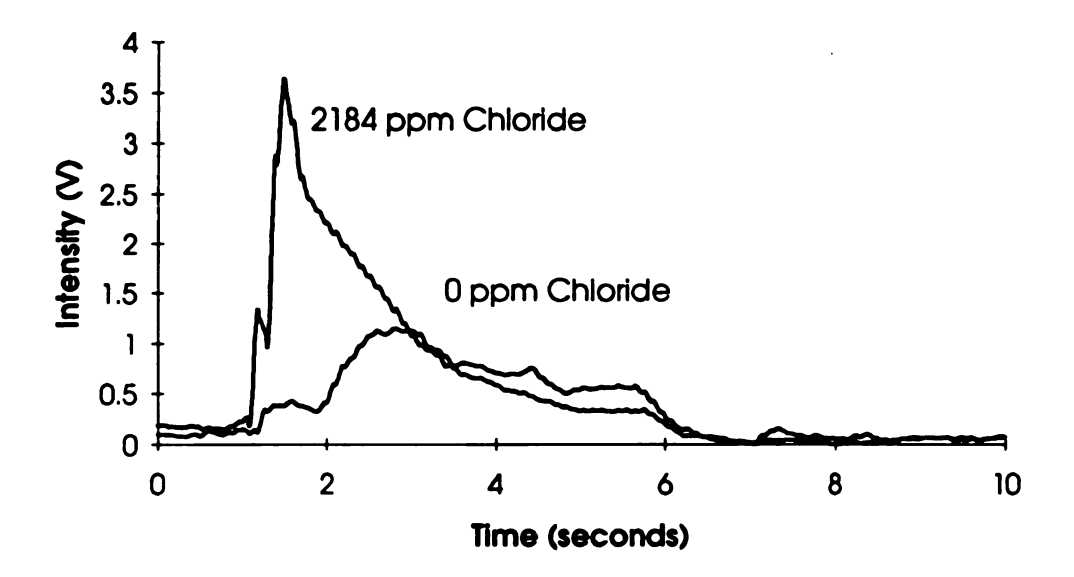


Figure 6-13. Effect of Chloride on Ca(II) Emission. 3933 Å Ca(II) line, 50 µs time delay, 2600°C atomization temperature, and 3.5 MW/pulse laser power.

Upon addition of 2184 ppm chloride as sodium chloride, the mechanism by which calcium volatilizes from the carbon rod is changed. Without chloride present calcium forms an oxide which decomposes to calcium atoms and carbon monoxide (12). This transformation occurs at an atomization temperature of approximately 2600°C. With the addition of chloride to the sample matrix, the calcium forms calcium chloride which has a boiling point of 1600°C. The peak maximum of the Ca(II) emission due to volitilization of calcium chloride occurs two seconds into the atomization cycle because the power supply heats the CRA at a

rate of 800°C/s. When chloride is not present in the matrix, peak emission from Ca(II) does not occur until about three seconds, which corresponds to the appearance of calcium atoms.

J. Determination of Fe in Coal Fly Ash

After investigations the elemental and optimization experimental parmeters, the CRALIBS technique was applied to the determination of Fe and P in coal fly ash. The coal fly ash was obtained from Detroit Edision (DE) (13). Independent determinations by ICP-AES found the sample had 5.76% Fe and 0.55% P. The fly ash for the experiments performed here was prepared by dissolving it in a mixture of sulfuric, hydrochloric, and phosphoric acids, followed by digestion for several hours until dissolution was complete. These experiments used a combination desolvation and charring cycle to remove the water and any volatile organics that may interfere with the determination. The charring cycle lasted 20 seconds. The temperature of the charring stage slowly increased over the 20 second interval to a final temperature between 100 °C and 200°C. When the charring cycle is omitted the sample reproducibility is 8.9%. If the charring cycle is used the precision improves to 3.2%. The experiments were performed by using external standards and standard additions. The latter method is used to compensate for matrix matching difficulties, interelemental suppression, and for physical and chemical interferences. The Fe analysis was also performed using ICP-AES for comparison.

Linear calibration curves were obtained for both methods. Table 6-6 summarizes the results obtained using CRALIBS. Similar slopes were obtained for external standards and the standard additions methods indicating that there were no chemical interferences present in the determination. Both methods reported higher percentages than the certified value but within the experimental error. This is attributed to the inadequate blank subtraction in the determination.

Table 6-6. Determination of Fe in Coal Fly Ash using CRALIBS

Method of Analysis	Slope(V*s/ppm)	%Fe in sample
External Standards	13.67 ± 1.4	5.95 ± 0.56
Standard Additions	11.5 ± 2.6	6.12 ± 0.61

The ICP-AES results are listed in Table 6-7. Linear calibration curves were obtained using external standards and standard additions. The slopes of the working curves between the two methods differ significantly indicating that an interference was present using the ICP method. Since the ICP is optical thin, self-absorption of the analyte emission is negligible.

Table 6-7. Determination of Fe in Coal Fly Ash using ICP-AES

Method of Analysis	Slope(V/ppm)	%Fe in sample
External Standards	1.47 ± 0.01	4.39 ± 0.40
Standard Additions	1.12 ± 0.04	5.34 ± 0.15

This is because of a non-specific interference. Since viscous acids were used to dissolve the fly ash, the flowrate of sample into the ICP was decreased due to the increase in viscosity of the sample. This decrease was reflected in the lower signal intensity obtained for the fly ash sample, which resulted in a lower %Fe for the external standards method. This is the main limitation for a determination using an ICP-AES. The standard additions method compensated for this non-specific interference by maintaining the sample matrix for each sample. By introducing the sample with a microsyringe, this sample introduction limitation is overcome.

K. Determination of P in Coal Fly Ash

The determination of the phosphorus content of coal fly ash was also performed. Both external standards and standard addition methods were used for comparison. Table 6-8 shows the results for the %P in coal fly ash with the CRALIBS technique.

Because the slopes of the two methods differed significantly, an interference occurred in the determination of phosphorus. The standard additions method was more accurate, and is the preferred

method to compensate for interferences. The interference is from either a chemical interference originating from vaporization of the analyte from the carbon rod or an excitation interference occurring within the laser plasma.

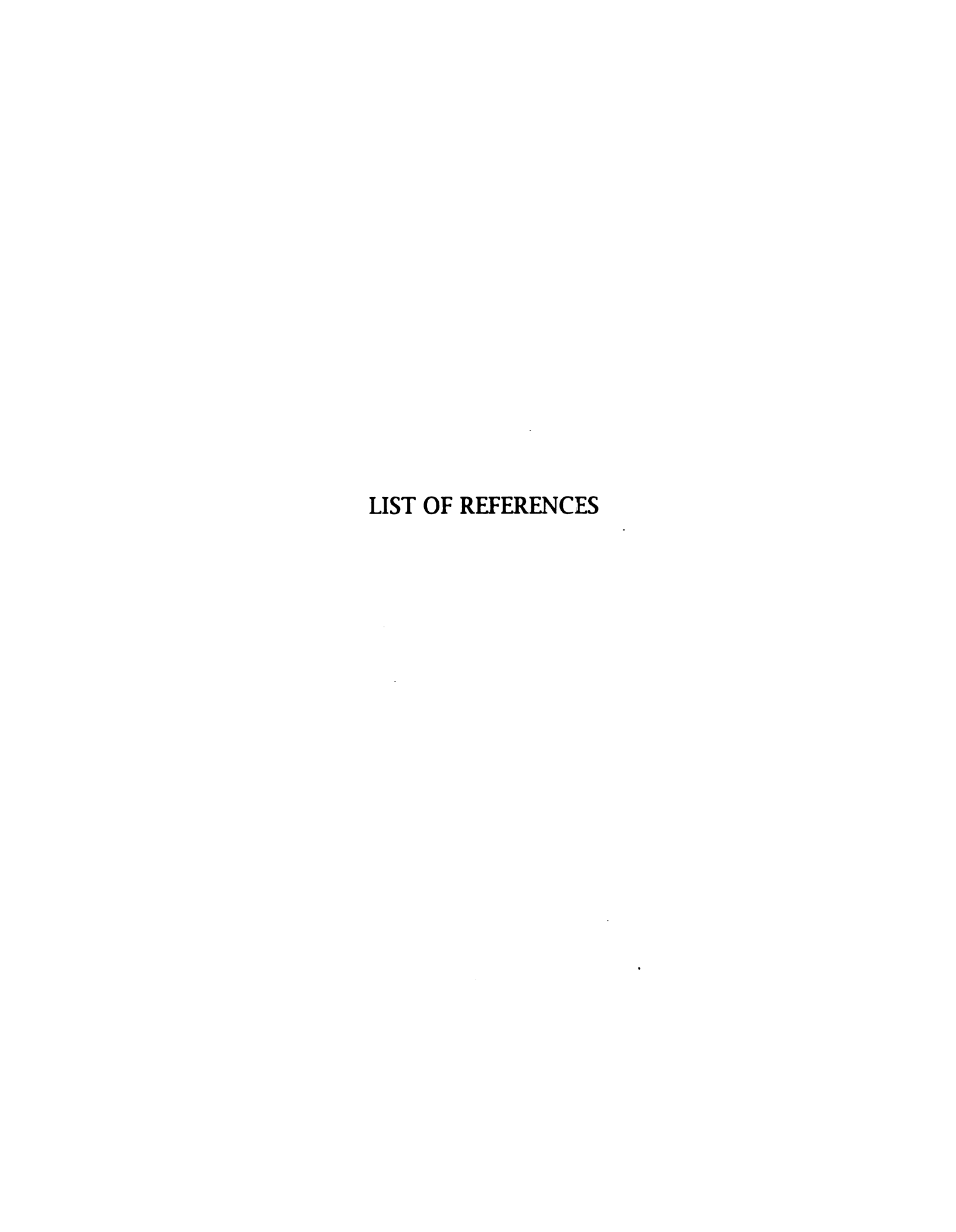
Table 6-8. Determination of Phosphorus using CRALIBS

Method of Analysis	Slope(V*s/ppm)	%P in sample
External Standards	0.22 ± 0.03	0.059 ± 0.004
Standard Additions	0.122 ± 0.002	0.47 ± 0.02

The mechanism by which phosphorus atomizes off the carbon rod depends strongly on experimental conditions. Depending on the partial pressure of oxygen, the formation of gaseous PO and PO₂ have been detected (14). When uncoated graphite is used, the partial pressure of oxygen is very low (15), and the formation of oxides is highly improbable. Under these conditions, it has been shown that gaseous HCP forms (14). This is the most likely mechanism by which phosphorus was atomized in this experiment, since the carbon rods were not pyrolytically coated. P₂ and HPO have also been detected (16) as products in the atomization of phosphorus. Since the laser plasma has been shown to dissociate molecular species, any chemical interference due to the formation of oxides of phosphorus is minimized. The matrix could also cause a suppression in the atomization rate of the analyte. This interference can

be both non-specific and specific. However, if this interference occurred, the peak widths obtained with external standards would differ from those obtained by the standard additions methods. Experimentally, the peak widths were 4.0 seconds for both methods. In addition, the peak shapes were identical for both methods.

In atomic emission based methods, excitation interferences can occur within the plasma (5). This interference is caused by a component(s) present in the coal fly ash matrix that were not removed during the charring cycle. These concominants were vaporized into the plasma, altering the excitation temperature. Since analyte emission is dependent on the temperature of the plasma, emission can be either raised or lowered depending on how the concominant affects the plasma. When the analyte has a low excitation energy, small changes in the plasma temperature do not affect the emission to the same extent as for an analyte of high excitation energy. Since phosphorus has a high excitation energy, it is concluded that the coal fly ash matrix lowered the plasma excitation temperature. This is also verified in Section H of this chapter. This interference decreased the sensitivity of the phosphorus determination.



LIST OF REFERENCES

- 1. CRC Handbook of Chemistry and Physics, Weast, R. C., Ed., CRC Press, Inc, Boca Raton, FL, 1984, Section E
- 2. Winge, R., Fassel, V., Peterson, V., Floyd, M., Inductively Coupled Plasma-Atomic Emission Spectrometry: An Atlas of Spectral Information, Elsevier, New York, 1985
- 3. Ouchi, G., LC-GC, 9, 474(1991)
- 4. Boumans, P. W. J. M., in *Inductively Coupled Plasma Emission Spectrometry*, Boumans, P. W. J. M. ed., Wiley-Interscience, New York, page 222
- 5. Ingle, J., Crouch, S., Spectrochemical Analysis, Prentice Hall, Englewood Cliffs, NJ, 1988
- 6. Ottaway, J., Bezur, L., Marshall, J., Analyst, 105, 1130(1980)
- 7. Spectra-Physics Quanta-Ray® DCR-11 Pulsed Nd:YAG laser Instruction Manual, Part Number 110A, Mountain View, CA, 1987
- 8. Chan, S. and Montaser, A., Spectrochim Acta, 40B, 1467 (1985)
- 9. Tourin, R., J. Quant. Spec. Rad. Trans., 3, 89 (1963)
- 10. Boumans, P. W. J. M, *Theory of Spectrochemical Excitation*, Plenum Press, New York, 1966
- 11. Welz, B., Atomic Absorption Spectrometry, 2nd Ed., VCH, Germany, 1985
- 12. Fuller, C., Electrothermal Atomization for Atomic Absorption Spectrometry, Burlington House, London, England, 1977
- 13. The author thanks Dr. P. Beckwith, Detroit Edison, Detriot, MI, for supplying the coal fly ash sample

- 14. Persson, J., Frech, W., Cedergren, A., Anal. Chim. Acta, 89, 119 (1977)
- 15. Montaser, A. and Crouch, S., Anal. Chem., 46, 1817 (1975)
- 16. Syty, A., Anal. Letters, 4, 531 (1971)

CHAPTER 7

HELIUM PLASMAS AND THEIR ANALYTICAL APPLICATIONS

A. Introduction

As discussed in Chapter 6, the laser plasma is influenced by the laser power used. The argon plasma was found to be adequate for the determination of alkali, alkaline earth, and transition metals. However, the sensitivity for chlorine was substantially reduced due to the high excitation energy of the transition. Raising the laser power, increased the Cl(I) emission, with a maximum occurring at 8 MW/pulse. However, this did not improve the detection limit for chlorine.

This chapter shows that by changing to a helium atmosphere inside the carbon rod atomizer (CRA) chamber, the excitation conditions can be further enhanced within the laser plasma. Chan and Montaser (1) have shown that He-ICPs are superior to Ar-ICPs for determining elements such as halogens which possess high excitation energies. Work by Welz and co-workers (2) has also shown that detection limits are improved in the determination of chlorine and bromine by using a helium plasma for excitation in Furnace Atomic Non-thermal Excitation Spectrometry (FANES). The higher excitation conditions in the helium plasma are realized by looking at two of the postulated mechanisms (1,3) by which emission occurs in an argon ICP, and generalizing the mechanisms to laser plasmas.

The first mechanism is a Penning ionization reaction (1,4). In this mechanism, argon-metastable atoms which are formed in the Ar-ICP ionize and excite the analyte. We shall define the sum of the ionization

and ionic excitation energies to be the total excitation energy of the ion (TEI). The energies of the two predominant metastables present in an Ar-ICP are 11.55 and 11.76 eV. When an element has a TEI less than the energy of the metastables, this mecahnism directly applies. However, this mechanism does not apply to analytes, such as halogens, where the TEI is greater than the energy of the argon-metastables.

Another mechanism is a charge transfer reaction (1,5). Charge transfer between an argon ion and the analyte atoms occurs when the TEI of the analyte is less than the ionization energy argon (IE =15.76 eV). This mechanism is preferred due to the higher concentration of argon ions compared to argon-metastables in both the ICP and especially in a laser plasma.

The TEI for the halogens far exceeds the ionization energy of argon. Table 7-1 lists the average excitation energy, ionization energy, and the average TEI for each halogen (6).

Table 7-1. Excitation and Ionization Energies for Halogens

Element	Atomic Excitation Potential (eV)	Ionization Potential (eV)	Total Excitation Potential (eV) [‡]
Br	10.5	11.8	14.3
Cl	11.2	13.0	21.0
F	15	17.4	†

[†] undetermined

[‡] sum of ionization and ionic excitation potentials

Upon consideration of the two proposed mechanisms above, the detection of ionic bromine is possible using an argon plasma because the TEI is less than ionization energy of argon. However, chlorine and fluorine must be detected using their atomic emission lines because their TEI is larger than the ionization energy of argon. Ar-ICPs have attained detection limits for Cl and F of 50 and 350 ng, respectively (7.8) in gas samples. The gas samples were necessary so the energy of the plasma went only into dissociation and excitation of the halogen. By switching to a helium plasma, the excitation of all the halogens are possible because the ionization energy is 24.6 eV. Radziemski (9) determined Cl and F using LIBS. Using an air plasma, detection limits for Cl and F were 80 and 2000 ng, respectively. In a helium plasma, the detection limit was lowered to 3 ng for both halogens. Even though argon is capable of exciting the halogens, it is not an efficient process as shown in Chapter 6. Thus, it seems from the work presented in this dissertation, helium is required for the trace analysis of elements that have total excitation energies greater than 10 eV.

This cut-off point is evident when the detection limits are compared with the total excitation energy of the element. From data presented in Chapter 6, the detection limits for metals which have lower total excitation energy than Cl(I) are in the nanogram range. The detection limit for phosphorus is also in the nanogram range, but is detected using the P(I) line which has an excitation energy of 7.2 eV. The

detection limit for chlorine from the argon plasma is 4500 ng when the measurement involves Cl(I) line that has an excitation energy of 10.4 eV.

This chapter first discusses the characteristics of the helium plasma. The background emission spectrum for a helium plasma is presented. The excitation temperature and electron density of a helium plasma are compared to the argon plasma. As with the argon plasma, all temperatures and electron densities are spatially averaged. Next, the effect of experimental conditions on the time-resolved Cl(I) emission is described. Finally, the detection of chlorine in pool and tap water using a helium plasma is presented.

B. Characteristics of a Helium Plasma

The breakdown threshold for the creation of a helium plasma is much higher than for an argon plasma. In this experimental setup, the breakdown threshold was 5.0 MW/pulse. Above this threshold, the additional laser power added to the excitation capability of the plasma. Figure 7-1 shows the helium plasma spectrum at a time delay of 25 µs, produced with a laser power of 8.0 MW/pulse.

The predominant feature in the helium plasma is the emission from excited helium atoms. No helium ionic emission is detected. Another feature of the spectrum is the background continuum. Peak background emission is approximately at 3700 Å. In comparison, the argon background intensity is much greater. This is because the argon plasma is more highly ionized than the helium plasma. The helium peak widths varied from 3 to 25 Å, depending on the Stark broadening parameter for the particular emission line, but most are less than 10 Å.

In comparison, line widths in the argon plasma presented in this dissertation varied from 5 to 9 Å.

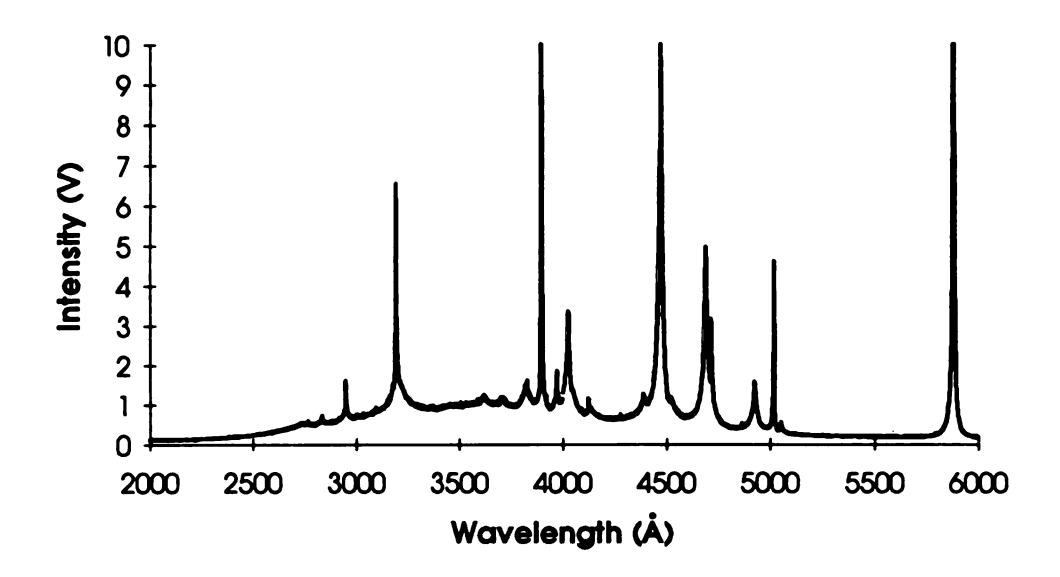


Figure 7-1. Helium Plasma after 25 µs Time Delay with a laser power of 8.0 MW/pulse.

The time-resolved excitation temperature was determined from a Boltzmann plot (see Chapter 4), using a group of He(I) emission lines at 4921.9, 4026.3, and 3888.7 Å. The data for these lines are found in the *CRC Handbook of Chemistry and Physics* (6). Because the wavelength interval was small, the photomultiplier tube transducer response was assumed constant. These were the only three lines that were not unresolved multiplets. The average excitation temperature was 5840 K. This is substantially lower than the argon plasma. The reason is because the He plasma is not as highly ionized. This compares with previously

reported temperatures for a He-ICP (1). Table 7-2 list the time-resolved excitation temperatures.

The time-resolved electron density of the helium plasma was determined. The electron density was calculated by measuring the line width of two different Stark broadened He(I) lines. The Stark broadening parameters are found in Griem (10). Table 7-3 shows the time-resolved electron densities.

The average electron density is 9.3 x 10^{16} cm⁻³. This is approximately 100 times less than for the argon plasma. The main error in determining the electron density in a helium plasma is from measuring the line widths, not from the theoretical Stark width of the emission lines. The error in determining the line widths is ± 0.5 Å. This error translates into an error in the electron density of ± 1.9 x 10^{15} cm⁻³, or $\pm 2\%$.

Table 7-2. Time-resolved Excitation Temperatures of a Helium Plasma

Time Delay (μs)	Excitation Temperature (K)	%RSD
5	5540	10.6
25	6620	7.1
50	5530	10.5
100	5660	10.5
250	5860	4.9

Table 7-3. Time-resolved Electron Densities of a Helium Plasma

Time Delay (µs)	N _e (3188 Å) (cm ⁻³)	N _e (4922 Å) (cm ⁻³)	Average (cm ⁻³)
5	1.4 x 10 ¹⁷	9.7 x 10 ¹⁶	1.2 x 10 ¹⁷
25	1.1 x 10 ¹⁷	8.5 x 10 ¹⁶	9.8×10^{16}
50	1.1 x 10 ¹⁷	8.1×10^{16}	9.6 x 10 ¹⁶
100	8.3 x 10 ¹⁶	7.7 x 10 ¹⁶	8.0×10^{16}
250	6.9 x 10 ¹⁶	7.3 x 10 ¹⁶	7.1 x 10 ¹⁶

C. Analytical Studies of Chlorine in a Helium Plasma

Because of the high ionization plus excitation energy for chlorine, detection of Cl(II) was not observed. However, detection of the Cl(I) 8375 Å emission is greatly enhanced compared to the argon plasma. Figure 7-2 show the effect of the signal-to-background ratio (SBR) at increasing laser powers. The optimum laser power for detection of chlorine is between 6 and 8 MW/pulse, where the highest SBR occurs.

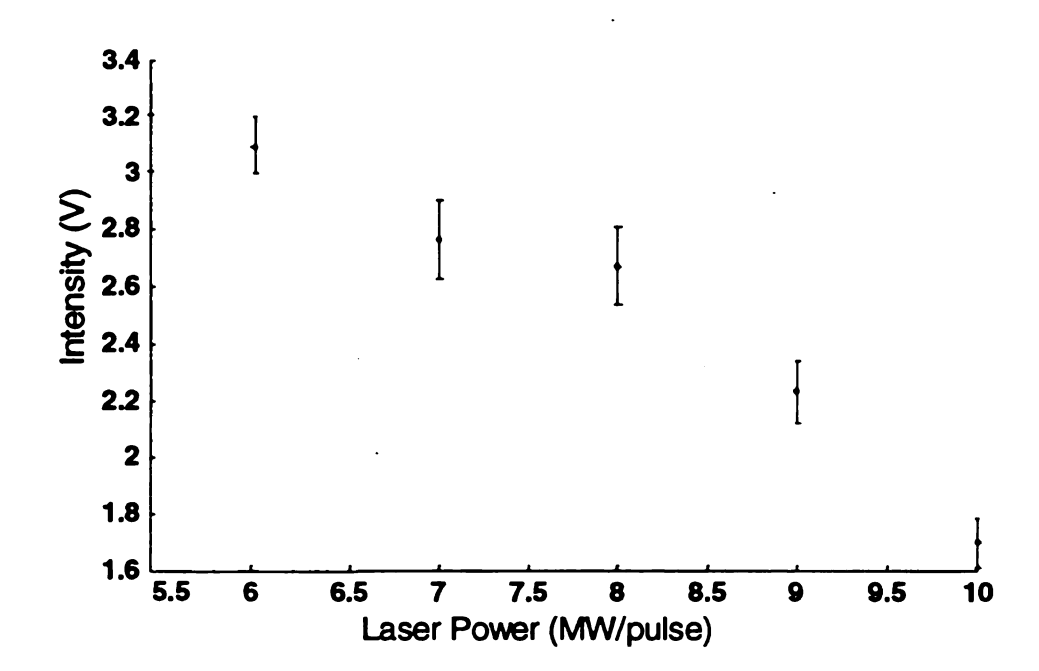


Figure 7-2. Signal-to-Background Ratio for Cl(I) in a He Plasma

At 8.0 MW/pulse laser power, the time-resolved Cl(I) emission from the plasma is shown in Figure 7-3. Peak emission for Cl(I) is 25 µs after plasma formation.

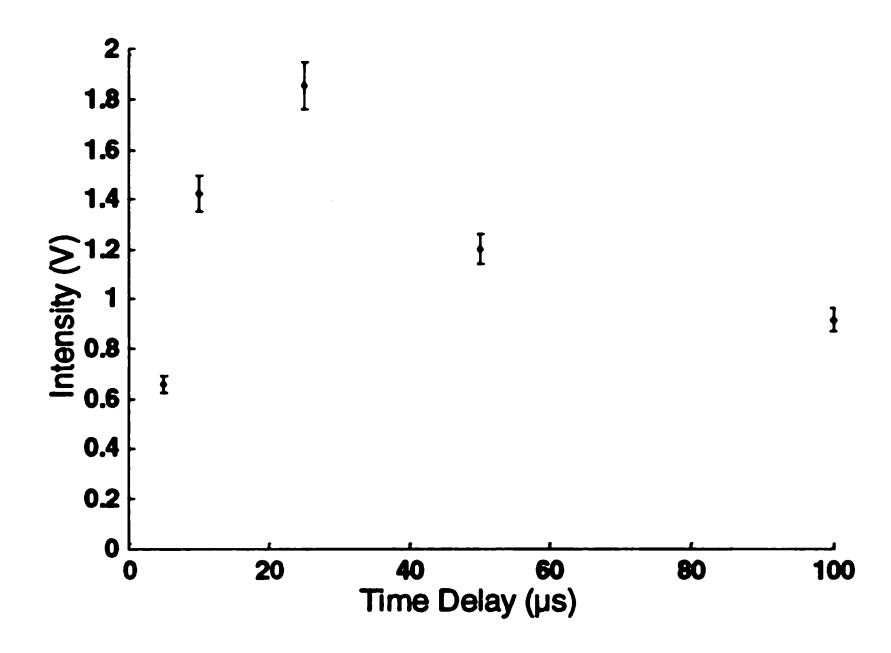


Figure 7-3. Profile of Cl(I) Emission in a He Plasma

The working curve presented in Figure 7-4 was prepared from data taken at a 25 µs time delay, a laser power of 8.0 MW/pulse, and an atomization temperature of 2600°C. The equation of the regression line is y=0.0497x+0.034 with a coefficient of determination of 0.94. The detection limit for chlorine with the helium plasma is 13 ppm (66 ng).

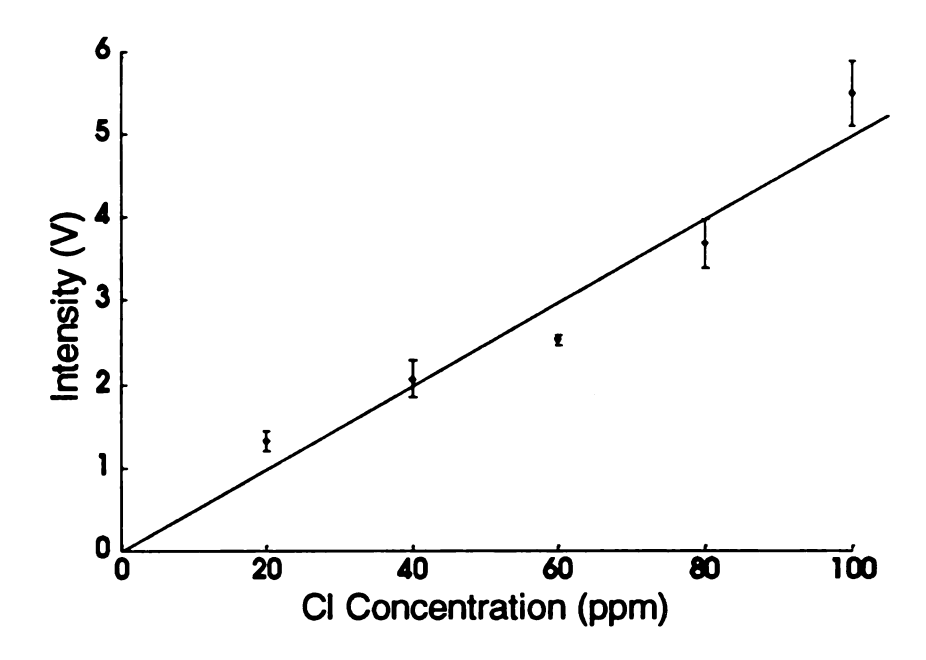


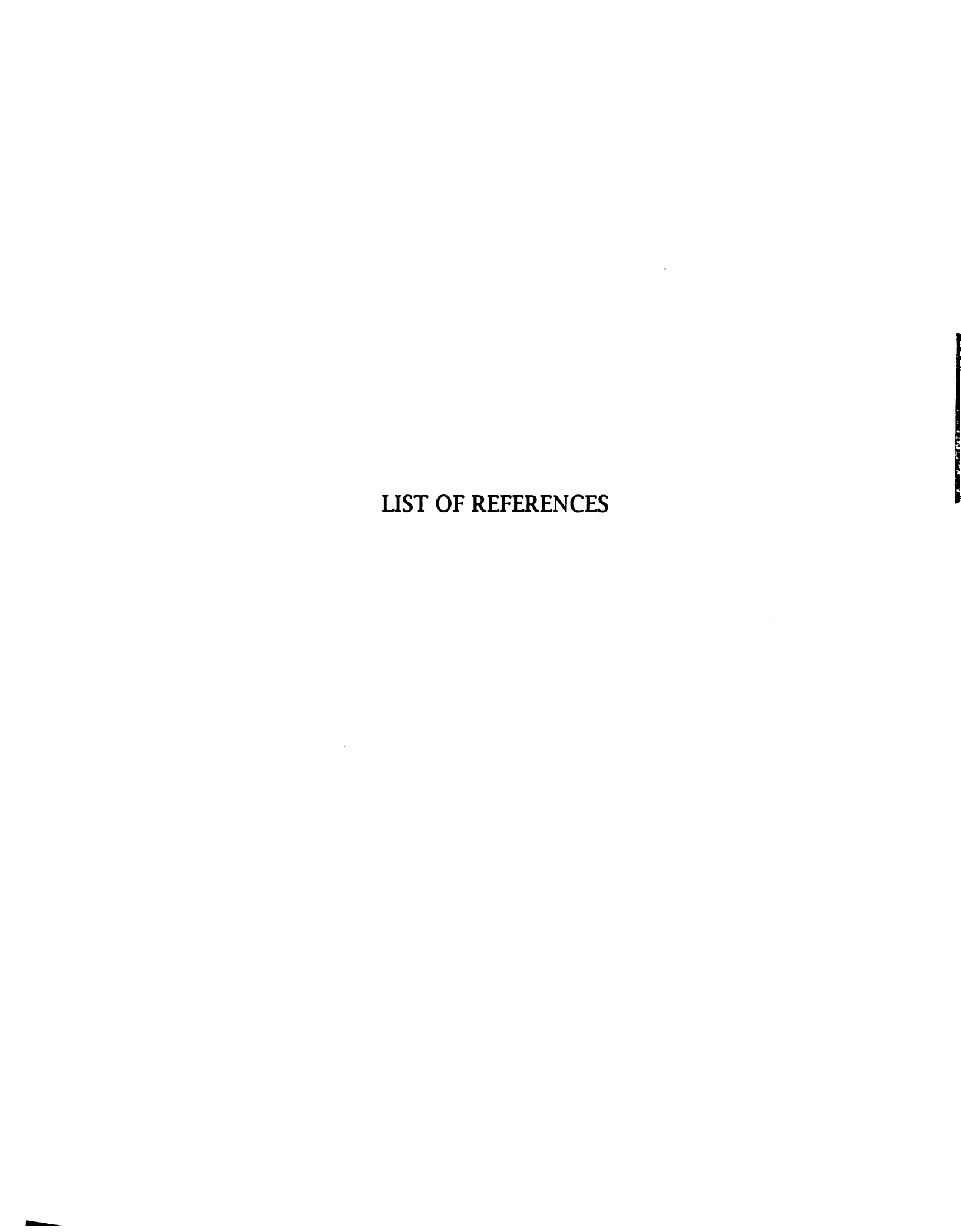
Figure 7-4. Working Curve for Chlorine. Cl(I) 8375 Å line, 25 µs time delay, and 2600°C atomization temperature.

D. Determination of Chlorine in Pool and Tap Water

The external standards method was used to determine the concentration of chlorine in pool and tap water. The pool water was obtained from Brandywine Creek Apartments (East Lansing, MI). The active ingredient is trichlorosocyanuric acid. When dissolved in water, this compound has 90% free chlorine (Cl_2). The recommended concentration of Cl in the pool is 7.6 ppm as free chlorine (11). By the CRALIBS technique, the concentration of chlorine in the pool water was 78.3 \pm 5.4 ppm. Because this technique determines the total chlorine content, which is independent of oxidation state and source, this measurement is not unexpected since the pool was most likely

overchlorinated. An independent gravimetric determination using silver chloride found 74.1 \pm 4.0 ppm Cl.

Using the same external standards, the chlorine concentration in tap water (Michigan State University, Chemistry Department) was determined. The concentration is 30.4 ± 2.6 ppm Cl. Again, this represents the total concentration of chlorine in the tap water sample. An independent gravimetric determination using silver chloride found 34.7 ± 4.2 ppm Cl.



LIST OF REFERENCES

- 1. Chan, S. and Montaser, A., Spectrochim Acta, 40B, 1467 (1985)
- 2. Dittrich, K., Radziuk, B., Welz, B., J. Anal. At. Spectrom., 6, 465 (1991)
- 3. Hasegawa, T., Haraguchi, H., Fundamental Properties of Inductively Coupled Plasmas in Inductively Coupled Plasmas in Analytical Atomic Spectrometry, edited by Montaser, A. and Golightly, D., VCH Publisher, New York, 1987
- 4. Mermet, J., C. R. Acad. Sci., Ser B 281, 273 (1975)
- 5. Schram, D., Raaymakers, I., van der Sijde, B., Schenkalaars, H., Boumans, P., Spectrochim. Acta, 38B, 1545 (1983)
- 6. CRC Handbook of Chemistry and Physics, Weast, R. C., Ed., CRC Press, Inc, Boca Raton, FL, 1984, Section E
- 7. Fry, R., Northway, S., Brown, R., Hughes, S., Anal. Chem., 52, 1716(1980)
- 8. Hughes, S., Fry, R., Anal. Chem., 53, 1111 (1981)
- 9. Cremers, D. and Radziemski, L., Anal. Chem., 55, 1252 (1983)
- 10. Griem, H., Plasma Spectroscopy, Mc-Graw Hill, New York, 1964
- 11. Pool and Patio, Inc., Holt, MI

CHAPTER 8

CONCLUSIONS AND FUTURE PROSPECTS

A. Conclusions

This dissertation has described a new method for sample introduction into a laser-induced plasma called carbon rod atomization laser-induced breakdown spectrometry, or CRALIBS. The technique was applied to aqueous solutions, that contained trace quantities of alkali metals, alkaline earth elements, transition metals, and non-metals. Because this technique is based on electrothermal atomization (ETA), it can be easily extended to samples that are organic based. In addition, electrothermal atomization (ETA) allows direct determinations of both solids and gases (1).

With the application of a laser plasma, ETA can be applied to emission spectrometry. This allows the simultaneous determination of more than one element. Since CRALIBS uses ETA for sample introduction, the desolvation, charring, atomization, and excitation of the analyte can be controlled. These independent controls allow the optimization of each process. This provides low ppm (nanogram) detection limits for alkali metals, alkaline earth elements, transition metals, and some non-metals. There are three main reasons that CRALIBS detection limits are higher than those of other atomic emission techniques:

- (1) dilution of the atomic vapor by the transport gas due to a large CRA chamber volume,
- (2) high background emission present in the laser plasma

(3) immaturity of the technique.

By using a graphite furnace, the atomic vapor is confined in a smaller volume. Preliminary detection limits reported by Majidi (2), obtained using a graphite furnace for sample introduction into the laser plasma, are in the picogram range.

The largest interferences in graphite furnace atomic absorption spectrometry (GFAAS) are chemical in origin. Because the laser plasma is highly energetic, it can dissociate, atomize, and excite any molecular species that would otherwise interfere in GFAAS. This interference becomes problematic in complex matrices, especially where the analyte cannot be separated from the interference(s). This is where CRALIBS would be best suited. It is also well suited for determinations in which sample is limited.

B. Instrumentation Upgrades

In the implementation of CRALIBS described in this dissertation, the instrumentation precludes simultaneous multielemental analysis. The addition of a gated charge coupled device (CCD) detector would remove this limitation. If the detector is not gated, the intense background emission present after plasma formation will saturate the detector. With a CCD, more sophisticated diagonistics of the plasma could be easily accomplished by viewing more than one wavelength at a time. It would give a more complete view of the effects the atomization cycle has on the laser plasma. Since the optimum time delay and laser power for the elements studied is between 25-50 µs and 3-4 MW/pulse, respectively, maximum sensitivity for each analyte is possible. The CCD

detector allows for dynamic background subtraction and the use of internal standards.

Another modification to the described instrumentation is the use of a modified graphite furnace (GF). The CRA was initally constructed because the optical axis for the laser beam had to be perpendicular to the emission axis. With a graphite furnace, there are two ways to view the plasma emission. The first way involves viewing on the same axis as the laser beam. Filtering the laser beam is possible, but is not recommended. The second method is to view the plasma emission through the dose hole of the GF where the sample is introduced; however, this only allows approximately 10% of the emission to be viewed. The modification of a GF would involve the addition of a quartz window on the side of the furnace. This would allow the viewing of the entire emission from the plasma without changing the integrity of the GF.

Another upgrade to the instrumentation would be the use of a power supply which can provide a faster heating rate. The current power supply is capable of heating the CRA at a rate of 800°C/s. Commerically available power supplies now have heating rates as high as 2000°C/s. A programmable power supply would give the best control over the heating cycles of the GF. Because the analyte would be volatized off faster, the resulting larger peak heights would improve the detection limits.

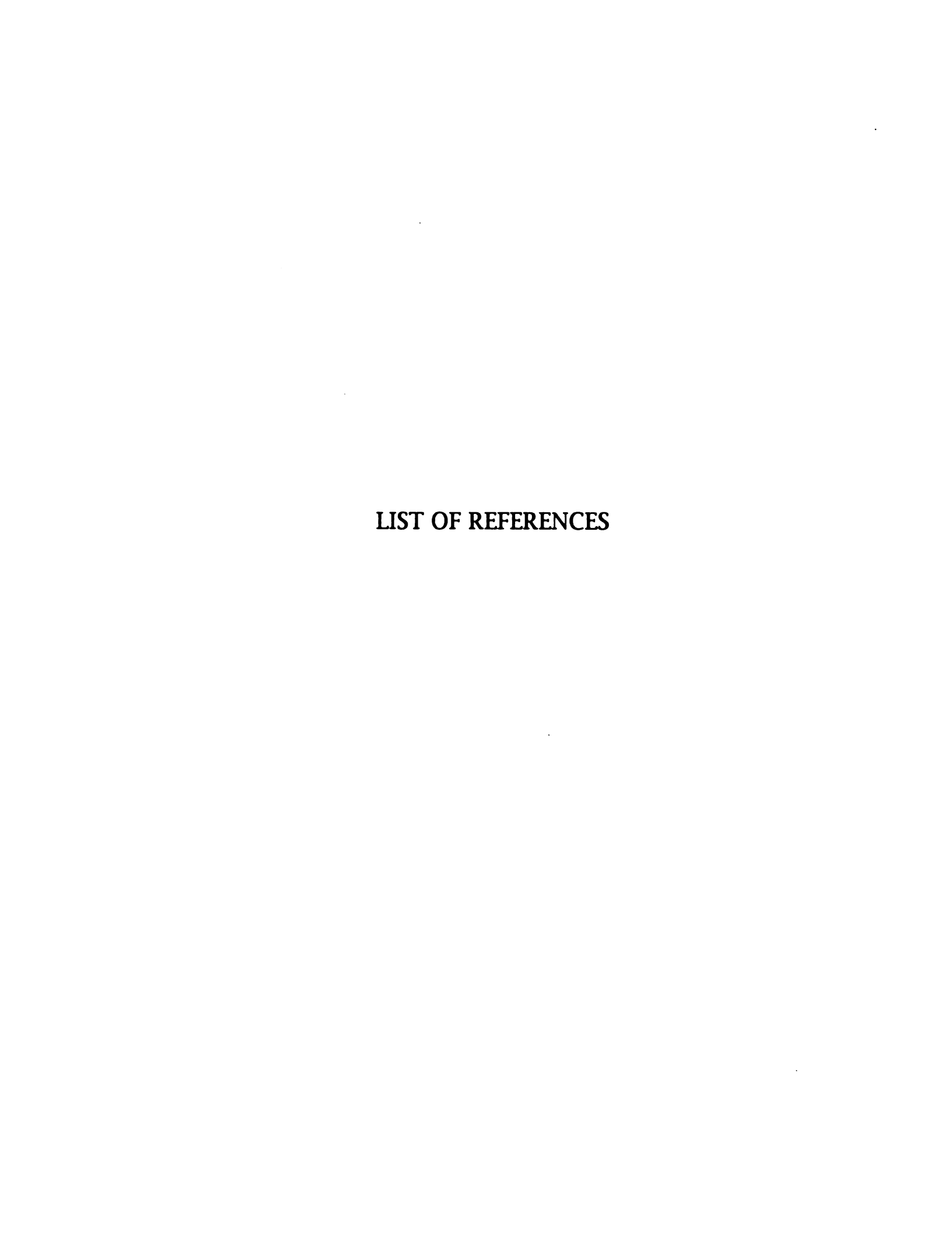
C. Future Applications

This dissertation has demonstrated some of the fundamental applications of using CRALIBS as a stand-alone instrument. There are several additional applications for which CRALIBS would be advantageous.

Currently, the inductively coupled plasma (ICP) is used as an ionization source for mass spectrometers (MS) (3). ICPs have the capability of ionizing elements of low to moderate ionization potential. However, the ICP does not have enough energy for ionization of many non-metals, such as halogens. Using a laser plasma, ionization of these species is possible. Since the plasma can be formed remotely, the carbon rod atomizer can be the intregral part of the ionization source of the MS. Currently, a similiar technique is being explored by Owens and Majidi (4).

An ICP atomization cell for atomic fluorescence has been demonstrated to provide spectral selectivity, freedom of interferences, and low background for detection of virtually all elements except for refractory elements (5). In addition to these advantages, CRALIBS does not suffer from ionization interferences due to the higher electron density in the laser plasma, and is able to determine refractory elements. In addition, the detection of ionic fluorescence could be delayed until later times in the plasma when excited state ions decay to the ground state ions. This would further improve detection limits because the maximum number of ions will be in the ground state for excitation and the background emission will have decayed substantially.

This technique can also be portable. This would provide trace analysis of metals and non-metals in the field where sample preparation would be at a minimum. Cremers (6) has used LIBS for detection of Pb in paint. This field determination used the laser plasma for sampling and excitation of the analyte in a handheld instrument. It also can be utilized for remote elemental analysis (7). Further portability applications of this technique are atmospheric pollution monitoring, nonintrusive analysis of hazardous materials, and fiber optic-based in situ analysis.



LIST OF REFERENCES

- 1. Fuller, C, Electrothermal Atomization for Atomic Absorption Spectrometry, Burlington House, London, England, 1977
- 2. Majidi, V., Rae, J. T., and Ratliff, J., Anal. Chem., 63, 1600 (1991)
- 3. Olesik, J., Anal. Chem., 63, 12A, 1991
- 4. Owens, M. and Majidi, V., J. Trace and Microprobe Tech., 10, 191 (1992)
- 5. Omenetto, N. and Winefordner, J., Chapter 9 in *Inductively Coupled Plasmas in Analytical Atomic Spectrometry*, Montaser, A. and Golightly, D. eds., VCH Publisher, New York, 1987
- 6. Cremers, D., 19th Meeting of the Federation of Analytical Chemistry and Spectroscopy Societies, 1992, talk #666, Philadephia, PA
- 7. Cremers, D., Appl. Spec., 41, 572 (1987)

